

AD-A014 862

BROADBAND ANTENNA STUDY

Lawrence R. Lewis, et al

Raytheon Company

20000727310

Prepared for:

Air Force Cambridge Research Laboratories

March 1975

DISTRIBUTED BY:

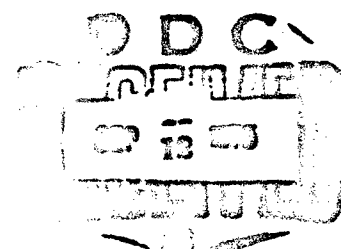
NTIS

**National Technical Information Service
U. S. DEPARTMENT OF COMMERCE**

**Reproduced From
Best Available Copy**

170 May 1962-31 March 1973

170 May 1962-31 March 1973



Reproduced by
NATIONAL TECHNICAL
INFORMATION SERVICE
US Department of Commerce
Springfield, MA 22151

REFERENCE BY	
FOR	DATE 10/10/70 <input checked="" type="checkbox"/>
ONE	DATE 10/10/70 <input type="checkbox"/>
UNCLASSIFIED	<input type="checkbox"/>
REVIEWED	
BY	
APPROVED/REVIEWED	
DATE 10/10/70	
A	1

Qualified requestors may obtain additional copies from the Defense Documentation Center. All others should apply to the National Technical Information Service.

UNCLASSIFIED

SECURITY CLASSIFICATION OF THIS PAGE (When Data Entered)

REPORT DOCUMENTATION PAGE		READ INSTRUCTIONS BEFORE COMPLETING FORM
1. REPORT NUMBER AFCRL-TR-75-0178	2. GOVT ACCESSION NO.	3. RECIPIENT'S CATALOG NUMBER
4. TITLE (and Subtitle) BROADBAND ANTENNA STUDY		5. TYPE OF REPORT & PERIOD COVERED Scientific - Final 07 Jan 72-31 Mar 75
7. AUTHOR(s) Lawrence R. Lewis Jerome Pozgay		6. PERFORMING ORG. REPORT NUMBER BR-8553
8. PERFORMING ORGANIZATION NAME AND ADDRESS Raytheon Company Missile Systems Division Bedford, Massachusetts 01730		9. CONTRACT OR GRANT NUMBER(s) F19628-72-C-0202
10. PROGRAM ELEMENT PROJECT, TASK AREA & WORK UNIT NUMBERS 4600-10-01 62702F		11. CONTROLLING OFFICE NAME AND ADDRESS Air Force Cambridge Research Lab. Hanscom AFB, Massachusetts 01731 Contract Monitor: Peter R. Franchi/LZR
12. REPORT DATE March 1975		13. NUMBER OF PAGES 147
14. MONITORING AGENCY NAME & ADDRESS (if different from Controlling Office)		15. SECURITY CLASS. (of this report) Unclassified
16. DISTRIBUTION STATEMENT (of this Report) Approved for public release, distribution unlimited		
17. DISTRIBUTION STATEMENT (of the abstract entered in Block 20, if different from Report)		
18. SUPPLEMENTARY NOTES		
19. KEY WORDS (Continue on reverse side if necessary and identify by block number) Broadband Radiators Octave Band Scanning Array Stripline Fed Flared Notch Antenna Leaky Wave Antenna Surface Wave Antenna		
20. ABSTRACT (Continue on reverse side if necessary and identify by block number) This final report describes the studies performed for AFCRL under Contract No. F19628-72-C-0202. The subject material may be classified in three separate topics. These are: the analysis of dielectric slab-covered waveguide arrays on large cylinders (extended array coverage), scattering from dielectric-covered periodic screens of small rectangular apertures (broadband antenna/radome technology), and the		

DD FORM 1473 EDITION OF 1 NOV 65 IS OBSOLETE

UNCLASSIFIED

SECURITY CLASSIFICATION OF THIS PAGE (When Data Entered)

UNCLASSIFIED

SECURITY CLASSIFICATION OF THIS PAGE (When Data Entered)

20. ABSTRACT (Cont.)

analysis of a stripline fed notch antenna and antenna array (broadband antennas). This report briefly summarizes the first two study areas where detailed accounts are included in Scientific Report No. 1 (AFCRL-73-0587) and Scientific Report No. 2 (AFCRL-74-0173). The investigation of the notch antenna and notch antenna arrays for broadband application are the primary subject material covered in this report.

The stripline fed flared notch antenna is shown to be a broadband radiator, capable of octave or greater bandwidths, in both isolated element and infinite array configurations. As shown by theoretical considerations the broadband nature of the element is associated primarily with the stripline-to-notch coupling region and the proper selection of planes for the notch and center conductor terminations.

Analysis of the coupling regions for both isolated element and infinite array configurations is restricted to the dominant modes of the stripline and notch regions. Higher order modes are partially included via the expressions for slit susceptance. The numerical results obtained from dominant mode analysis have shown excellent agreement with measured data for two broadband notch elements in the isolated configuration, and with a 256 element E-plane scanning array.

The computed results for the E-plane scanning array are in agreement with measured array gain loss to within 1dB over an octave band and 45° scan range. Computed reflection coefficients for the isolated elements are within .1 of measured values over 2:1 and 3:1 frequency bands.

Wave slowing has been observed for H-plane active array element patterns for one of the arrays considered. The slowing produces dips in the H-plane active element patterns at high frequencies, and consequently poses a restriction on the high frequency scan volume. The scan volume may be increased by appropriate change in element spacing.

UNCLASSIFIED

SECURITY CLASSIFICATION OF THIS PAGE (When Data Entered)

ACKNOWLEDGMENT

The authors extend their appreciation to Prof. Alex Hessel for his very helpful suggestions and guidance in several critical problem areas of this study.

TABLE OF CONTENTS

	Page
1. INTRODUCTION AND SUMMARY.....	1
1.1 Analysis of Dielectric Covered Slab on Large Cylinders.....	1
1.2 Scattering From Dielectric Covered Periodic Screens of Small Rectangular Apertures.....	4
1.3 The Notch Antenna and Antenna Array (Broadband Antennas).....	4
2. THE ISOLATED NOTCH ANTENNA.....	8
2.1 Analysis of Isolated Notch Antenna.....	10
2.2 Calculations and Measurements of Isolated Notch Antenna.....	35
3. GUIDED WAVES OF SLITTED PARALLEL PLATES.....	43
3.1 Complex Power, $\gamma = 0^+$	46
3.2 Complex Power, $\gamma = 0^-$	50
3.3 Dispersion Relation.....	58
4. PROPAGATION CHARACTERISTICS OF A PERIODIC ARRAY OF SLITTED PARALLEL PLATE GUIDES.....	64
4.1 Modes.....	64
4.2 Mode Functions of the Unit Cell Waveguide.....	76
5. THE INFINITE PHASED ARRAY OF NOTCH ELEMENTS.....	82
5.1 The Scattering Matrix \underline{S}^a	84
5.2 The Scattering Matrix \underline{S}^o	88
5.3 The Transmission Matrix \underline{T} of the Flared Notch Region.....	96
5.4 The Active Array Reflection Coefficient.....	99
5.5 Numerical Results.....	101
5. CONCLUSIONS.....	117

APPENDIX A

STRIPLINE TEM MODE FUNCTIONS

119

	Page
APPENDIX B	
SLIT SUSCEPTANCE FOR SLITTED PARALLEL PLATE GUIDE	127
APPENDIX C	
ORTHONORMAL MODE FUNCTIONS OF PARALLEL PLATE REGIONS WITH OPEN AND SHORT CIRCUIT BOUNDARIES	129
APPENDIX D	
COUPLING COEFFICIENTS FOR SLITTED PARALLEL PLATE ARRAY TO FREE-SPACE TRANSISTION	133
REFERENCES.....	137

List of Illustrations

<u>Figure</u>		<u>Page</u>
1-1	Flared Notch Antenna	2
2-1	Flared Notch Antenna	9
2-2	Infinite Slit-Infinite Stripline Geometry	11
2-3	Equivalent Network of the Scattered Field Contribution in the Strip Transmission Line	15
2-4	Notch Element Radiation Pattern, 16 GHz, No Ground Plane	18
2-5	Notch Element Radiation Pattern, 12 GHz, No Ground Plane	19
2-6	Approximate Aperture Equivalent Circuit	22
2-7	Network Representation of Infinite-Slit-Infinite Stripline Coupling Region	25
2-8	Modulus of Scattering Parameters S_{11} and S_{31} vs a/λ	27
2-9	Phase of Scattering Parameter S_{11}	29
2-10	Approximate Model of Notch Element with Open and Short Circuit Terminations	30
2-11	Reflection Coefficient vs a/λ - parameter Y_2/a	33
2-12	Reflection Coefficient vs a/λ - parameter $1 \times a/\lambda$	34
2-13	Notch Element Geometry	36
2-14	Measured and Calculated $ \Gamma $ vs a/λ Element #5	38
2-15	Measured and Calculated $ \Gamma $ vs a/λ Element #6	39
2-16	Measured $ \Gamma $ vs a/λ Elements 1 and 2	40
2-17	Measured $ \Gamma $ vs a/λ Elements 1, 3 and 4	42
3-1	Slitted Parallel Plate Region	44
3-2	Strip Geometry for Determination of Leaky Wave Spectrum, $k_{xn}(a)$	45
3-3	Circuit of Transmission Line Bank Excited by Equivalent Aperture Voltage Sources	55

<u>Figure</u>		<u>Page</u>
3-4	$\text{Re} \{ \gamma_i \}$ vs. γ_λ Parameter h/λ	59
3-5	$\text{Re} \{ \gamma_i \}$ vs. a/λ Parameter a/h	61
3-6	Real Part of Higher Leaky Mode of Slitted Parallel Plate Region, Parameter h/λ	62
3-7	Imaginary Part of Higher Leaky Mode of Slitted Parallel Plate Region, Parameter h/λ	63
4-1	Infinite Array of Periodic Slits	65
4-2	Unit Cell of Infinite Array of Slitted Parallel Plate Guides	66
4-3	Equivalent Circuit of Unit Cell	67
4-4	γ_o vs. $\hat{\alpha}_d/\pi$, Parameter a/λ	70
4-5	γ_o vs. $\hat{\alpha}_d/\pi$, Parameter a/λ	71
4-6	γ_o vs. $\hat{\alpha}_d/\pi$, Parameter a/λ	72
4-7	γ_o vs. $\hat{\alpha}_d/\pi$, Parameter a/λ	74
4-8	Lowest Order Passband of the Dispersion Relation for Iris Loaded Waveguide; $\bar{\Gamma}_3(\theta, \hat{\theta})$ Versus θ	75
4-9	Susceptance Load Lines on Dispersion Curve for Iris Loaded Waveguides	77
4-10	$n = 0$ Mode Function, (H-Mode)	80
4-11	$n = 0$ Mode Function, (H-Mode)	81
5-1	Notch Element Array, "Egg Crate"	83
5-2	Equivalent Circuit of Unit Cell	85
5-3	Cell Geometry	89
5-4	Network Definitions for Stripline-to-Slitted Parallel Plate Coupling Region	94
5-5	Modulus of Scattering Parameters $ S_{11}^o $ and $ S_{21}^o $ vs. a/λ , $\hat{\alpha}_d/\pi = 0$	97
5-6	64 Element "Egg Crate" Array	102
5-7	Array 1 Active Reflection Coefficient vs H-Plane Scan Angle, θ	105
5-8	Array 2: Active Array Reflection Coefficient vs H-Plane Scan Angle, θ	106
5-9	Array 2: Active Array Reflection Coefficient vs E-Plane Scan Angle, θ	108

<u>Figure</u>		<u>Page</u>
5-10	Array 1: Active Array Element Pattern, H-Plane	110
5-11	Array 1: Active Array Element Pattern, H-Plane	111
5-12	Array 2: Active Array Element Pattern H-Plane	112
5-13	Array 2: Active Array Element Pattern, E-Plane	113
5-14	Array 2: Measured Array Directive Gain Relative to Theoretical Full Array Gain and Calculated Active Array Element Gain Relative to Cell Gain <u>vs.</u> Frequency, Broadside Scan	114
5-15	Array 2: Measured Array Directive Gain Relative to Theoretical Full Array Gain and Calculated Active Array Element Gain Relative to Cell Gain <u>vs.</u> Frequency, E-Plane Scan Angle = 30°	115
5-16	Array 2: Measured Array Directive Gain Relative to Theoretical Full Array Gain and Calculated Active Array Element Gain Relative to Cell Gain <u>vs.</u> Frequency, E-Plane Scan Angle = 45°	116
A-1	Stripline Cross Section	120
C-1	Parallel Plate Region with Open and Short Circuit Boundaries	130

1. INTRODUCTION AND SUMMARY

This final report describes the studies performed for AFCRL under Contract No. F19628-72-C-0202. The subject material may be classified in three separate topics. These are: the analysis of dielectric slab-covered waveguide arrays on large cylinders (extended array coverage), scattering from dielectric-covered periodic screens of small rectangular apertures (broadband antenna/radome technology), and the analysis of a stripline fed notch antenna and antenna array (broadband antennas). This report briefly summarizes the first two study areas where detailed accounts are included in Scientific Report No. 1 (AFCRL 73-0587) and Scientific Report No. 2. (AFCRL-74-0173). The investigation of the notch antenna and notch antenna arrays for broadband application are the primary subject material covered in this report.

1.1 Analysis of Dielectric Slab-Covered Arrays on Large Cylinders

This study was performed during 1972-73. The objective of the study program was the investigation of techniques to obtain hemispheric scan coverage (no more than 6 db antenna gain fall off or oscillation over the hemisphere) by using an array of waveguide apertures covered by a dielectric slab. The array is on a cylindrical ground plane of large radius ($R \simeq 100 \lambda$) and its aperture gain is between 20 and 30 db above isotropic. The most significant result of the study was that hemispheric scan coverage is indeed achievable with dielectric covered arrays.

In a first phase of the study the properties of infinite cylindrical arrays covered by dielectric were investigated. The problem was approached by separately

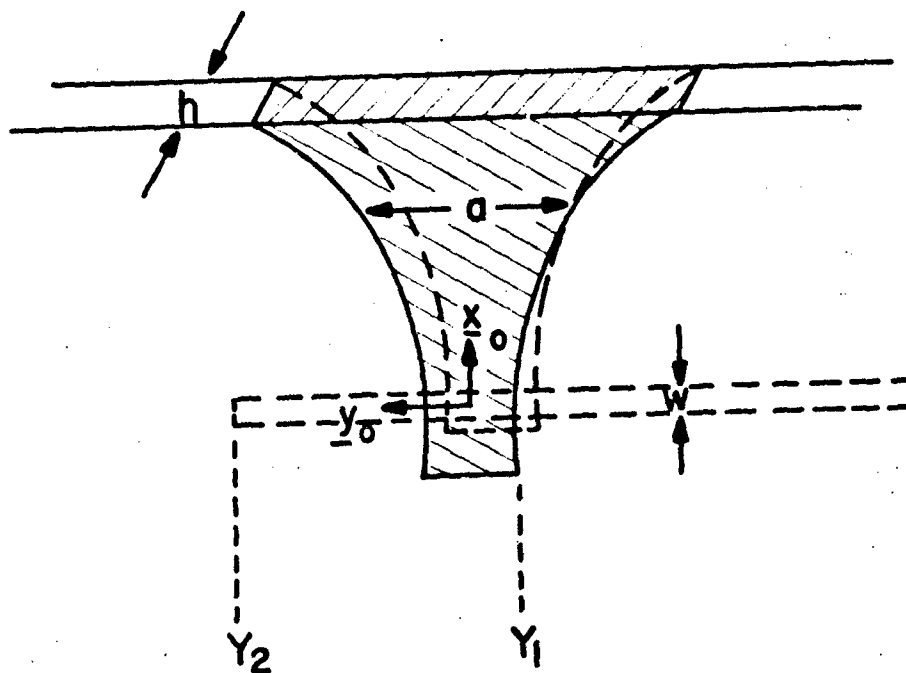


Figure 1-1. Flared Notch Antenna

enforcing the continuity of the EM fields at the air-dielectric and at the dielectric-cylinder interface.

The computations showed that there are only minor differences in the element pattern and in driving point admittance between dielectric-clad cylindrical arrays of large radius and the corresponding planar arrays. Coverage performance of a finite dimension array (aperture gain 20-30 db) on a large cylinder can be evaluated with excellent approximation by means of a plane array model.

In the second phase of this study program efforts were directed at the investigating the radiation properties of finite arrays of waveguide elements in an infinite ground plane covered by an infinite dielectric sheet. The main results of the second part of the studies was in developing a method of analysis of finite arrays. Computations of the coverage of an array of 61 circular waveguide elements showed that it is not possible to obtain hemispheric coverage from arrays in an infinite ground plane covered by dielectric. No radiation can occur in directions close to endfire because the energy leaving the array is trapped in a surface wave propagating along the dielectric sheet. In order to achieve endfire coverage the energy bound to the surface wave must be radiated in free space by terminating the dielectric sheet.

In the last phase of the program the radiation properties of surface wave excited dielectric wedges were studied by generating a transmission line model. The patterns and the reflection coefficients of several tapered two dimensional wedges were investigated. The analytical results showed that by properly tapering the dielectric wedge, it is possible to obtain hemispheric scan coverage from an array of 20-30 db aperture gain.

1.2 Scattering From Dielectric-Covered Periodic Screens of Small Rectangular Apertures

This study was performed during 1972-74. The objective was to investigate the use of self complementary screens as broadband devices to plane wave incidence. The results of this study confirmed that the screen of small apertures is highly transmissive; however, when used in combination with dielectrics suitable for radomes at microwave frequencies, the self-complementary screen will not enhance the bandwidth. More significantly, for increasing frequency ($s/\lambda \geq 0.1$ to $s/\lambda \lesssim 0.21$), the reflection characteristics of the uncovered screen are such that a constant shunt capacitive susceptance is realized. The constant capacitive element characteristic suggests the use of self-complementary screens as:

- 1) Low pass filters or filter sections;
- 2) Dispersionless capacitive microwave circuit elements;
- 3) Harmonic filters in waveguides or integrated to radomes, and
- 4) Matching devices in waveguides.

1.3 The Notch Antenna and Antenna Array (Broadband Antennas)

The notch antenna study was performed during 1974-75. The objective was to theoretically determine the bandwidth properties of this antenna as an isolated element and an element of a scanning phased array. Comparisons with experimental results would determine the validity of analysis and the range of applicability.

The broadband behavior of the notch antenna has been demonstrated; both isolated and as an element of an infinite array. The well matched broadband (over an octave) charac-

teristic is in excellent agreement with measurements. These comparisons are for both an isolated antenna example and a scanning phased array.

The notch antenna is sketched in Fig 1-1. The basic broadband characteristic is associated with the stripline feed coupling into the constant width notch formed by symmetrical etching of the parallel plate walls. Bandwidth properties depend on the stripline and notch termination as well as notch and stripline dimensions. The radiation of the antenna is via a travelling wave launched at this coupling junction, into this slit or notch. The properties of this junction are determined by 1) enforcing conservation of energy between the stripline dominant mode and that of the guided wave (source of radiation) and 2) assuming an approximate aperture susceptance.

For both the array and isolated element cases the guided wave spectrums of the slitted regions are required. These are determined by applying transverse resonance to the appropriate configurations.

For each antenna configuration (isolated or array) the transition to free space off the element edge presents a second discontinuity. This interface is well matched for the isolated case; demonstrated experimentally and inferred from the analysis. In a scanning array this discontinuity is not necessarily well matched with scan, and is thus explicitly modeled analytically. The transverse fields in the unit cell of the infinite array are mode matched across the plane of discontinuity via Galerkins method.

In chapter 2 the formulation of the analysis for the isolated notch antenna is presented. Circuit analogies are used to enhance understanding of the coupling mechanisms. Equations for reflection coefficient are obtained and used to compute results for a representative range of physical

parameters over wide bandwidths. A comparison with several measured elements is included, where agreements are excellent.

The guided modes appropriate for the notch region are determined in chapter 3. The spectrum is that of a slitted parallel plate guide which can be extended for use in a non-uniform tapered notch region. These modes are found by requiring continuity in power flow across the slitted waveguide region. The lowest order guided modes are surface waves, higher modes are leaky, with relatively large attenuation. The surface wavenumber is very slowly varying with both frequency and slit width; necessary for a broadband coupling region and well matched flare. Curves of normalized wavenumber versus geometry parameters and frequency are presented.

Basic to the evaluation of an infinite array analysis of notch elements is the determination of the modes of an array of slitted parallel plate guide. These wavenumbers and modal fields are solved for in Chapter 4. The dispersion relation is derived via application of transverse resonance in a unit cell of the infinite structure. This dispersion relation limits correctly to the cases of: 1) slit width equal to lattice spacing, and 2) parallel plate spacing $\rightarrow 0$. The modes are expressed as normalized wavenumber as a function of inter-element phase excitation. The trends observed in the variations of wavenumber are justified by examining the dispersion diagram for the case where plate spacing $\rightarrow 0$.

The mode functions are derived from transmission line circuit relations of a network representation in the transverse plane. The modes limit properly at the band edges (boundary between pass and stop bands); either short or open circuits. In the formulation the symmetry with a cell is exploited to simplify the equations and computations.

The analysis of an infinite array of notch elements is presented in Chapter 5. The elements are linearly polarized and the array configuration forms an "egg crate" type construction. Active reflection and coefficients are derived in terms of scattering matrices at the stripline-notch coupling region and notch-free space transition. An equivalent circuit in terms of these scattering matrices is used to derive these results. Computed results show 1) the broadband characteristic is retained with scan and 2) there is some premature element pattern dip associated with wave slowing from the corrugated surface. The broadband scan characteristic is very encouraging for use in broadband-wide scan application; however, there is some constriction of the resonance free-scan volume. Thus, at some increase of element density high performance goals can be achieved.

The computed element patterns for octave band 45° scan, compare very well to those measured on a 256 element scanning array.

An $e^{j\omega t}$ time dependence is assumed throughout.

2. THE ISOLATED NOTCH ANTENNA

A stripline fed tapered notch is an antenna capable of broad bandwidths. A sketch of the antenna configuration is shown in Fig. 2-1. The strip transmission line is fed in the dominant mode and couples to the notch discontinuity. The notch is etched away on both outer conductors forming a balanced (symmetric) termination. The basic radiation mechanism is via a coupled leaky wave in the notch region. A traveling wave is launched off the board edge and radiates normal to it.

There are essentially two transition regions of the structure which must individually possess broadband behavior: the coupling from the dominant stripline mode (TEM WRT \perp) to the traveling wave in the notch (with and without the terminations in the stripline and at the notch bottom), and the transition to free-space off the board edge. Empirically, it has been established that for particular notch widths, line widths and center conductor placement the coupling to the leaky mode is very broadband. The notch free-space transition was found to be broadband for a range of wide gaps at the notch edge.

This chapter is concerned with the analytic formulation and calculations of the coupling from the stripline to notch region.* The basis of solution involves establishing the mode spectrum of the notch region (Chapter III) and determining the coupling to these modes from the stripline feedguide. The coupling is found from consideration of the infinite slitted region fed by stripline extending to infinity beyond the slit. The symmetry of this four port can be exploited to obtain a scattering matrix into which appropriate terminations of the

* The broadband behavior of the free-space transition for large parameter variations has been established empirically. Moreover, the leaky mode impedance (Chapter III) is shown to be very close to that of free-space further justifying the observed results.

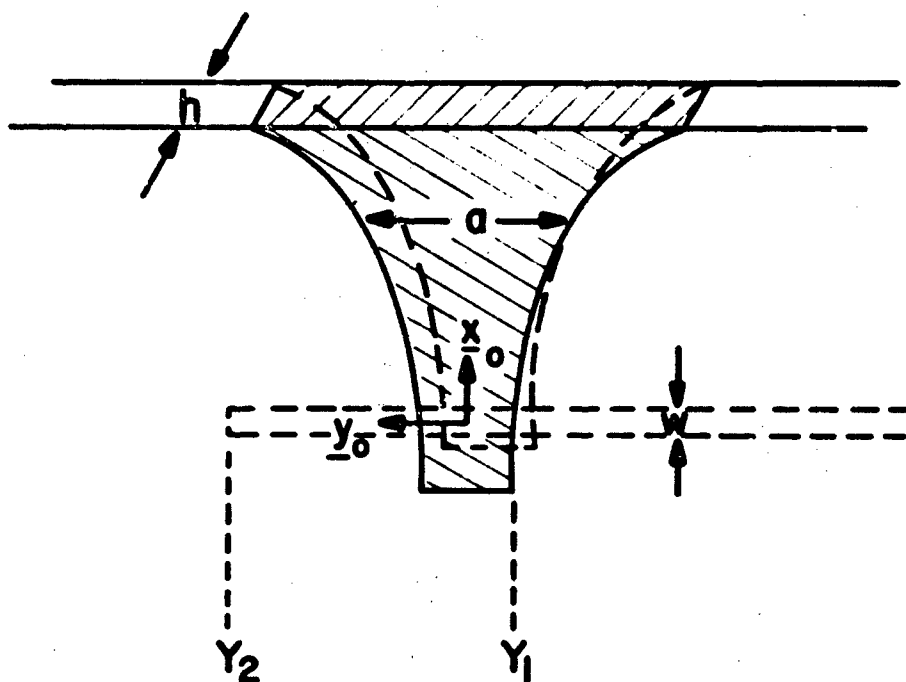


Figure 2-1. Flared Notch Antenna

notch bottom (short circuit) and end of the stripline center conductor (open circuit) can be incorporated. The matching properties of the four port are derived from a requirement of conservation of energy and an assumed form of slit susceptance in the coupling region.

The broadband characteristic of the notch antenna is theoretically demonstrated. Comparisons of computed reflection coefficients with results of several measured antennas show excellent agreement.

2.1 Analysis of Isolated Notch Antenna

The unique bandwidth properties of the notch antenna are associated with the stripline feed-to-notch coupling region and the location of the open and short circuit terminal planes. In order to solve for the coupling the guided wave spectrum of the notch is required. These modes are developed and discussed in chapter III.

The analysis for the coupling or scattering into the notch is conveniently first solved for an infinite slit fed by stripline extending beyond the slit to infinity. This geometry is shown in Fig. 2-2. The scattering matrix of this geometry can readily incorporate the stripline and notch terminations from which the reflection and transmission properties of the antenna are obtained. The solution to this slit geometry provides insights into the nature of the coupling mechanism of the notch.

For small slit width ($a/\lambda \ll 1$ in the coupling region for the notch antenna) the slit (or aperture) field may be assumed \underline{y}_0 directed and uniform in y . With TEM stripline feed excitation (from $y = \pm \infty$ or both) the notch field distribution remains symmetric in x . The aperture field is thus represented as a superposition of guided waves with uniform amplitudes,

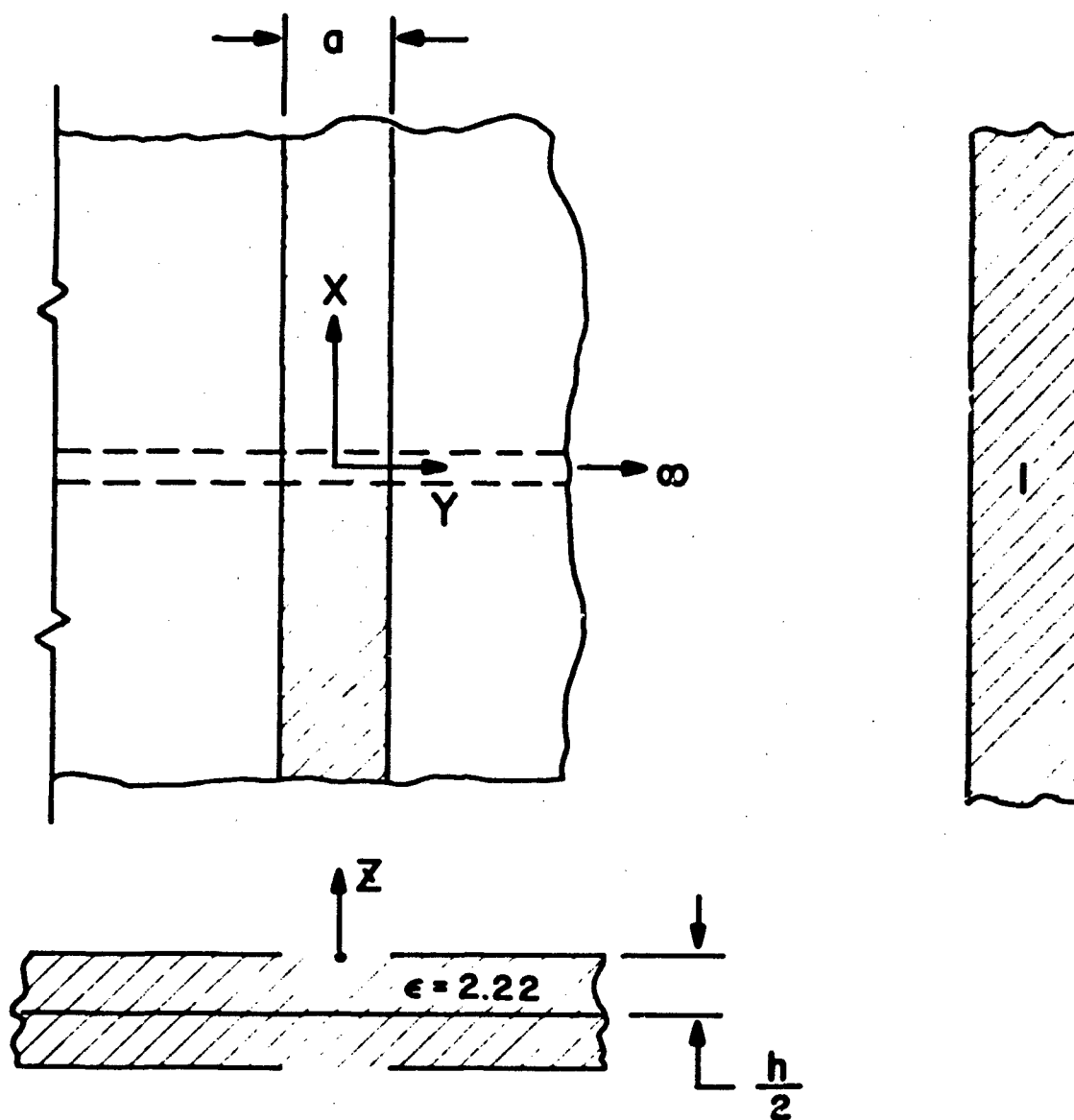


Figure 2-2. Infinite Slit-Infinite Stripline Geometry

symmetrically leaving the $x = 0$ plane,

$$\underline{E}_{ap} = y_0 \sum_i E_i e^{-j k_i |x|} P(y) \quad (2-1)$$

where $P(y) = \begin{cases} 1, & |y| \leq a/2 \\ 0, & \text{otherwise} \end{cases}$

The procedure outlined by Felsen^[1] is used to find the coupling of this longitudinal slit in stripline. The total field inside the stripline is given as a superposition of the scattered fields from the slit properly added to those of the unperturbed region. The equivalence theorem is used to obtain those scattering sources associated with the aperture based on the assumed form of \underline{E}_{ap} in (2-1). A suitable Green's function is then used to find the resulting coupling into the stripline. The unperturbed solution for the longitudinal slit reduces to the trivial case of uniform matched strip transmission line.

The scattered fields in the stripline arise from the equivalent magnetic current source, given by,

$$\underline{M}(x, y, z) = z_0 \times \underline{E}_{ap}(x, y) [\delta(z) - \delta(z-h)] \quad (2-2)$$

where $\delta(z)$ is the Dirac-delta function. The aperture (or slit) may be closed and the short circuit wall will sustain \underline{M} with the resulting fields inside the stripline the same as the original problem. This equivalent current is put in a representation in terms of stripline modes, ^[2]

$$\underline{M}(x, y, z) = \sum_n v_n(y) h_n(x, z) \quad (2-3)$$

In this representation h_n are the transverse to y magnetic mode functions of stripline, and $v_n(y)$ are the corresponding scalar voltage amplitudes.* The dominant mode functions e_0 and h_0 are

* The formalism is carried out for single mode which appears justified based on the excellent comparisons with measured results. Higher mode effects are included in both the assumptions for slit susceptance and the power flow relations, to be discussed.

derived in Appendix A, with a corresponding orthogonality relation. The voltage amplitudes are interpreted as distributed series voltage sources in the stripline media.^[1] This circuit equivalence facilitates solutions of the scattered fields.

The orthonormality properties of the derived mode functions are used to obtain an equation for the voltage amplitude,

$$V_0(y) = \iint_{C_g} \vec{z}_0 \times \vec{E}_{ap} \cdot \vec{h}_0(x, z) [\delta(z) - \delta(z-h)] dC_g \quad (2-4)$$

where C_g is the stripline cross section extending from $-h \leq z \leq 0$ and $-\infty < x < \infty$. With the particular representation of \vec{E}_{ap} given in (2-1) and $\vec{h}_0(x, z)$ defined in Appendix A equation (A -38 to A -30) the voltage defined in (4-2) is,

$$V_0(y) = \sum_i E_i \epsilon_i P(y) \quad (2-5)$$

with

$$E_i = N \left\{ \frac{4w}{h} \frac{1 - e^{-jk_z w/2}}{jk_z w/2} + 8e^{-jk_z w/2} \sum_{\substack{p=1 \\ \text{odd}}}^{\infty} \frac{\sin \frac{p\pi}{2}}{p\pi/2} \frac{1}{p\pi + jk_z h} \right\} \quad (2-6) *$$

where

$$N = (4w/h + 1.09)^{-1/2}$$

h = stripline plate spacing

w = center conductor width

* For dimensions typical of practical radiating elements, E_i is essentially frequency independent and is approximately given by,

$$E_i \sim N (4w/h + 1.485)$$

where the summation in equation (2-6) reduces to $16/\pi^2 \beta(2)$ and $\beta(2)$ is Catalan's constant^[3]

The voltage amplitude, V_0 , obtained from the magnetic currents in the aperture is equivalently a distributed series voltage source in the y directed modal transmission line corresponding to the dominant stripline mode. The equivalent network of this scattering source is shown in Fig. 2-3.

The transmission line modal current, $I_0^s(y)$ in $-a/2 < y < a/2$, resulting from the applied scattering source $V_0(\xi)$ is given as,

$$I_0^s(y) = - \int_{-a/2}^{a/2} d\xi \mathcal{Y}(y, \xi) V_0(\xi) \quad (2-7)$$

where $\mathcal{Y}(y, \xi)$ is the admittance Green's function for a unit voltage source at a point ξ on the uniform modal transmission line. For the TEM stripline mode (defined with normalizations in Appendix A) in an infinite line this Green's function may be written as,

$$\mathcal{Y}(y, \xi) = \frac{1}{2\eta_0} e^{-jk_0|y-\xi|} \quad (2-8)$$

where $\eta_0 = \eta_0/\sqrt{\epsilon}$; η_0 = free-space impedance = 377Ω ; and $k_0 = k/\sqrt{\epsilon}$. Using (2-8) and (2-5) in (2-7) yields,

$$I_0^s(y) = - \frac{\sum E_i \epsilon_i}{jk\eta_0} [1 - e^{-jk_0 a/2} \cos k_0 y], \quad y \leq |a/2| \quad (2-9)$$

With the generator voltage V_g^+ set equal to zero and only the scattered source considered residing in $-a/2 \leq y \leq a/2$, then propagation is away from the planes at $y = -a/2$ and $y = a/2$. Thus at $y = -a/2$,

$$I_0^s(-a/2) = I_g^{s-} = -V_g^{s-}/\eta_0 \quad (2-10)$$

The reflected voltage at $y = -a/2$ from the scattering aperture

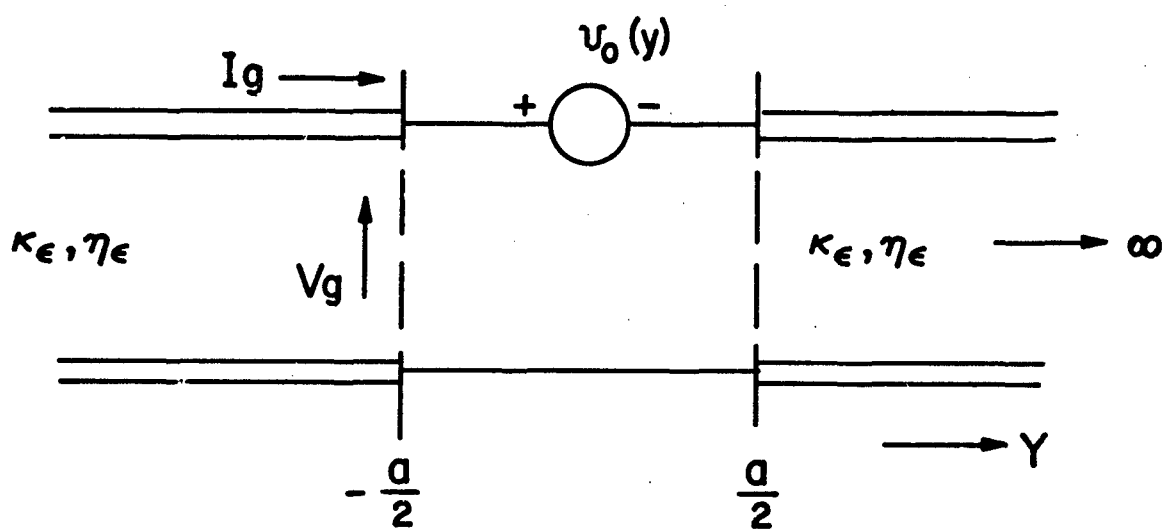


Figure 2-3. Equivalent Network of Scattered Field Contribution in the Strip Transmission Line

is obtained from (2-9) and (2-10) as,

$$V_g^{s-} = \frac{\sin u}{u} e^{-ju} \frac{a}{2} \sum_i E_i \epsilon_i \quad (2-11)$$

where $u = k_0 a/2$. From the symmetry of (2-9) and the radiation condition requiring $+y$ propagation, $y > a/2$, the scattered voltage at $a/2$ is given by,

$$V^s(a/2) = -V_g^{s-} \quad (2-12)$$

To obtain total voltages and currents at the planes $y = \pm a/2$, the unperturbed (scatterer removed) solutions must be considered. Removing the equivalent aperture source M leaves a uniform (in y) cross section strip transmission line of infinite extent. The voltage at $y = -a/2$ in this case is,

$$V^o(-a/2) = V_g^+ \quad (2-13) *$$

The voltage at $y = a/2$ is the excitation voltage with an appropriate phase delay given as,

$$V^o(a/2) = V_g^+ e^{-2ju} \quad (2-14)$$

The total voltages at the planes $y = \pm a/2$ are:

$$V(-a/2) = V_g^+ + \frac{\sin u}{u} e^{-ju} \frac{a}{2} \sum_i E_i \epsilon_i \quad (2-15)$$

and

$$V(a/2) = [V_g^+ e^{-2ju} - \frac{\sin u}{u} e^{-ju} \frac{a}{2} \sum_i E_i \epsilon_i] \quad (2-16)$$

* The plane $y = -a/2$ has been arbitrary selected as the phase reference plane for the internal (stripline) geometry.

The transmission and reflection properties of the structure can thus be determined from the above equations with a knowledge of the aperture field excitations E_i .

To determine the aperture field E_{ap} the following approximations are made:

- a) Single mode $E_i \rightarrow E_0$; this approximation has been partially justified from calculations of the next higher mode coupling coefficients, being of the order -20dB from that of the dominant mode.
- b) The radiated power is associated only with the surface wave mode. This implies that the space wave contribution is small. The measured directional properties of the antenna, shown for example in Figs. 2-4 and 2-5, are constant with this assumption. In particular comparing the rear and side response to that in the forward direction indicates the directional nature of a travelling wave antenna.

The first approximation simplifies equation (2-1) for the aperture field:

$$E_{ap} = j_0 E_0 e^{-jk_x |x|} P(y) \quad (2-16)$$

The second approximation facilitates a conservation of energy relation* that is used to solve for the unknown field amplitude E_0 .

* The solution for the unknown aperture field in terms of a conservation of energy relation needs a further assumption of slit susceptance. These approximations are all justified individually, and yield results in excellent agreement with measurements. An alternative field matching approach involves an integral of the form,

$$\int_{-\infty}^{\infty} dk_y e^{jk_y y} \frac{\sin k_y a}{k_y a/2} \int_{-\infty}^{\infty} dk_x e^{jk_x x} \frac{k^2 - k_x^2}{\sqrt{k^2 - k_x^2 - k_y^2}} \frac{2k_x}{k_x^2 - k_{x0}^2}$$

which is very difficult to solve.

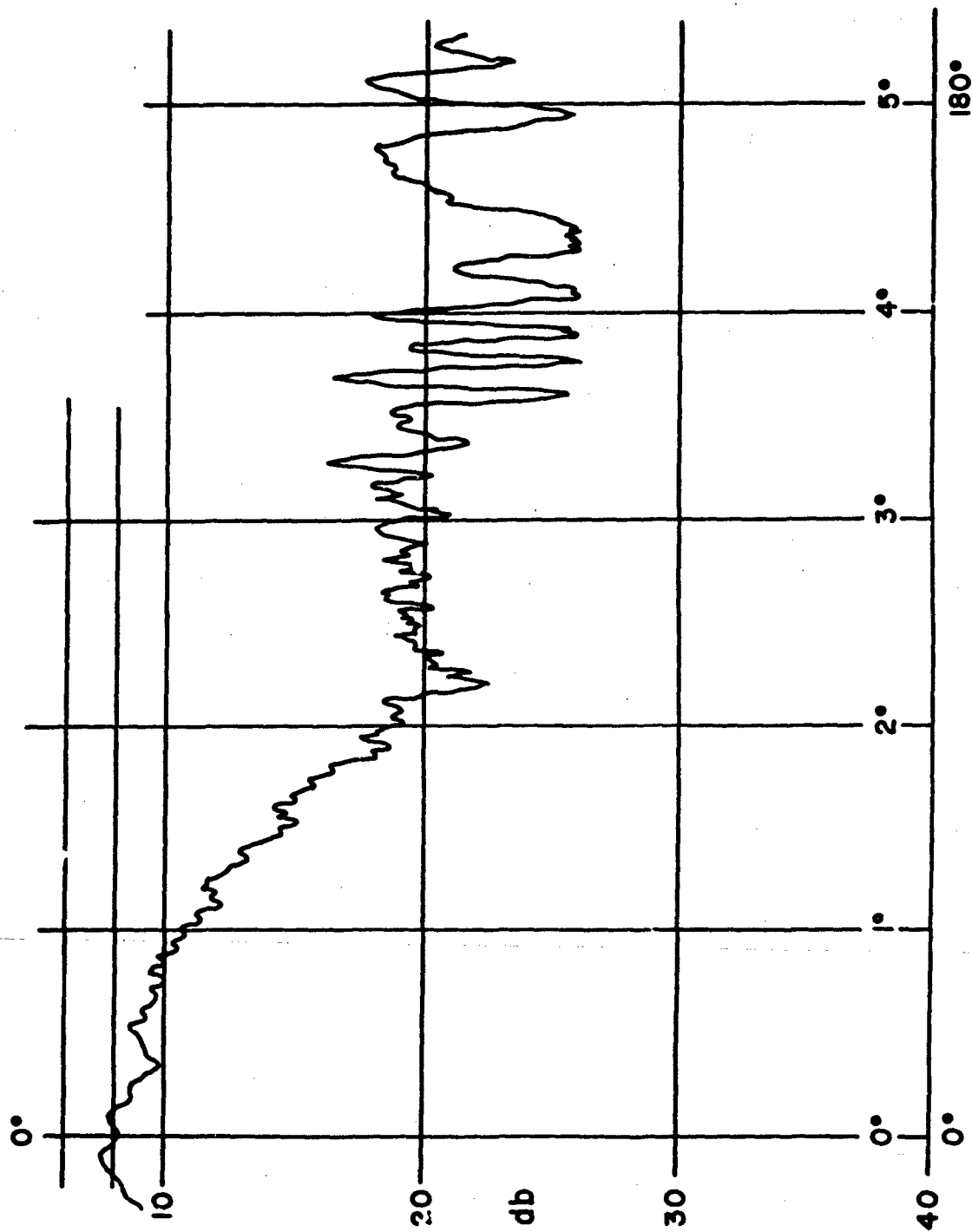


Figure 2-4 Notch Element Radiation Pattern
16GHz No Gr und Plane

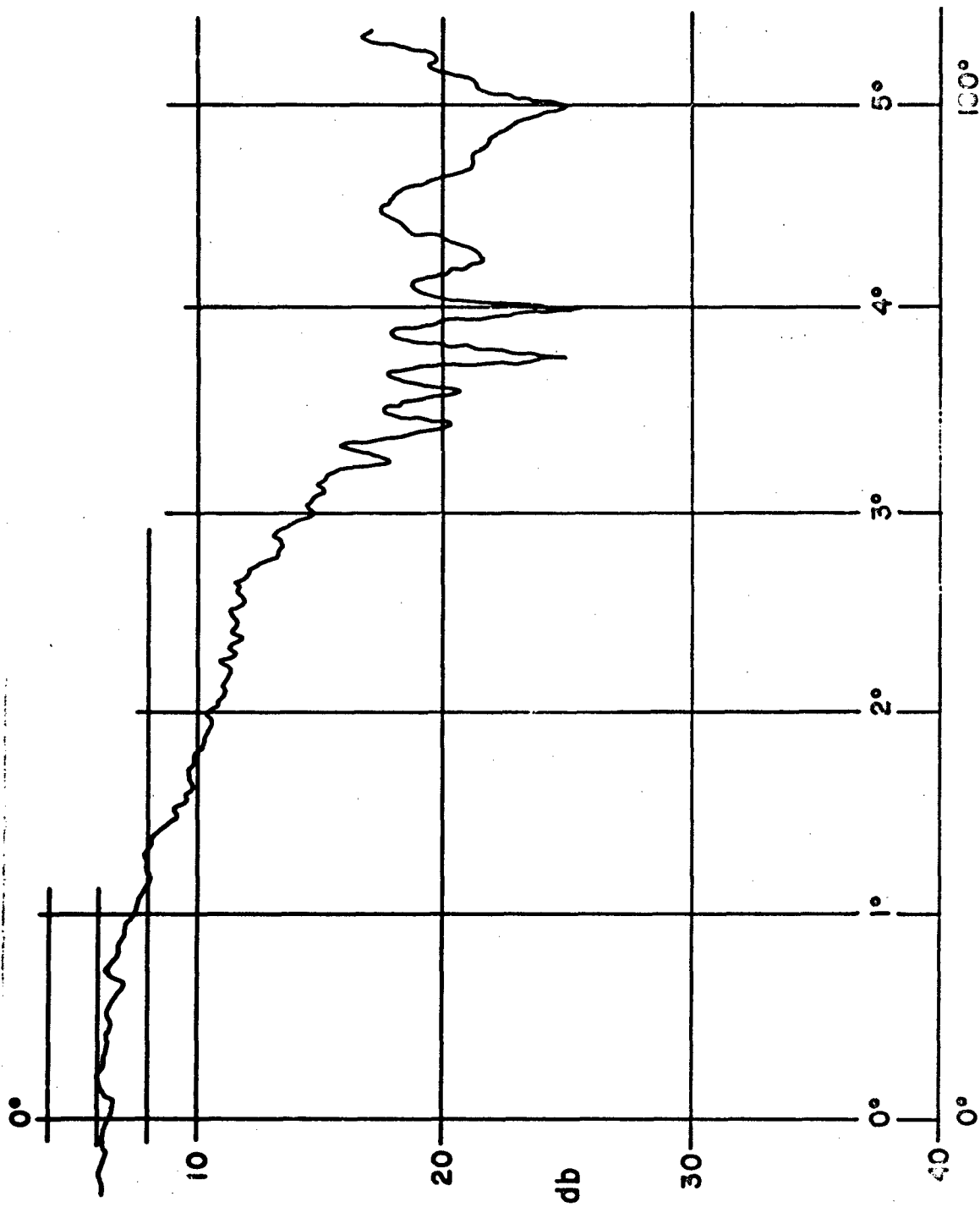


Figure 2-5 Notch Element Radiation Pattern
F=12GHz No Ground Plane

Real power conservation requires that,

$$P_{inc} = P_{ref} \Big|_{y = -a/2} + P_{trans} \Big|_{y = a/2} + P_{rad} \text{ (in the surface wave)} \quad (2-17)$$

where,

P_{inc} - incident power or maximum available power from the generator,

$$= |V_g|^2 / \eta_0$$

P_{ref} - reflected power at $y = -a/2$, solely arising from the scattering aperture.

$$= |V_g|^2 / \eta_0$$

(see(2-11))

P_{trans} - power going to the infinite stripline termination;

$$= |V(a/2)|^2 / \eta_0$$

P_{rad} - the total radiated power; this power is assumed to be solely associated with the x directed surface wave.

The numerical results for the modes in Chapter III exhibit a surface wave character for the dominant guided wave in x.

An expression for this surface wave power flow is obtained from a modification of results derived in reference^[4].

This power flow relation uses the travelling wave form for the fields on the infinite structure (i.e. $e^{-jk_x x}$ dependence) and is given as^[5]

$$jP_{rad} = \frac{\partial}{\partial k_x} \left[\int_{slit} (\epsilon_0 \mathbf{E} \times \mathbf{H}^*(z=0^-)) \cdot (-\hat{z}) dS + \int_{slit} (\epsilon_0 \mathbf{E} \times \mathbf{H}^*(z=0^+)) \cdot (\hat{z}) dS \right] \quad (2-18)$$

The first integral expression of (2-18) is the power flow normal to the slit at $z = 0^-$ ($-\hat{z}$ direction) and the second term is the power flow normal to z , for $z = 0^+$ ($+\hat{z}$ direction).

The individual power expressions are derived in Chapter III in connection with the determination of the slit guide mode spectrum. Equation (2-18) is solved numerically for P_{rad} from the formal expressions of Chapter III. The result may be cast as,

$$P_{\text{rad}} = A |E_0|^2 \quad (2-19)$$

with $A = A(k, k_{x1}; a, h, \epsilon)$. Using the results of (2-11), (2-15) and (2-19) in (2-17) yields,

$$|E_1| = -\cos(\theta_0 + \theta_s + u) \frac{|V_1| |E_0| \sin u}{k_s A \eta_0 + u |E_0|^2 \frac{\sin^2 u}{u}} \quad (2-20)$$

where θ_0 is the phase of E_0 , θ_s is the phase of E_s , and a factor of 4 is included into the first term of the denominator because of the double-sided slit geometry, and the symmetric excitation in x .^{*} Equation (2-20) forces conservation of energy in terms of the magnitude and phase of E_0 . By deriving an approximate equivalent circuit for the slit discontinuity, an expression for the phase of E_0 , θ_0 , is obtained.

The coupling region from the stripline to slit is very small (even three center conductor line widths $\ll \lambda$) and within this region the dominant guided mode field is approximately constant (i.e. $E_{\text{ap}} \approx E_0 y_0$ for $|x|$ small). In this fashion, the susceptance associated with a uniformly excited infinite slit is about the same as for the stripline-slit coupling region. The slit susceptance is presented in Appendix B.

The equivalent circuit of Fig. 2-3 can be further specialized, in light of the derived form of controlled scattering source and the assumed slit field in the coupling region. This network may be reduced to that of Fig. 2-6. The

^{*} Total power in the surface waves is $4 A/E_0/2$

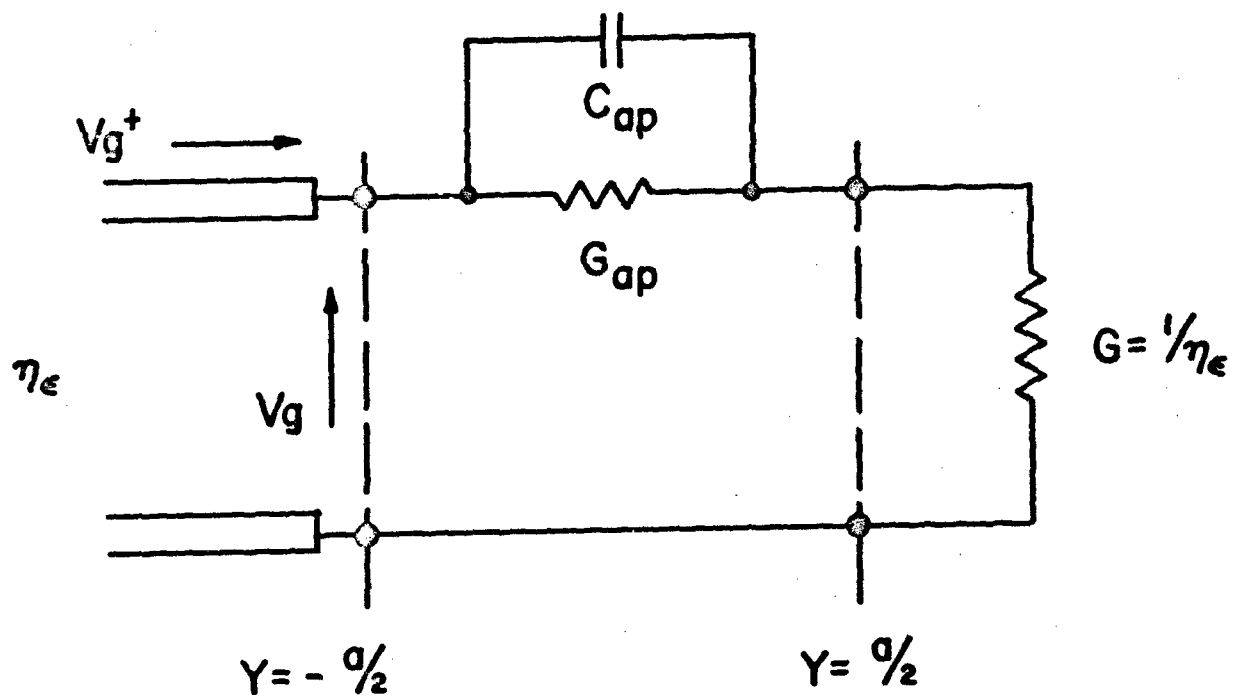


Figure 2-6 Approximate Aperture Equivalent Circuit

aperture voltage is then given by,

$$V_{ap} = \frac{Z_{ap}}{Z_{ap} + \eta_0} V_g = V_g - V_g^{i=1/2} \quad (2-21)$$

where

$$Z_{ap} = (G_{ap} + jB_{ap})^{-1}$$

Using the voltage expressions of (2-15) in the right hand side of (2-21) yields,

$$V_{ap} = V_g^i (1 - e^{-j\mu}) + a E_0 \epsilon_0 e^{-j\mu} \frac{\sin \mu}{\mu} \quad (2-22)$$

which for $\mu \ll 1$ becomes,

$$V_{ap} \approx a E_0 \epsilon_0 \quad (2-23)$$

The conductance, G_{ap} , is a radiation conductance determined by associating the radiated power as that carried in the surface wave mode. It follows that,

$$P_{rad} = |V_{ap}|^2 G_{ap} = 4A |E_0|^2 \quad (2-24)$$

Substituting (2-23) into (2-24) yields

$$G_{ap} = \frac{4A}{a^2 |E_0|^2} \quad (2-25)$$

Based on a knowledge of G_{ap} and B_{ap} , an explicit expression for the phase of E_0 is obtained. Using (2-12) and (2-13) in (2-21) and solving for V_g^{-s} yields

$$V_g^{-s} = \frac{Q + e^{-2j\mu} + 1}{2 - Q} \quad (2-26)$$

where $Q = Z_{ap}(G_{ap} + j\eta_0)$. V_g^{-s} is the $i = 0$ term of the summation in 2-15a thus, the phase of E_0 is,

$$\phi_0 = \angle V_g^{-s} + \mu - \phi_e \quad (2-27)$$

It is a simple matter now to recast the original field problem as a network. By assigning ports to phase planes $\pm a/2$ in the stripline and $x = 0^{\pm}$ in the slits and since the physical structures of both infinite and notch geometries are fully symmetric in z about the stripline center conductor, the network reduces to the four port shown in Figure 2-7. Normalizing the conservation of energy expression (equation 2-17) to the incident power we may make identifications for the scattering parameters of the four port network in Figure 2-7 for which we define:

$$\begin{pmatrix} V_1^- \\ V_2^- \\ V_3^- \\ V_4^- \end{pmatrix} = \underline{\underline{S}} \begin{pmatrix} V_1^+ \\ V_2^+ \\ V_3^+ \\ V_4^+ \end{pmatrix} \quad (2-28)$$

Thus,

$$S_{11} = \frac{V_1^-}{V_1^+} = \frac{V_1^-}{V_1^+} \Big|_{V_2^+ = V_3^+ = V_4^+ = 0} \quad (2-29a)$$

$$= \frac{a E_0 \epsilon_0}{2 \sqrt{Y_0}} e^{-j u} \frac{\sin u}{u}$$

$$S_{21} = \frac{V_2^-}{V_1^+} = \frac{V_2^-}{V_1^+} \Big|_{V_2^+ = V_3^+ = V_4^+ = 0} \quad (2-29b)$$

$$= 1 - S_{11}$$

$$S_{31} = \frac{V_3^-}{V_1^+} \Big|_{V_2^+ = V_3^+ = V_4^+ = 0} = \sqrt{a Y_0 A} \frac{E_0}{V_1^+} \quad (2-29c)$$

* The scattering parameters defined in equations 2-30 a,b,c are defined such that power is given by $V_n I_n^* = Y_n |V_n|^2$ where Y_n is the characteristic admittance of the line associated with port n.

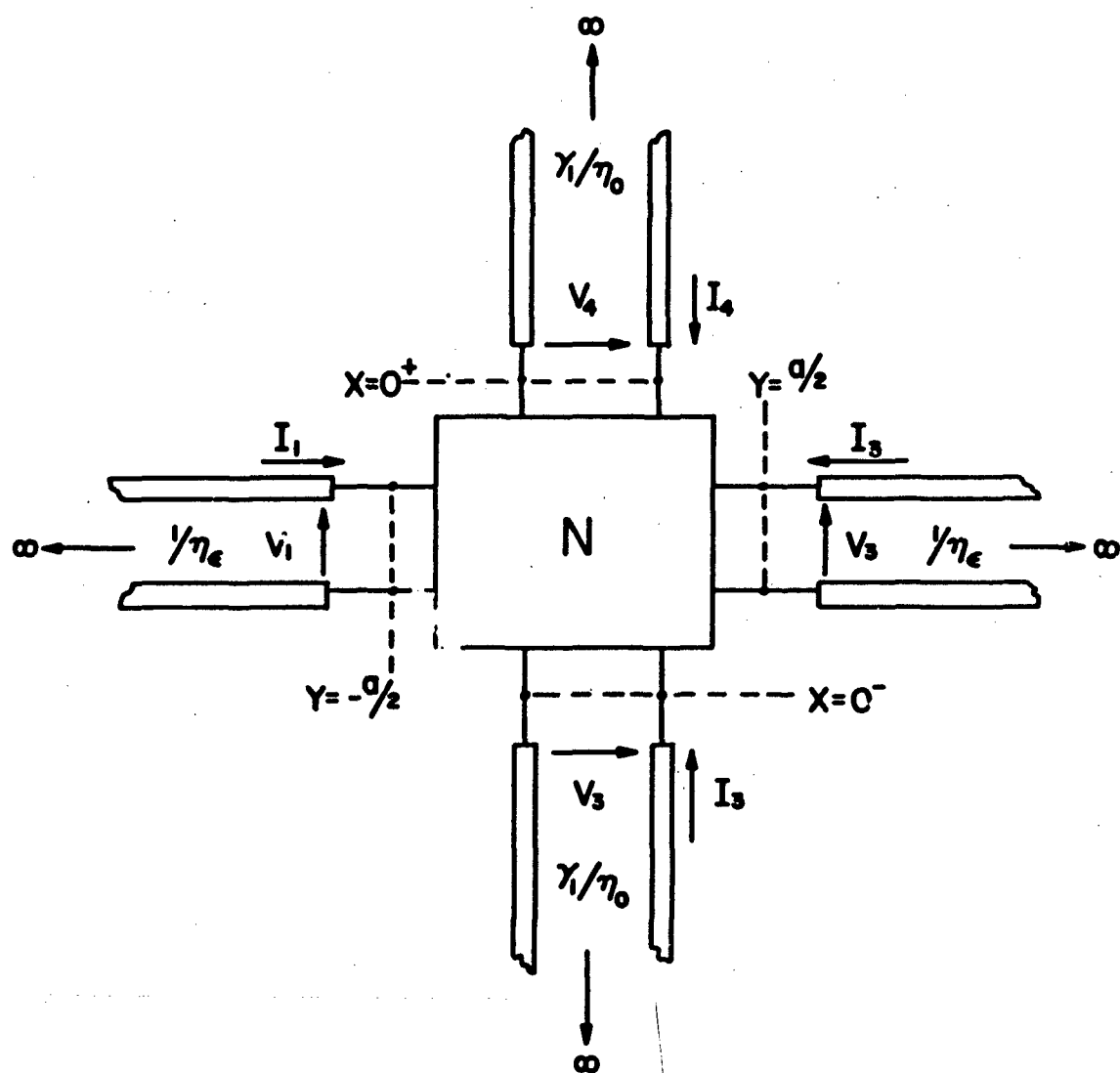


Figure 2-7 Network Representation of Infinite Slit
Infinite, Stripline Coupling Region

Requiring reciprocity and exploiting the symmetry of the structure the scattering matrix may be written as

$$\underline{\underline{S}} = \begin{pmatrix} S_{11} & S_{21} & \bar{\eta} S_{31} & -\bar{\eta} S_{41} \\ S_{21} & S_{11} & -\bar{\eta} S_{31} & -\bar{\eta} S_{41} \\ S_{31} & -S_{31} & S_{43} & S_{43} \\ S_{31} & -S_{31} & S_{43} & S_{43} \end{pmatrix} \quad (2-30)$$

where $\bar{\eta}$ is the ratio of surface wave admittance, $Y_s = k_x/k\eta_0$ to stripline wave admittance, $1/\eta_0$. Applying lossless conditions

$$S_{33} = \frac{1}{2} \frac{S_{31}(S_{21}^* - S_{11}^*)}{S_{31}^*} - 1, \quad (2-31)$$

and

$$S_{43} = 1 + S_{33} \quad (2-32)$$

The minus signs preceeding certain elements of the scattering matrix follow from reversal of direction of slit field via excitation of port 1 compared with that of port 2 (the stripline ports).

Figure 2-8 shows the frequency variation of $|S_{11}|$ and $|S_{31}|$ for a typical coupling region over a 3:1 frequency band. Both $|S_{11}|$ and $|S_{31}|$ are slowly increasing with a/λ , and the curves remain approximately parallel throughout. The conservation of energy statement of (2-17) may be rewritten in terms of the scattering parameters as

$$0 = |S_{11}|^2 - \operatorname{Re}\{S_{11}^*\} + \bar{\eta} |S_{31}|^2 \quad (2-33)$$

which shows that the phase of S_{11} must also be a slowly varying function of a/λ . In particular it is found that the phase of S_{11} for the parameters of Figure 2-8 is a slow monotonically

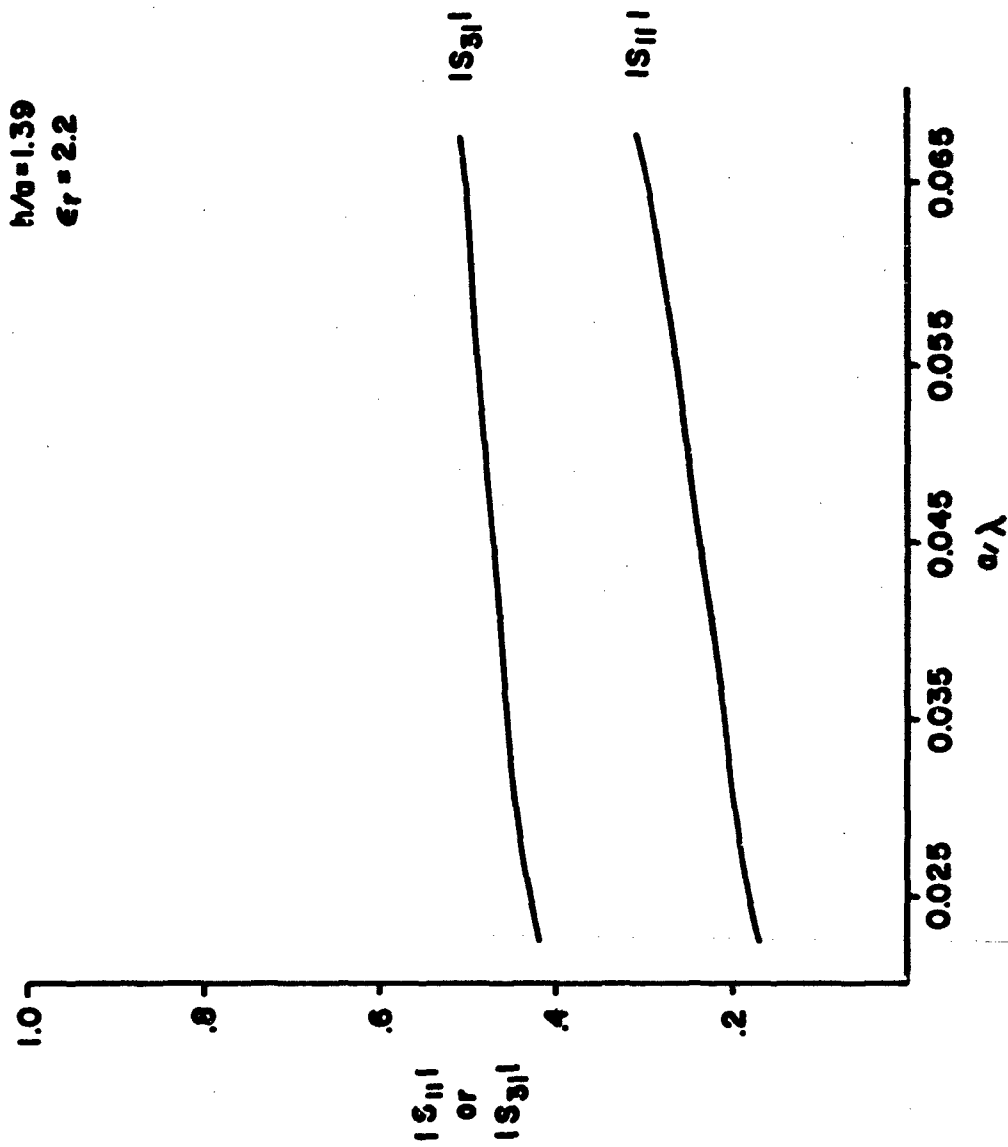


Figure 2-8 Modulus of Scattering Parameter S_{11} and S_{31} vs a/λ

decreasing function of a/λ as shown in Figure 2-9.

The scattering matrix developed above may be applied directly to the notch geometry (compare Figures 2-1 and 2-2) by including the notch and stripline terminations. Measured antenna reflection coefficient data indicates that the free-space transition and flare are well matched. Thus, an adequate model of the notch element (insofar as reflections back into the generator port are concerned) is that of Figure 2-10. This model consists of an open circuit terminated stripline (i.e. abruptly terminated stripline center conductor at $y = y_2$) and short circuit terminated (at $x = -x_2$) semi-infinite slit. These last two terminations are readily inserted into the scattering formulation via the relation of V_2^- and V_2^+ and V_3^- and V_3^+ as measured at the appropriate phase planes. That is, at $y = a/2$,

$$V_2^+ = \bar{\Gamma} V_2^- e^{-jk_0(2y_2-a)} = \alpha V_2^- \quad (2-34)$$

and at $x = 0$,

$$V_3^+ = -V_3^- e^{jk_0 x_2} = \beta V_3^- \quad (2-35)$$

In equation 2-34, the reflection coefficient $\bar{\Gamma}$ has a modulus 1 and phase slightly different from zero, corresponding to a small translation of the open circuit plane from the physical location of the termination, (slight phase shift due to fringing capacitance). $\bar{\Gamma}$ is given by

$$\bar{\Gamma} = - \frac{\tan k_0 c + jt}{\tan k_0 c - jt} \quad (2-36) *$$

where

$$t = \frac{4C + 2W}{C + 2W}$$

$$c = \frac{h \ln 2}{\pi}$$

* For detailed discussion of $\bar{\Gamma}$, see Altshuller and Oliner, [6].

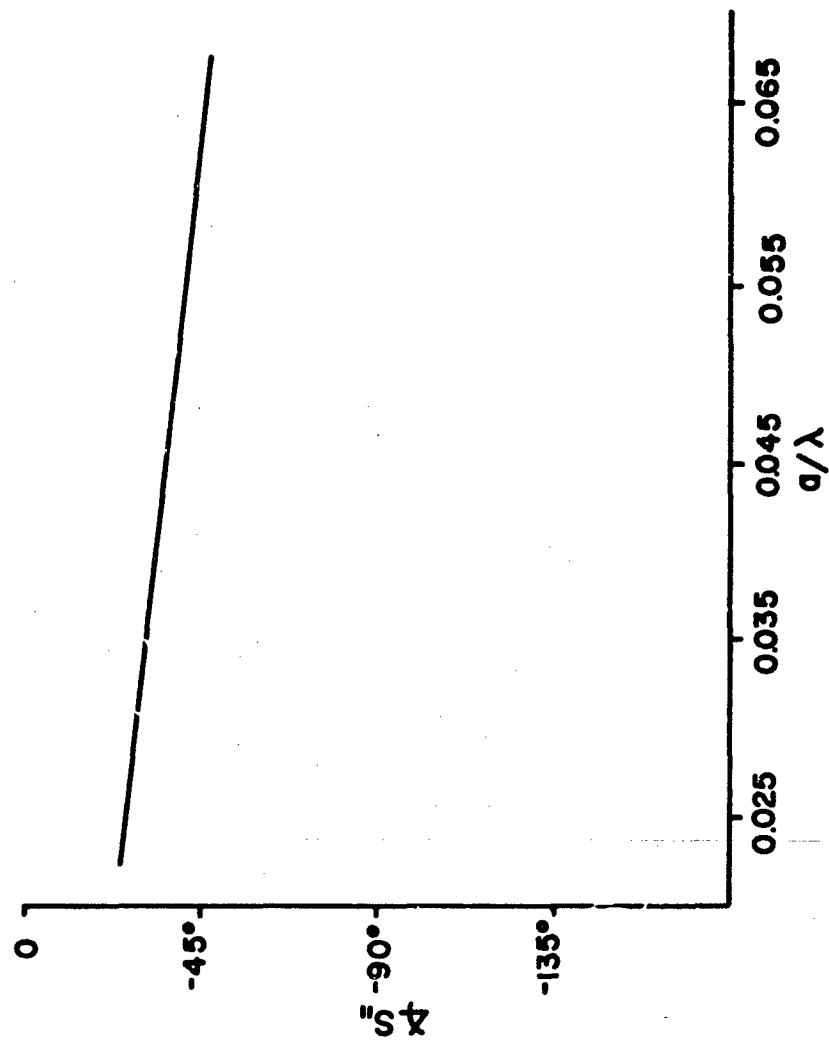


Figure 2-9 Phase of Scattering Parameter S_{11}

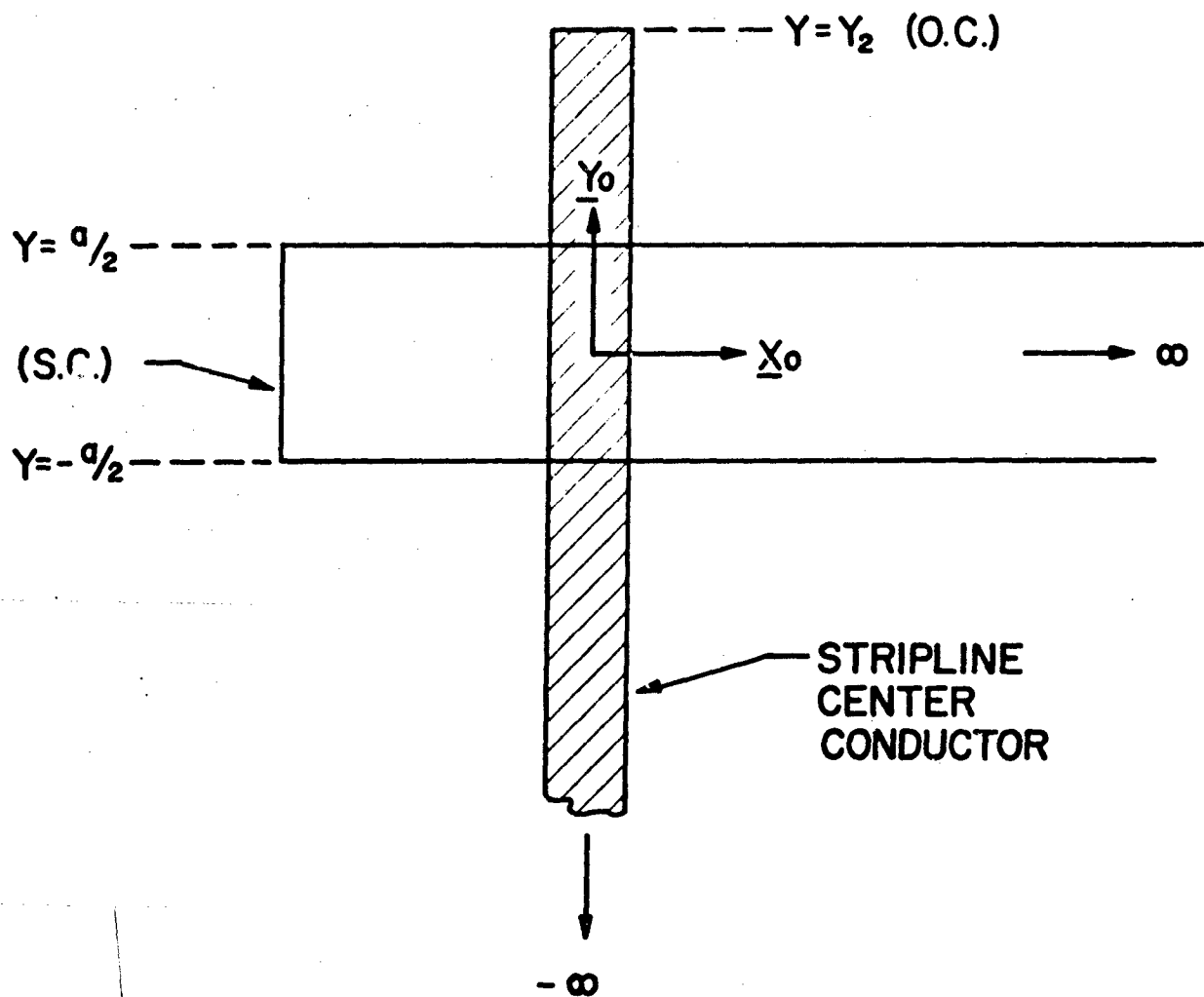


Figure 2-10 Approximate Model of Notch Element
with Open and Short Circuit Terminations

and w and h are the stripline center conductor width and plate spacing, respectively.

Similarly, a translation of the slit short circuit plane might be expected since (as will be discussed in Chapter III) the surface waves are not tightly bound to the slit plane. However, excellent agreement with measured reflection coefficient suggests that this translation is negligible.

By inserting (2-34) and (2-35) into (2-29) the matrix equation maybe reduced to two equations in the unknowns V_1^- and V_4^- ($V_4^+ = 0$ since reflection at the flare is assumed negligible), with V_2^- , V_2^+ , and V_3^+ determined directly. Thus,

$$V_1^- = S_{11} V_1^+ + S_{21} V_2^+ + \bar{\gamma} S_{31} V_3^+ \quad (2-37)$$

$$V_4^- = S_{31} V_1^+ - S_{31} V_2^+ + S_{33} V_3^+ \quad (2-38)$$

where

$$\begin{aligned} V_3^+ &= -V_3^- e^{2jk_0 x_2} = \rho V_3^- \\ &= \rho S_{31} [1 - \alpha] / [(1 - \alpha S_{11})(1 - \rho S_{33}) - \alpha \bar{\gamma} S_{31}^2] \end{aligned}$$

$$\begin{aligned} V_2^+ &= \bar{\Gamma} e^{-jk_0 (x_2 - a)} V_2^- = \alpha V_2^- \\ &= \alpha (S_{21} - \bar{\gamma} \rho S_{31} V_3^+) / (1 - S_{11}) \end{aligned}$$

From equations 2-35 and 2-36, the antenna reflection and transmission coefficients are

$$\Gamma = \frac{V_1^-}{V_1^+} = S_{11} + S_{21} \frac{V_2^+}{V_1^+} + \bar{\gamma} S_{31} \frac{V_3^+}{V_1^+} \quad (2-39)$$

and

$$T = \frac{V_4^-}{V_1^+} = S_{31} - S_{21} \frac{V_2^+}{V_1^+} + S_{43} \frac{V_3^+}{V_1^+} \quad (2-40)$$

Examination of equations (2-37) - (2-40), shows that, since the scattering parameters are essentially constant over wide frequency ranges, the locations of the open and short circuit planes are critical if broadband operation is to be achieved. In particular, if the open circuit plane is moved to $Y_2 = a/2$, $\alpha \rightarrow 1$ (independent of frequency), $V_3^+ = V_3^- = 0$, $V_2^+ = V_2^- = 1$ and $\Gamma \rightarrow +1$. Similarly, if $x_2 = 0$, $\beta \rightarrow -1$, and $\Gamma \rightarrow +1$ for $\alpha = 1$. In this latter case, Γ would oscillate rapidly if $y_2 \gg \lambda$. Figures 2-11 and 2-12 show $|\Gamma|$ as a function of a/λ with parameters y_2/a and x_2/a , respectively. In Figure 2-11, y_2/a has been taken over a wide range of values to indicate the type of behavior discussed above. In particular, for the larger values of y_2/a , increasing variations of $|\Gamma|$ are observed, with $|\Gamma| = 1$ for $\alpha = 1$. When y_2/a is too small with respect to x_2/a , there is a strong phase imbalance in the contribution of the last two terms of equation 2-39 and $|\Gamma|$ remains constantly large.

In Figure 2-12 x_2/a has been varied $\pm 20\%$, with y_2/a fixed. The change in parameter has relatively minor effect. However, it should be noted that there is a general tendency for the level to rise as x_2/a departs significantly from the value y_2/a .

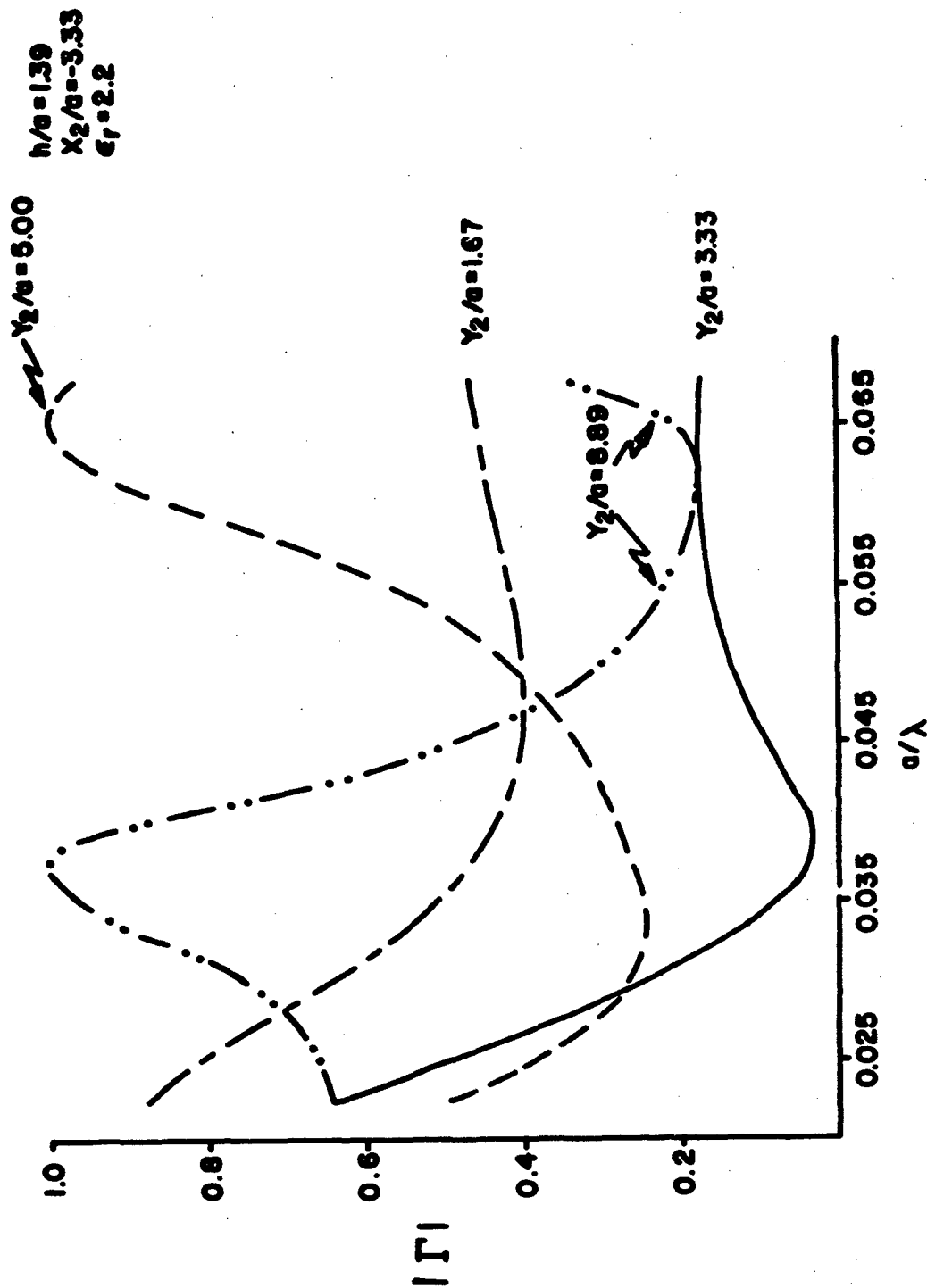


Figure 2-11-Reflection Coefficient $\sqrt{a/\lambda}$
 - Parameter Y_2/a

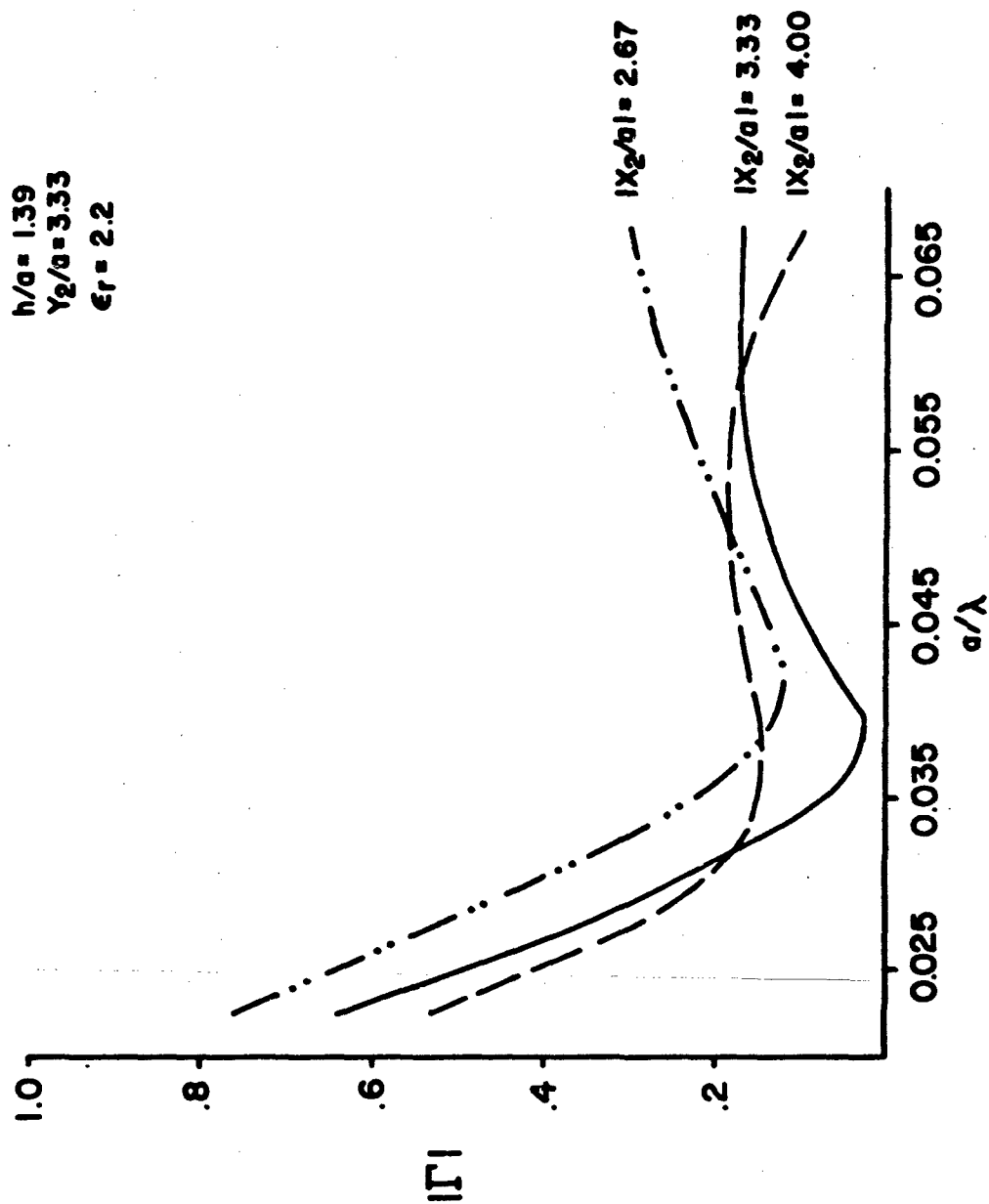


Figure 2-12 Reflection Coefficient vs a/λ
 -Parameter x_2/a

2.2 Calculations and Measurements of Isolated Notch Antenna

In the previous section, it was shown that the broadband properties of the notch antenna are associated with the nature of the coupling region and the relative locations of the open and short circuit terminal planes. In this section, measured and computed active reflection coefficient are compared. The agreement between experiment and theory is very good. The broadband behavior is clearly demonstrated and correlates well with measurements. Some deviation occurs where the theory predicts the occurrence of a low frequency cut-off somewhat higher in frequency than is found experimentally.

Six notch elements have been selected for discussion. The configuration is shown in Figure 2-13, and the dimensions of the six elements are given with respect to free-space wavelength at low frequency, f_0 , Table II-1. All elements are etched on .03125" Duroid ($\epsilon_r = 2.2$), giving stripline plate spacing of .0625".

Measure and calculated reflection coefficient for elements 5 and 6 are shown in Figures 2-14 and 2-15 respectively. Both elements are well matched over greater than 2:1 frequency bands. For both elements, a low frequency cut-off is predicted by the calculations. This cut-off has been observed experimentally at slightly lower frequencies. Over the remainder of the frequency bands, the agreement is quite good. Calculations for these elements have shown that they remain well matched at frequencies well above the range of experimental data.

Figure 2-16 shows measured reflection coefficient elements 1 and 2 for an approximate 3:1 frequency band. The elements differ only in length of flare, x_0 , and flare radius of curvature, R (see Figure 2-13 and Table 2-1). Both elements are poorly matched over the entire band, however, the data indicates certain characteristics of practical interest to designers. First, the shapes and levels of the curves are approximately the same

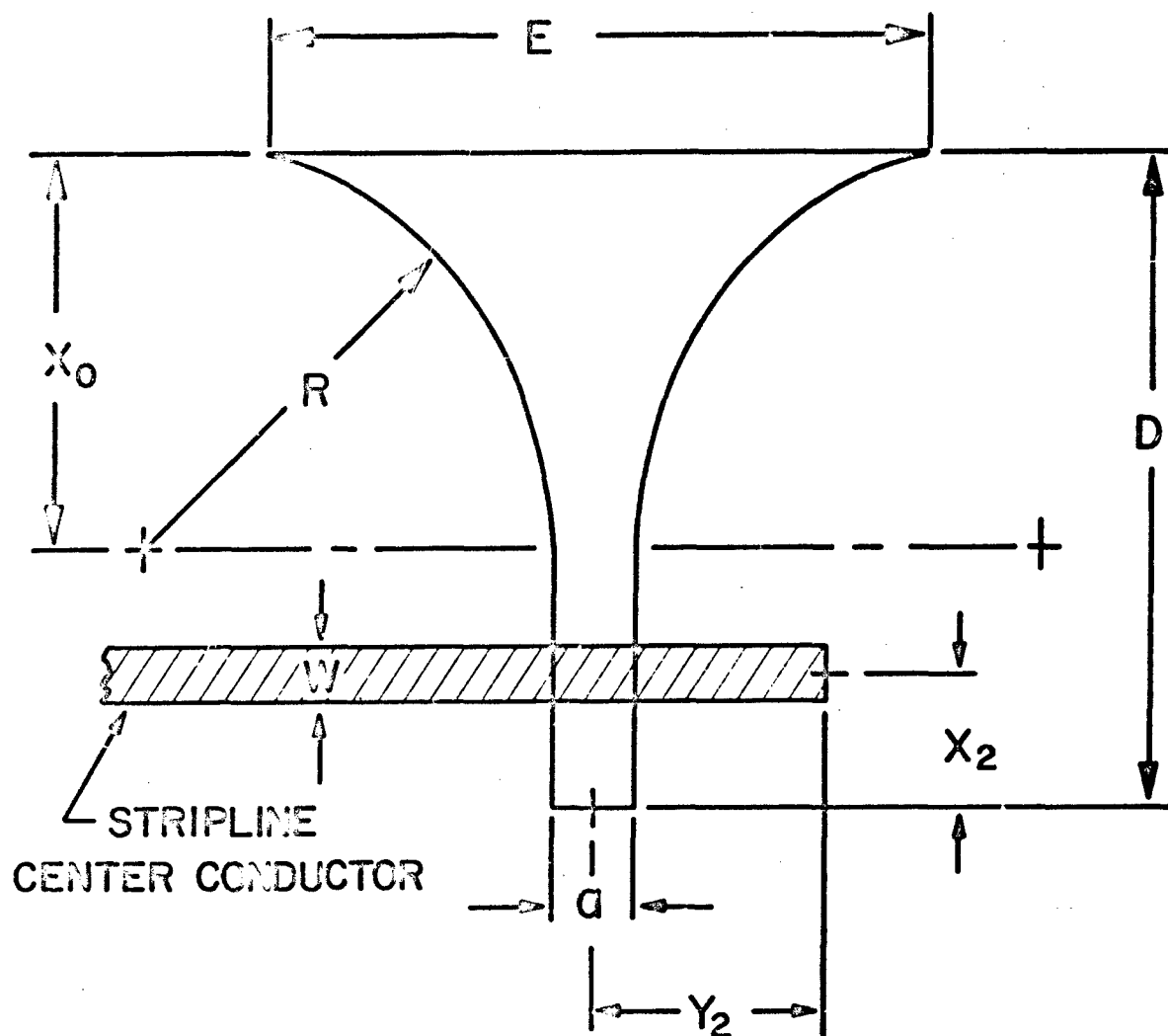


Figure 2-13 Notch Element Geometry

Element	E/λ_0	D/λ_0	R/λ_0	a/λ_0	x_0/λ_0	x_2/λ_0	y_2/λ_0	w/λ_0
1	.1875	.150	.1558	.0225	.138	-.025	0.20	.010
2	.1875	.1875	.1019	.0225	.100	-.025	0.20	.010
3	.150	.1875	.1802	.0225	.138	-.025	0.20	.010
4	.225	.1875	.1440	.0225	.138	-.025	0.20	.010
5	.1875	.1875	.1180	.0225	.113	-.075	0.075	.010
6	.300	.1875	.1465	.0225	.125	-.0625	0.0810	.0113

TABLE 2-1

Element Dimensions with Respect to λ_0 at Low Frequency

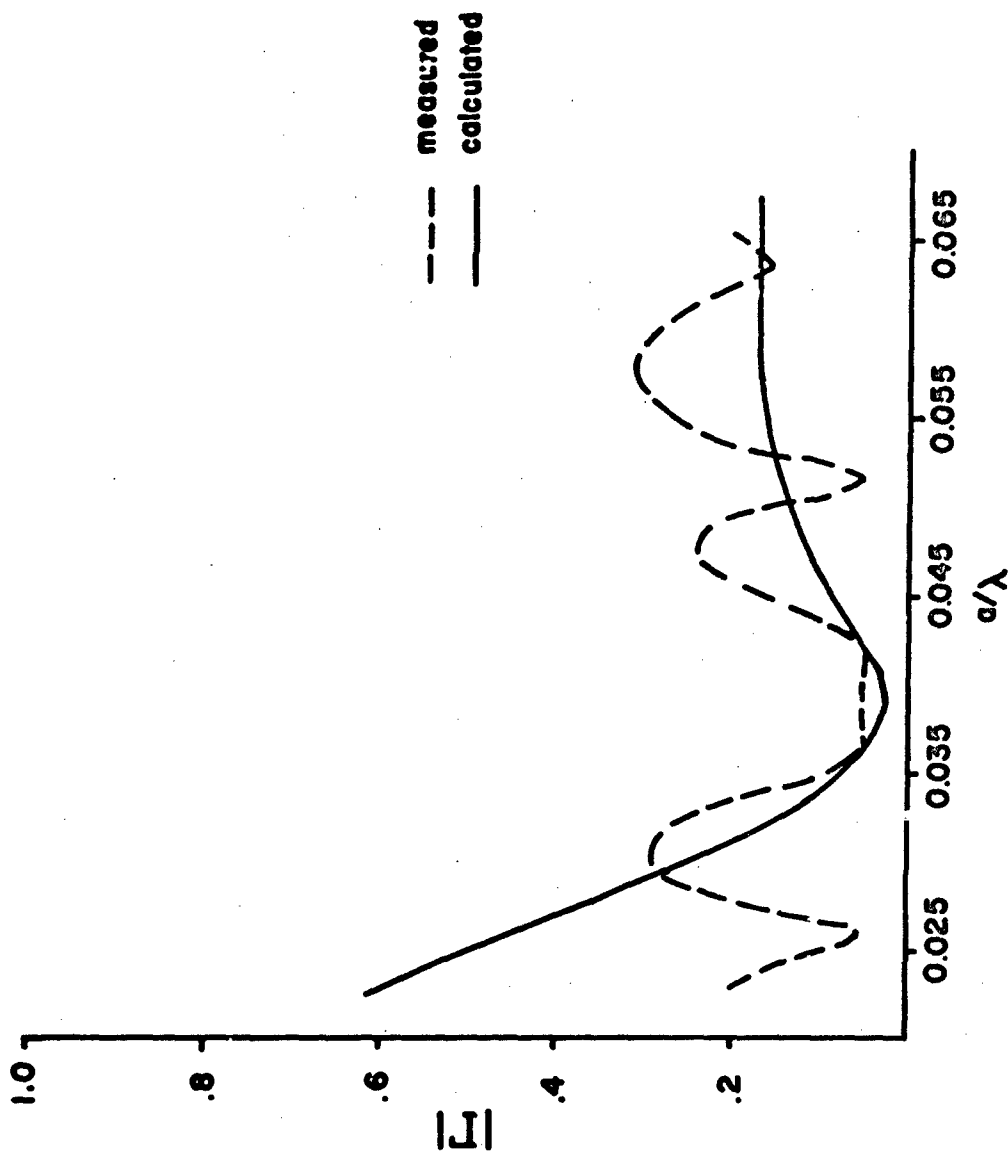


Figure 2-14 Measured and Calculated $|\Gamma|$ vs a/λ
Element #5

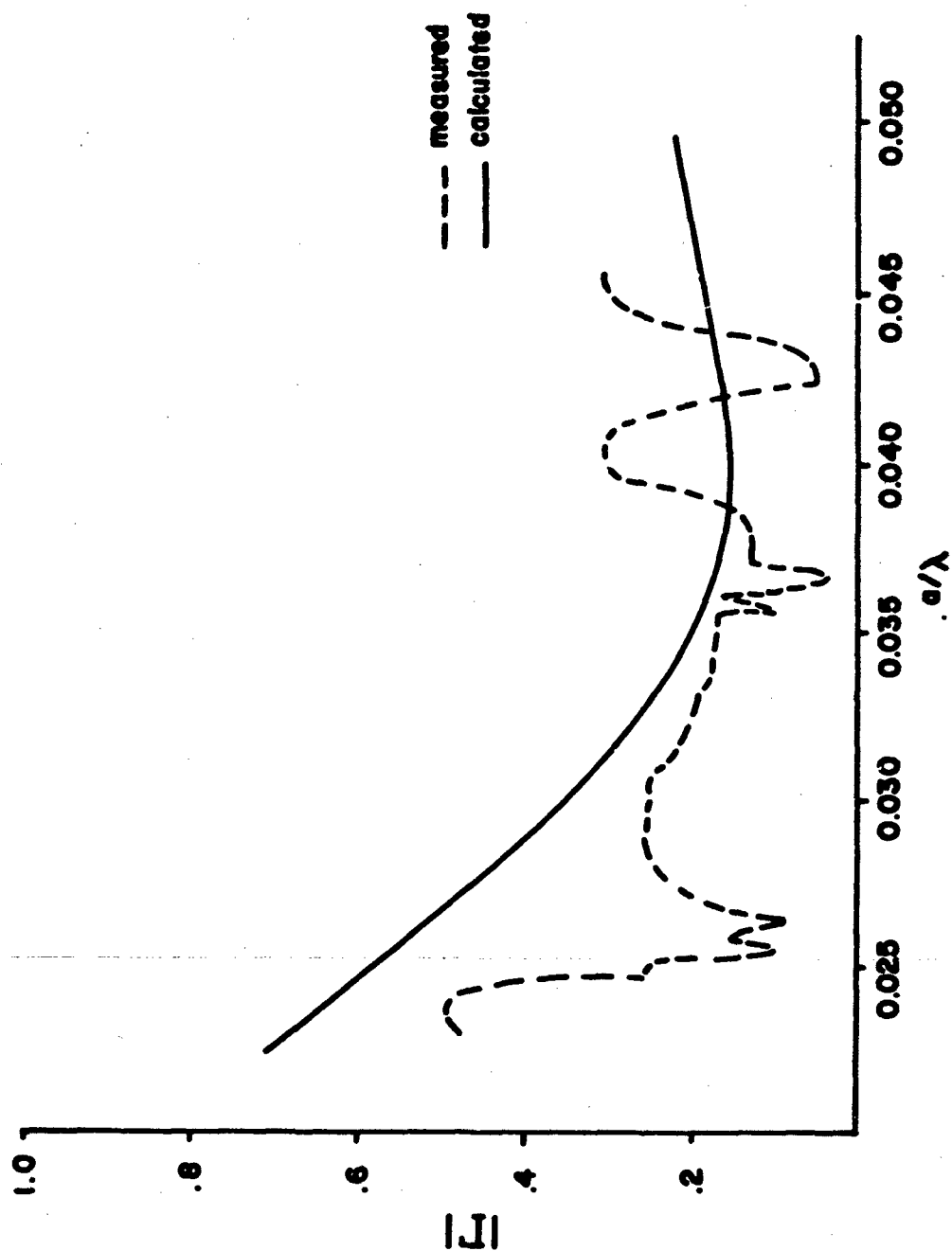


Figure 2-15 Measured and Calculated $|\Gamma|$ vs a/λ
Element #6

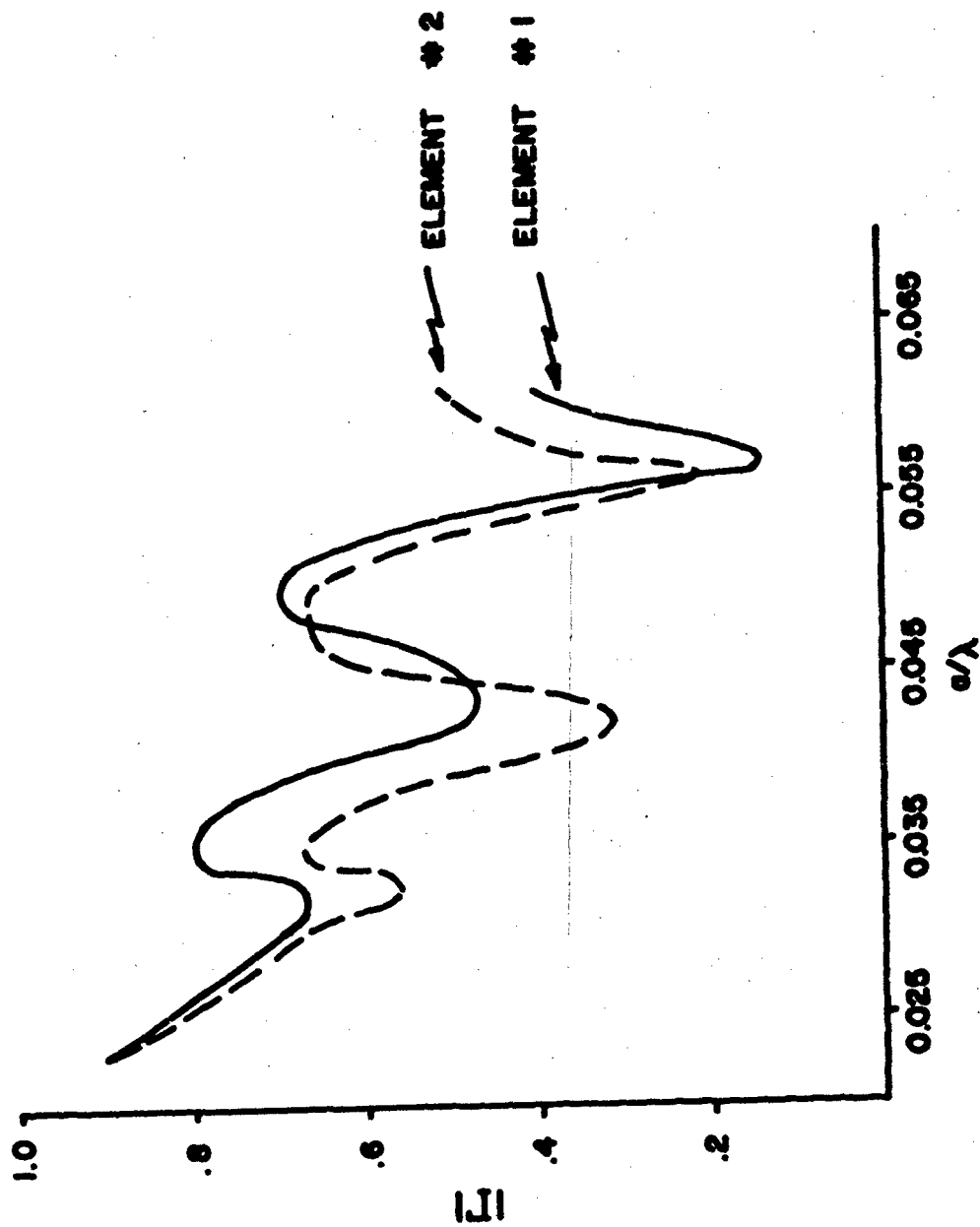


Figure 2-16 Measured $|\Gamma|$ vs a/λ Elements 1 and 2

and show no translation, indicating that the length of flare is not a significant consideration for element design. That element 2 is somewhat better matched over a segment of the band, suggests that the more rapid discontinuity looking into the flare may have some advantageous consequences, though it seems fairly apparent from previous experience that the slower transition is more desirable. Secondly, the first humps in the curves occur that $(y_2 - a/2)/\lambda_g \approx .5$, or $\alpha \approx 1$. The second humps are due to the close-in notch short circuit. To further illustrate that the influence of the flare is negligible, measured reflection coefficient is shown in Figure 2-17 for elements 1, 3, and 4. These elements differ only in the E and R dimensions.

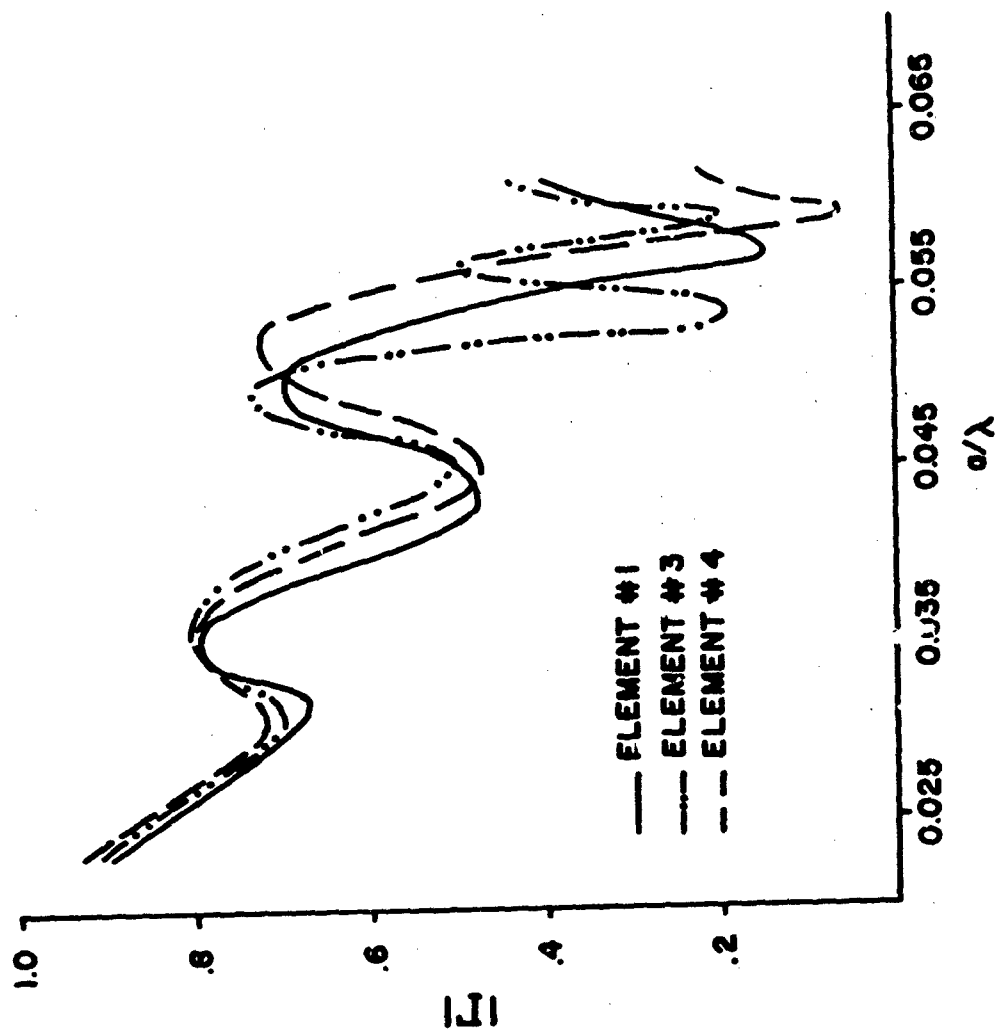


Figure 2-17 Measured $|\Gamma|$ vs a/λ
 Elements 1, 3, and 4

3. GUIDED WAVES OF SLITTED PARALLEL PLATES

The mechanism for radiation in the notch antenna is associated primarily with the guided wave properties of the slitted parallel plate region. The piece-wise extensions of modal solutions for infinite strips (constant width) of this slitted guide well approximate the field distribution and match in a slowly varying flare with the same transverse cross section. A similar approximation was used in determining dielectric wedge radiation for extending array coverage using dielectric sheaths.^[7]

The slitted parallel plate configuration is shown in Fig. 3-1. The resonant solutions (guided modes) correspond to either open or short circuits at the symmetry plane, $y = -h/2$. For the case of stripline TEM mode excitation of the notch antenna the short circuit modes are decoupled and do not contribute to the radiation field or junction susceptance. The geometry of concern here is simplified to the open circuit symmetry as shown in Fig. 3-2. The guided wave spectrum are the wavenumbers k_{xn} which are dependent on k and slit width a . A dispersion relation for k_x as a function of k is required.

The method of determining the dispersion relation, $D(k_y, k; a) = 0$, assumes a uniform (in y) travelling wave field along x in the slit and enforces conservation of complex power per unit length of slit at the $z = 0$ (slit) discontinuity. The total transverse electric field in the plane of $z = 0$ is assumed to be,

$$E_t = E_y y_2 = E_0 e^{-jk_x x} P(y) y_0 \quad (3-1)$$

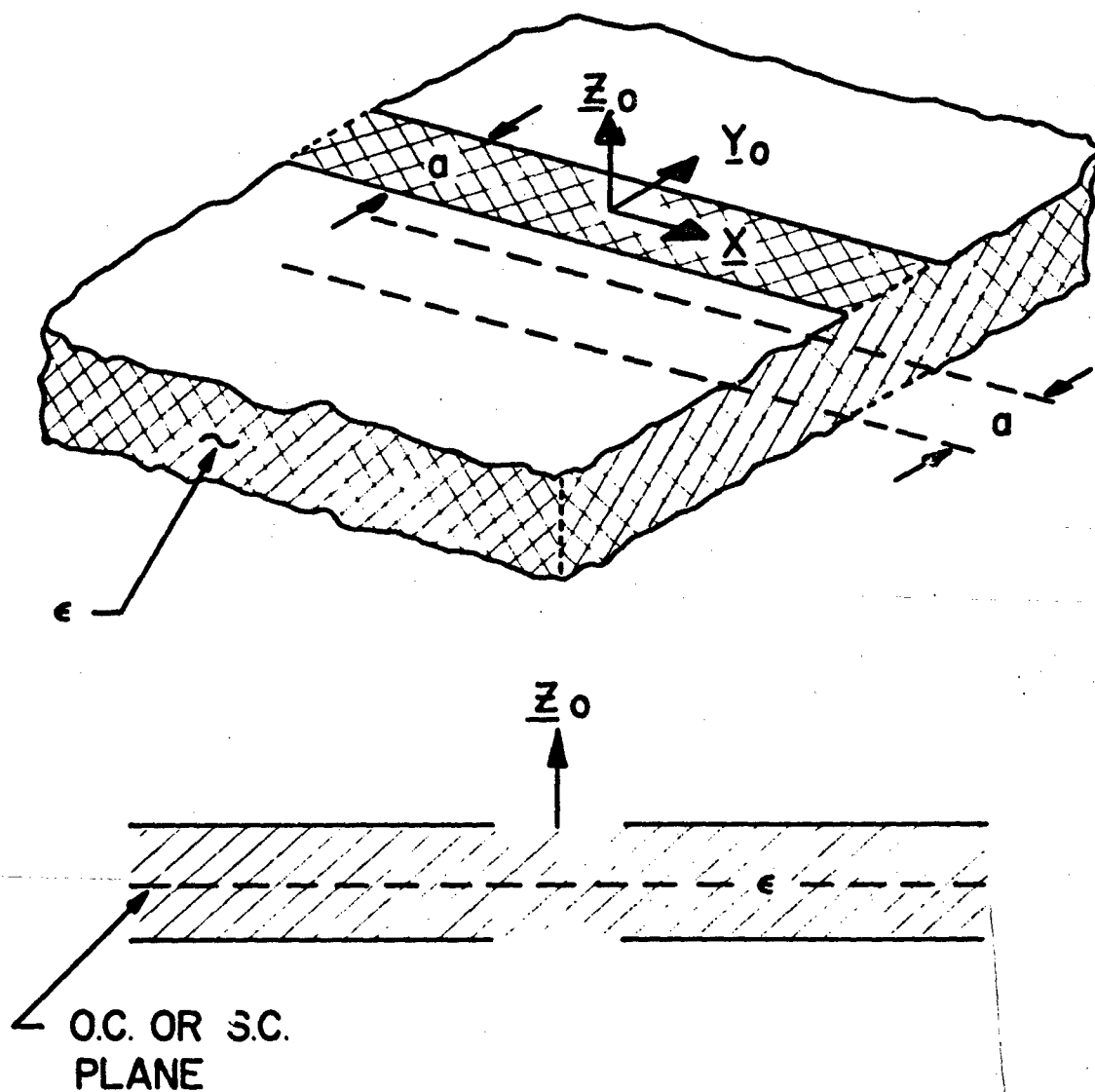


Figure 3-1 Slitted Parallel Plate Region

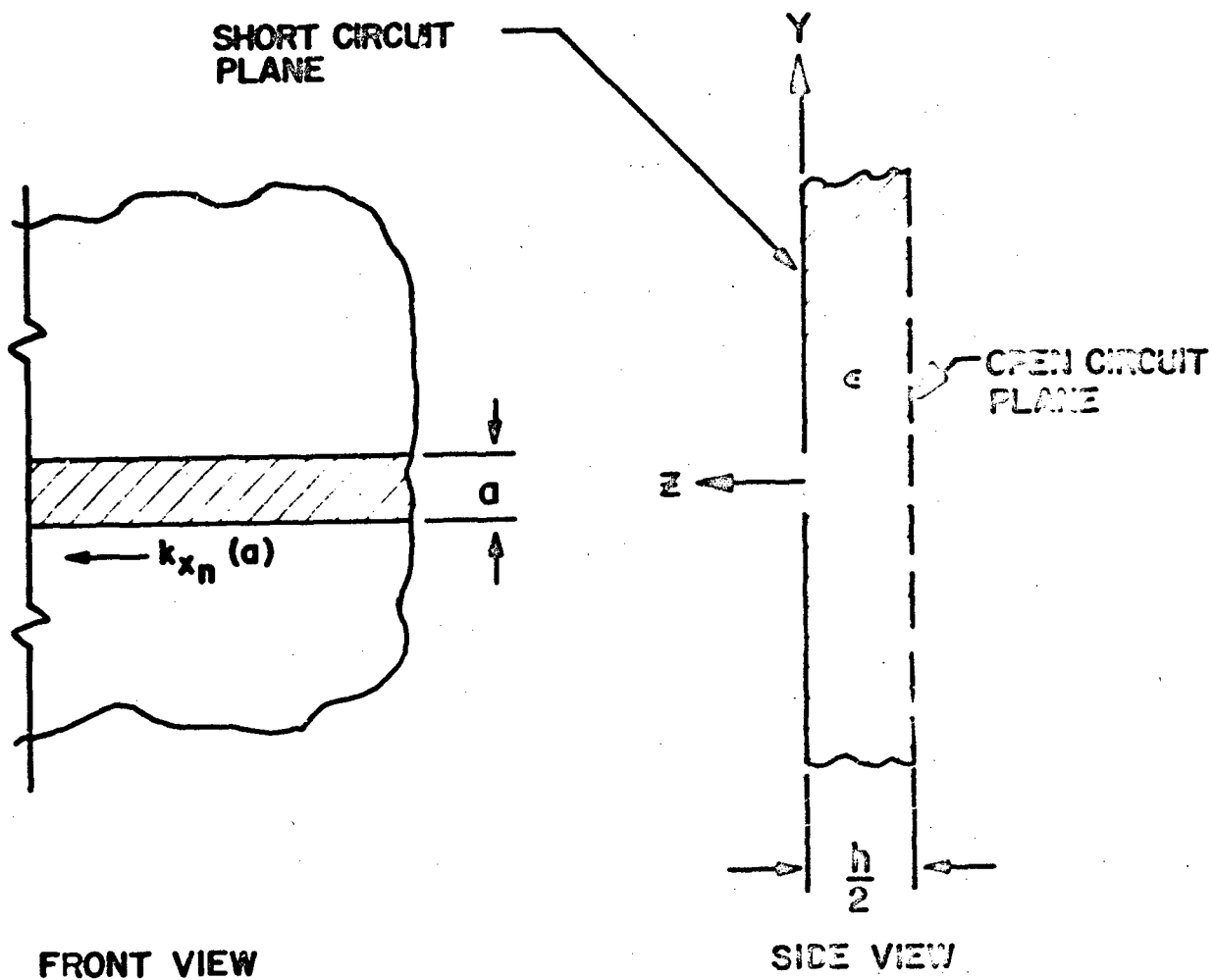


Figure 3-2 Strip Geometry for Determination of Leaky Wave Spectrum, $k_{x_n}(a)$

where $P(y)$ is a pulse function given as unity in $y \leq |y/2|$ and zero otherwise.

3.1 Complex Power $z = 0^+$

The assumed transverse electric field in the aperture is E_y only; thus the complex power leaving the $z = 0$ interface ($z = 0^+$) is

$$P_z = \int_S E_y(0^+) y_z \times H_x^*(0^+) x_z \cdot z_z dS, \quad (3-2)$$

where S is the infinite extent of the plane $z = 0$. The assumed guided wave is TE with respect to x and may be derived from a longitudinal magnetic field H_x . For the single mode excitation of k_x the magnetic field $H_x(x, y, z)$ can be defined in terms of the transform $h(k_y)$ as,

$$H_x(x, y, z) = \frac{e^{-jk_x x}}{2\pi} \int_{-\infty}^{\infty} h(k_y) e^{-jk_y y} e^{-j\sqrt{k^2 - k_x^2 - k_y^2} z} dk_y \quad (3-3)$$

The electric field, E_y , in terms of H_x (for $E_x = 0$) is via Maxwell's equations,

$$E_y = \frac{-j\omega\mu}{k^2 - k_x^2} \frac{\partial H_x}{\partial z} \quad (3-4)$$

Using (3-3) in (3-4) yields,

$$E_y(x, y, z) = \frac{-j\omega\mu}{k^2 - k_x^2} \frac{e^{-jk_x x}}{2\pi} \int_{-\infty}^{\infty} \sqrt{k^2 - k_x^2} h(k_y) e^{-jk_y y} e^{-j\sqrt{k^2 - k_x^2 - k_y^2} z} dk_y, \quad (3-5)$$

where

$$k_t^2 = k_x^2 + k_y^2 \quad (3-6)$$

The magnetic field transform $h(k_y)$ is determined as a result of comparing the electric field in a transform representation in equation (3-5) with the assumed form of \underline{E} in equation (3-1) at $z = 0$. Whence,

$$E_y(z=0) = E_0 e^{-jk_x x} P_{iy} = \frac{-\omega \mu}{k^2 - k_t^2} e^{-jk_x x} \left\{ \frac{1}{2\pi} \int_{-\infty}^{\infty} \sqrt{k^2 - k_t^2} h(k_y) e^{-jk_y y} dk_y \right\} \quad (3-7)$$

The term of (3-7) in parenthesis is identified as the transform of $\sqrt{k^2 - k_t^2} h(k_y)$. Taking the inverse transform of both sides of (3-7) yields a simple equation for $h(k_y)$, as:

$$\sqrt{k^2 - k_t^2} h(k_y) = - \frac{(k^2 - k_x^2)}{\omega \mu} E_0 \int_{-\infty}^{\infty} P_{iy} e^{jk_y y} dy \quad (3-8)$$

from which:

$$h(k_y) = \frac{a E_0}{\omega \mu} \frac{(k_x^2 - k^2)}{\sqrt{k^2 - k_t^2}} \frac{\sin k_y y/2}{k_y y/2} \quad (3-9)$$

The complex power equation of (3-2) is written in terms of $h(k_y)$ using (3-3) and (3-5) as,

$$P_{>}(z=0^+) = \frac{-\omega\mu}{k^2 - k_x^2} \left(\frac{1}{2\pi}\right)^2 \int_{-\infty}^{\infty} \int_{-\infty}^{\infty} dk_y dk_y' h(k_y) h(k_y') \sqrt{k^2 - k_y^2} e^{-j(k_y - k_y')y} \quad (3-10)$$

The integral on y only has a contribution at $k_y = k_y'$; specifically,

$$\int_{-\infty}^{\infty} e^{-j(k_y - k_y')y} dy = 2\pi \delta(k_y - k_y') \quad (3-11)$$

The indicated identity of (3-11) and the result of (3-9) used in (3-10) with an integration on k_y yields

$$P_{>}(z=0^+) = \frac{-|E_0|^2 \omega^2}{2\pi \omega\mu} \frac{|k_x^2 - k^2|^2}{k^2 - k_x^2} \int_{-\infty}^{\infty} \frac{1}{(\sqrt{k^2 - k_y^2})^4} \frac{\sin^2 k_y y/2}{(k_y y/2)^2} dk_y \quad (3-12)$$

Rewriting (3-12) using the even symmetry in k_y gives,

$$P_{>} = \frac{|E_0|^2}{\pi k \eta_0} (k_x)^2 \left(\left(\frac{k_x}{k} \right)^2 - 1 \right) \int_0^{\infty} \frac{dk_y}{(\sqrt{k^2 - k_y^2})^4} \frac{\sin^2 k_y y/2}{(k_y y/2)^2} \quad (3-13)$$

where $\eta_0 =$ free space impedance 377Ω .

Since the orthogonality condition for the leaky modes is obtained by extension into the complex plane, the integral on x has been eliminated. Thus $P_{>}$ has units power per unit length of slit.

The integral in (3-13) in general requires numerical solutions for an arbitrary choice of parameter ka . However, for small slits $ka \ll 1$, asymptotic expressions can be derived.

An alternative form of the integral in equation 3-13 is obtained via the following representation of the Hankel function $H_0^{(2)}(kR)$: [8]

$$H_0^{(2)}(kR) = H_0^{(2)}(k|y-y'|) = \frac{1}{\pi} \int_{-\infty}^{\infty} dk_y \frac{e^{-jk_y(y-y')}}{\sqrt{k^2 - k_y^2}} \quad (3-14)$$

Taking successive integrals in y and y' reproduces the integral of interest:

$$\frac{\pi}{2a^2} \int_{-a/2}^{a/2} dy \int_{-a/2}^{a/2} dy' H_0^{(2)}(k|y-y'|) = \int_0^{\infty} \frac{dk_y}{\sqrt{k^2 - k_y^2}} \frac{\sin^2 k_y a/2}{(k_y a/2)^2} \quad (3-15)$$

The transformation $k^2 \rightarrow k^2 - k_x^2$ is valid due to the separability of the wave equation. The left hand side of (3-15) can thus be used for the integral of (3-13) with $k \rightarrow \sqrt{k^2 - k_x^2}$. For small ka , the small argument approximation of the Hankel function permits a simple integration:

$$H_0^{(2)}(k|y-y'|) \sim 1 - j \frac{2}{\pi} \ln(k|y-y'|) \quad (3-16)$$

The computed solution for complex power (i.e. dispersion relation for k_x) used these asymptotic forms to facilitate numerical results.

Since the integration on the right hand side (RHS) of equation 3-15 is along the real axis, the square root appearing in the integral may be analytically continued into the complex plane. Provided that $\text{Im}\{k_x\} \neq 0$ the conjugated square root appearing in equation 3-13 may be expressed as $\sqrt{k^2 - k_1^2 - (k_x^)^2}$. Thus for $k \rightarrow \sqrt{k^2 - (k_x^*)^2}$, the RHS of equation 3-15 reduces to the integral in equation 3-13.

For $k_x = 0$, the integral expression for complex power, equation 3-13, reduces identically to that given by Harrington [9] for the power per unit length transmitted by an aperture when excited by a normally incident plane wave. As a check on the validity of the numerical techniques employed in the evaluation of P_z the integration was carried out for $k_x = 0$. The results obtained were exactly those published by Harrington.

3.2 Complex Power $z = 0^-$

To determine an expression for the complex power flow in z at $z = 0^-$ a suitable representation for the fields in $-h/2 < z < 0^-$ is needed. In contrast to the external problem ($z > 0$), the fields in this bounded (in z) region can be expressed as a discrete modal series. The aperture fields for $z = 0^-$ are formed by matching electric and magnetic fields in the slit to a guided wave representation of modes that propagate in the y direction between the plates. In this fashion a rapidly convergent series for aperture magnetic field is formed and a corresponding closed form series for complex power is determined.

Making use of the equivalence theorem, the assumed aperture electric field E_{ap} is equivalently a magnetic current M applied to the closed parallel plate region in $-\frac{h}{2} < z < 0$. This equivalent current source couples to the modes of the parallel plate geometry. In particular, for this aperture in the waveguide wall with uniform field in y , (longitudinal slit) the coupling mechanism is a series voltage source for each of the discrete modal transmission lines. The coupled traveling wave mode amplitudes (transmission line voltages and currents) are found by applying the equivalent voltage excitation to an appropriate transmission line Green's function for the series source. The

aperture magnetic field is then determined as the series sum of magnetic mode functions and modal current amplitudes, taken in the aperture plane.

The equivalent magnetic current for the assumed aperture electric field, \underline{E}_{ap} , is

$$\underline{M}(x, y, z) = \underline{E}_{ap} \times \underline{\hat{z}} = x_0 E_0 e^{-jk_x x} p(y) h(z) \quad (3-17),$$

where $\delta(z)$ is the Dirac-delta function. For the fields in $z < 0$ bounded by the reactive planes at $z = 0$ and $z = -h/2$ the electric wall may be closed and sustain \underline{M} in the aperture region to be equivalent to the original problem. In following the prescription outlined above, this equivalent current source is put in a representation in terms of modes of the parallel plate structure,

$$\underline{M}(x, y, z) = \sum_i v_i(y) \underline{h}_i(x, z) \quad (3-18).$$

In this representation \underline{h}_i are the transverse, to y , mode functions and $v_i(y)$ are scalar voltage amplitudes, interpreted as series voltage sources in the transmission line media of modal lines characterized by $\underline{h}^{(2)}$.

The orthonormal transverse to y mode functions in the parallel plate region of open and short circuit walls as derived in Appendix C are given below as:

$$\underline{e}_n' = \sqrt{\frac{2}{\pi h}} \frac{e^{-jk_x x}}{k_{tn}} \left[-jk_x \frac{\sin((2n+1)\pi z/h)}{h} x_0 - \frac{(2n+1)\pi}{h} \cos\left(\frac{(2n+1)\pi z}{h}\right) z_0 \right] \quad (3-19)$$

$$\underline{h}_n' = \underline{y}_e \times \underline{e}_n' \quad (3-20)$$

for E-modes, with $k_{tn} = \sqrt{k_x^2 + \left(\frac{(2n+1)\pi}{h}\right)^2}$

and

$$\underline{h}_m' = \sqrt{\frac{2}{\pi h}} \frac{e^{-jk_{tm}y}}{k_{tm}} \left[-jk_x \cos\left(\frac{(2m+1)\pi}{h}z\right) \underline{x}_e + \frac{(2m+1)\pi}{h} \sin\left(\frac{(2m+1)\pi}{h}z\right) \underline{z}_e \right] \quad (3-21)$$

with

$$\underline{e}_m' = \underline{h}_m' \times \underline{y}_e \quad (3-22)$$

for H-modes.

The mode functions (3-19), (3-20), (3-21) and (3-22) form a complete orthonormal set such that,*

$$\int_{C_s} \underline{e}_i \cdot \underline{e}_j^* dC_s = \int_{C_s} \underline{h}_i \cdot \underline{h}_j^* dC_s = \delta_{ij} \quad (3-23)$$

*The orthogonality of the mode function is established via extension of the result for k_x real into the complex plane.

or

$$\int_{C_s} \underline{e}_i \times \underline{h}_j^* \cdot \underline{y}_z dC_s = \delta_{ij} \quad (3-24)$$

where

$$\delta_{ij} = \begin{cases} 0 & , i \neq j \\ 1 & , i = j \end{cases} .$$

The cross section of the transverse plane, C_s , includes the infinite x dimension and the region $-\frac{h}{2} < z < 0^-$. The dispersion relation for the longitudinal modal wavenumbers χ_i is given as,

$$\chi_i = \sqrt{k^2 - k_{ti}^2} \quad (3-25)$$

for both E and H modes.

Application of the orthonormality properties of the mode functions (3-23) in equation (3-18) results in an equation for the unknown voltage amplitudes given as,

$$V_i(y) = \int_{C_s} M_x(x, y, z) h_{xi}^*(x, y) dC_s \quad (3-26)$$

The particular forms of mode functions, (3-20) and (3-21), used with \underline{M} given in (3-17), yields,

$$V_n'(y) = -E_0 \sqrt{\frac{2}{\pi h}} \frac{(2n+1)\pi}{h} \frac{\pi}{k_{tn}} P_n(y) ; \frac{\text{Volts}}{\text{unit length in } x} \quad (3-27)$$

for E-modes and

$$V_m(y) = j E_0 \sqrt{\frac{2}{\pi h}} \frac{k_x}{k_{tm}} 2\pi P(y)$$

$$\frac{\text{Volts}}{\text{unit length in } x} \quad (3-28)$$

for H-modes.

The voltages of (3-27) and (3-28) are series distributed sources [2] in each of the E_n and H_m -mode transmission lines. Figure 3-3 is the equivalent circuit for the bank of transmission lines and the connected voltage sources.

The transmission line currents (modal current amplitudes I) resulting from the voltage sources are defined via,

$$I(y) = - \int d\xi Y(y, \xi) V(\xi) \quad (3-29)$$

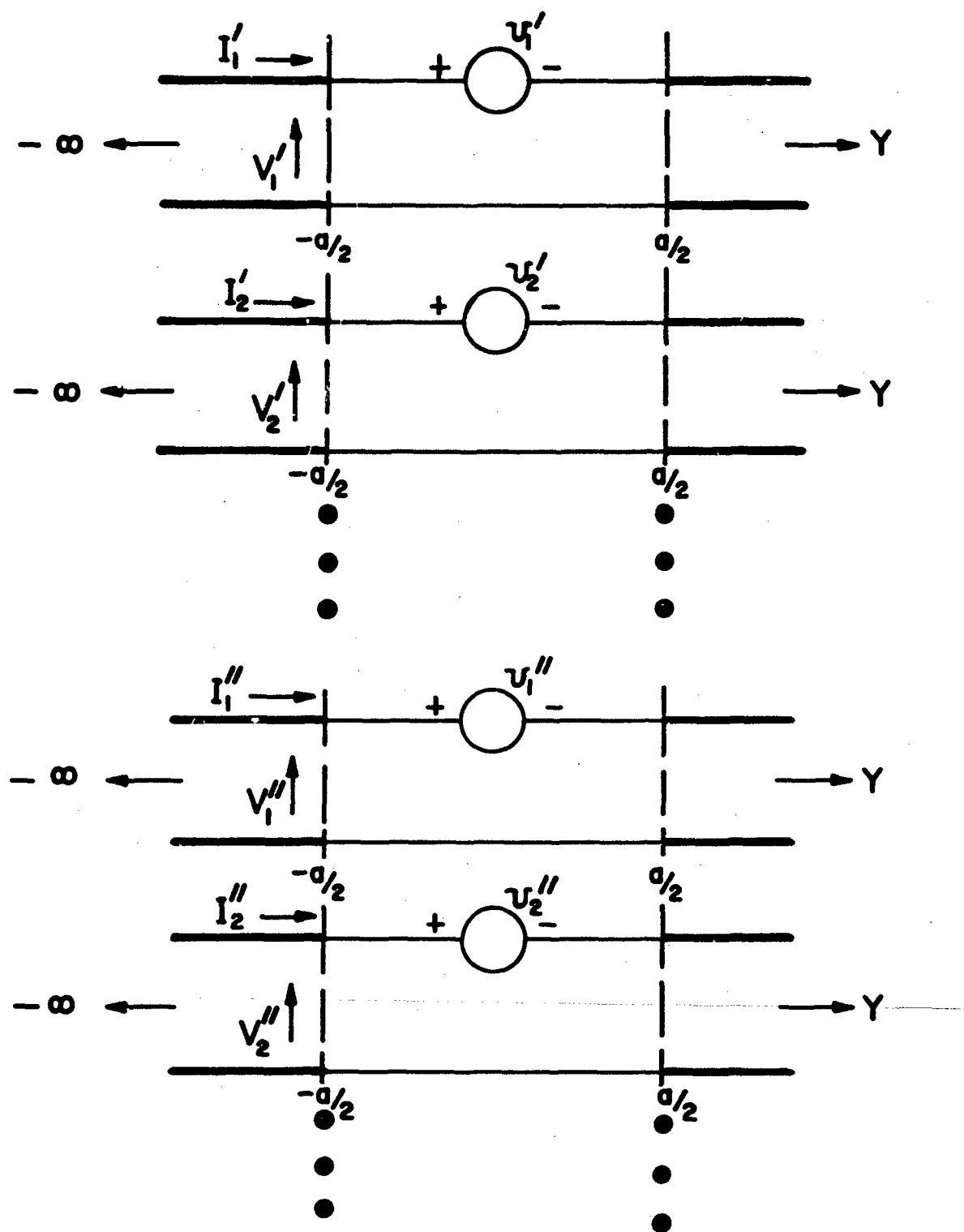


Figure 3-3 Circuit of Transmission Line Bank
Excited by Equivalent Aperture Voltage Sources

where $y(y, \xi)$ is the admittance Green's function for a unit voltage source at a point ξ on a uniform transmission line. For infinite lines this Green's function is,

$$y(y, \xi) = \frac{1}{2Z} e^{-j\alpha|y-\xi|} \quad (3-30),$$

with Z defined as the transmission line characteristic impedance. Using (3-27), (3-28) and (3-30) in (3-29) and performing the indicated integrations yields the modal currents* within the aperture region, given as

$$I_n(y) = \frac{-V}{jZ\alpha} (1 - e^{-j\alpha y/2} \cos \alpha y) \quad (3-31)$$

all n and m ,

with

$$V = V_n' \text{ or } V_m''$$

$$Z = \begin{cases} Z_n' = \frac{\chi_n}{\omega\epsilon} \\ \text{or} \\ Z_m'' = \frac{\omega\mu}{\chi_m} \end{cases}$$

The x directed magnetic field in the aperture region ($z = 0^-$) is,

$$H_x(x, y, 0) = \sum I_n(y) h_{x_i}(x, 0), \quad (3-32)$$

all E and H modes

*It is noted that these modal currents are related as usual to the modal voltages by the transmission line equation

$$V(y) = \frac{j}{\alpha} Z \frac{d}{dy} I(y)$$

The complex power flow in the z direction at $z = 0^-$ is defined in (3-2) as

$$P_z = \int_S \mathbf{E}_y(0^-) \mathbf{y}_0 \times \mathbf{H}_x(0^-) \cdot \mathbf{z}_0 dS \quad (3-33)$$

In terms of the E and H-modes of the parallel plate region, complex power is

$$P_z = - \int_S \mathbf{E}_y(0^-) \left[\sum_n \mathbf{H}_{x_n}'(0^-) + \sum_m \mathbf{H}_{x_m}''(0^-) \right] dS \quad (3-34)$$

The derived values of v and I used in (3-34) yield*,

$$P_z = -2\pi E_0^2 \left[\sum_n K_n' S_n + \sum_m K_m'' S_m \right] \quad (3-35)$$

where
$$S_i = a \left(1 - e^{-j \kappa_i a/2} \frac{\sin \kappa_i a/2}{\kappa_i a/2} \right)$$

$$K_n' = -j E_0 \frac{4}{h} \left[\frac{(2n+1)\pi}{h} \right]^2 \frac{1}{k_{zn}^2} \frac{\omega \epsilon}{\kappa_n^2}$$

and

$$K_m'' = -j E_0 \frac{4}{h} \frac{k_{zm}^2}{k_{zm}^2} \frac{1}{\omega \mu}$$

Both the sums in (3-35) are of order $O(\frac{1}{n^2})$; $O(\frac{1}{m^2})$ which are rapidly convergent.

*See comments following equation 3-13.

3.3 Dispersion Relation

The dispersion relation for the guided wave solutions to the slitted waveguide is obtained by equating (3-35) with (3-13),

$$P_+ = P_- \quad (3-36)$$

or

$$P_+(k, k_x, a) - P_-(k, k_x, a, h, \epsilon) = 0 \quad (3-37)$$

Equation (3-37) is used to compute the x directed wavenumbers k_x . The particular solutions are formed by iterative numerical methods to obtain the zero crossings of the function. The normalized infinite set of solutions k_x/k are given as γ_i . This notation for the x directed normalized eigenvalues as γ_i is used throughout the text.

The solutions for γ in (3-37) are in general complex and correspond to improper leaky waves that attenuate in x and tend to grow in z. The lowest order (least attenuation) solutions reside very close to the positive real γ axis such that their behavior is that of bound surface waves propagating in x. A plot of the real part of γ versus slit width a/λ for the lowest order mode γ_1 is shown in Fig. 3-4 with h/λ as a parameter and dielectric loading $\epsilon = 2.2$ (duroid). The imaginary part of γ_1 is ≈ 0 for the wide range of values shown. The wavenumber lies

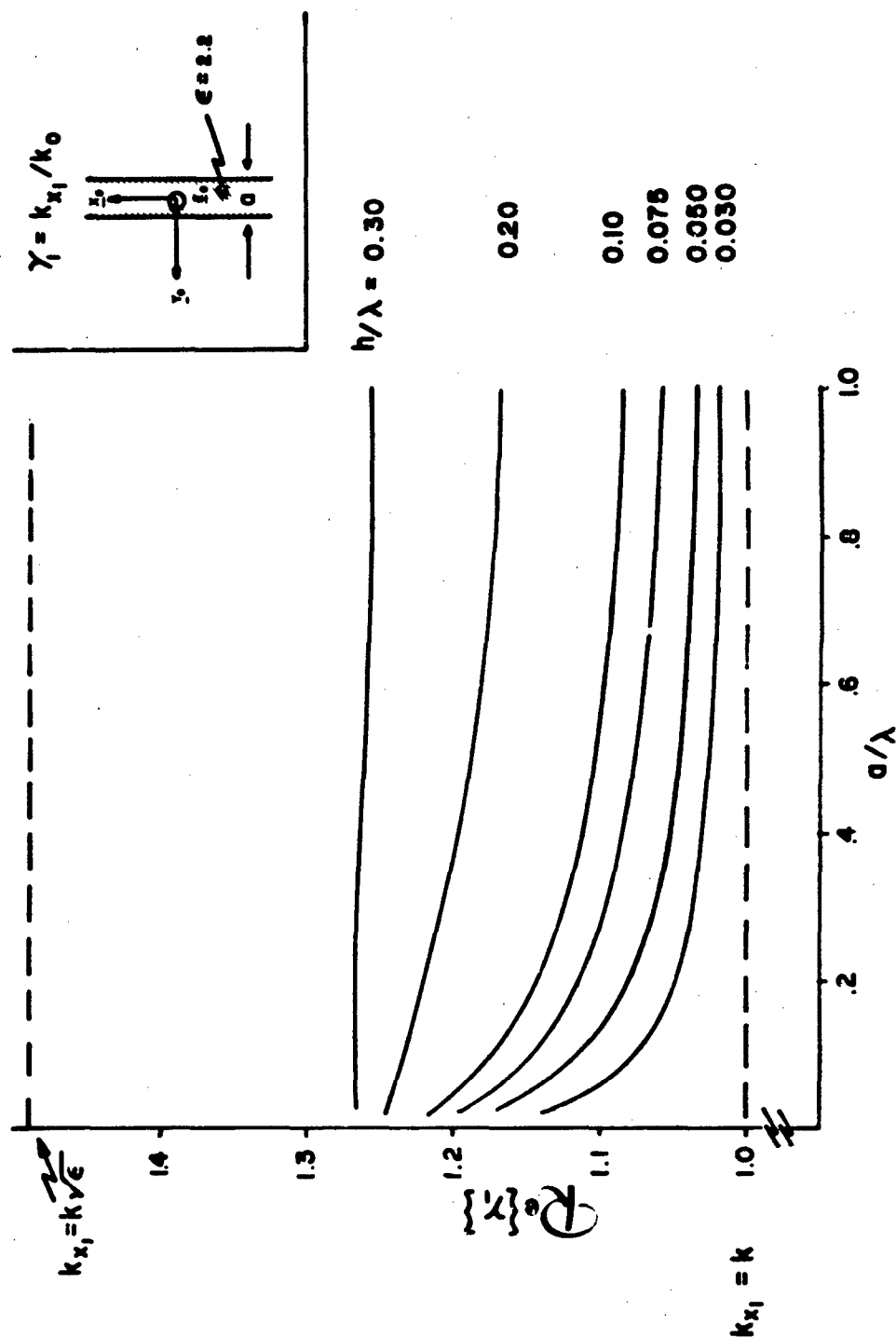


Figure 3-4 $\text{Re}\{\gamma\}$ vs a/λ -Parameter h/λ

between that of TEM propagation in air and that in the dielectric. This is anticipated as these solutions are perturbations about modes of the parallel plate geometry. The wavenumber γ_1 varies slowly with a/λ for a fixed h/λ . This slow variation is necessary in light of the step-wise approximation to the flare.

The curves of Fig. 3-5 are computed values of γ vs a/λ for a fixed geometry a/h . These curves show that for a large range of frequency variation the surface wavenumber γ_1 does not significantly change. For wide slits compared to the stripline plate spacing these variations are extremely slow with frequency. The range of interest in a/h is ≈ 1 and the variations with frequency are still not significant*.

The higher order leaky modes are increasingly evenescent in x . The lowest complex wave, γ_2 is plotted versus a/λ in Fig. 3-6 and Fig. 3-7 corresponding to real and imaginary parts respectively. The parameter h/λ is varied for both curves. The curves remain relatively flat with frequency except for very small slits. The large imaginary part of γ_2 indicates strong attenuation in x and hence, a small contribution to the radiating field. Decreasing attenuation with increased plate width is observed, as might be expected from a bounded structure. There is a corresponding decrease in the real value as cutoff is approached.

*The range of interest is established by the empirically designed notch elements, where $a/h \approx 1$.

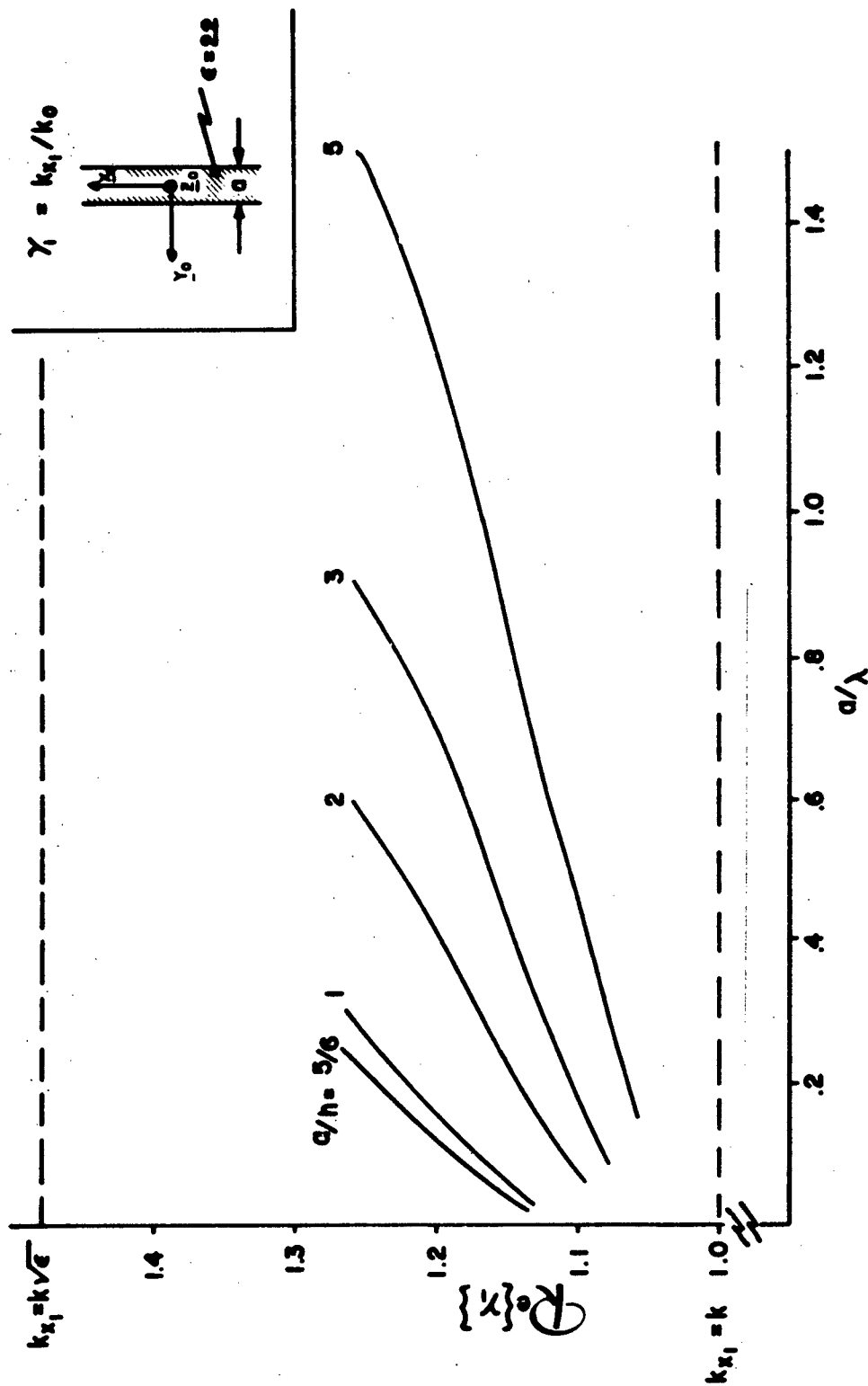


Figure 3-5 $\text{Re}\{\gamma\}$ vs a/λ -Parameter a/h

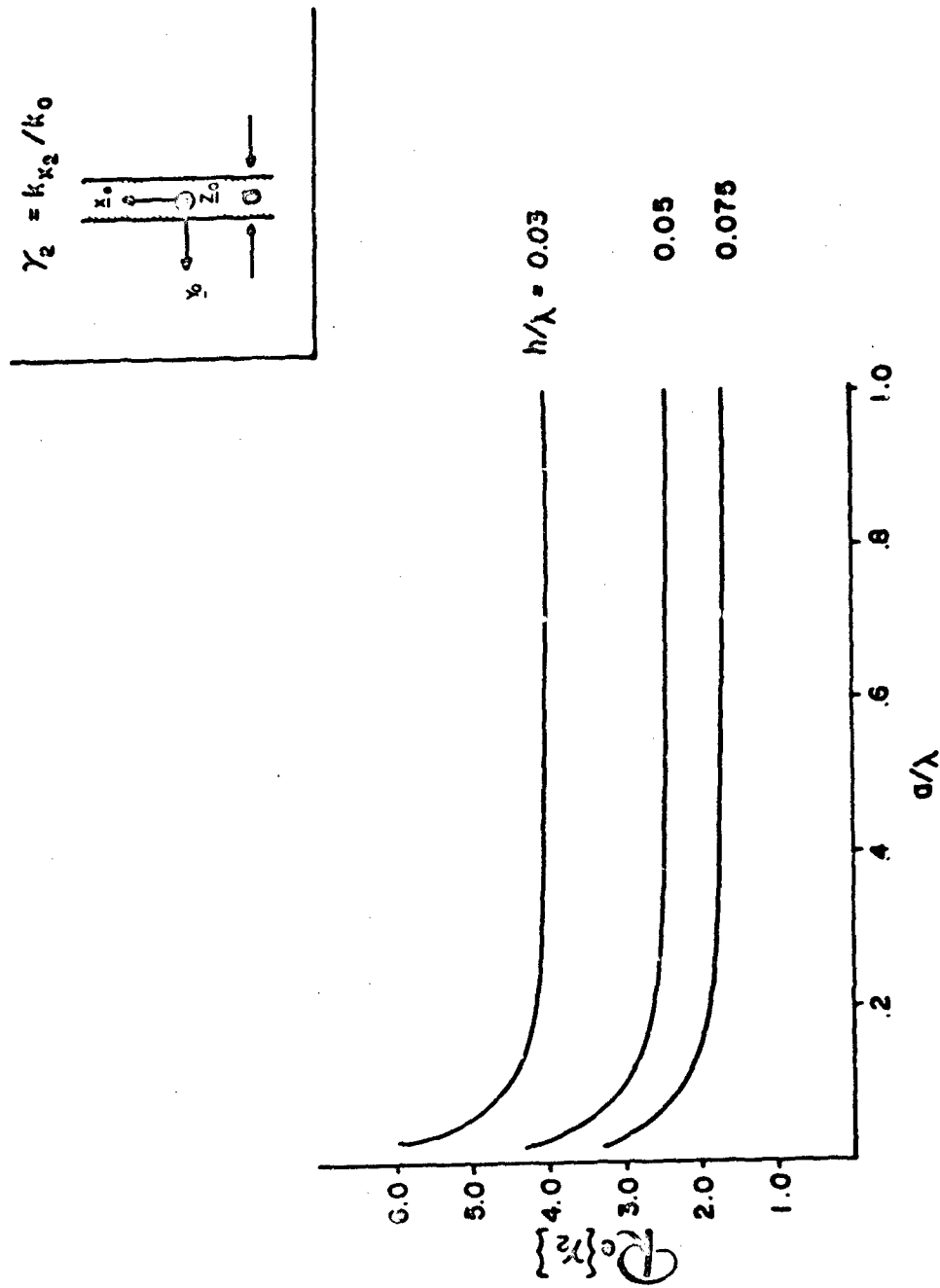


Figure 3-6 Real Part of Higher Leaky Mode of Slitted Parallel Plate Region
-Parameter h/λ

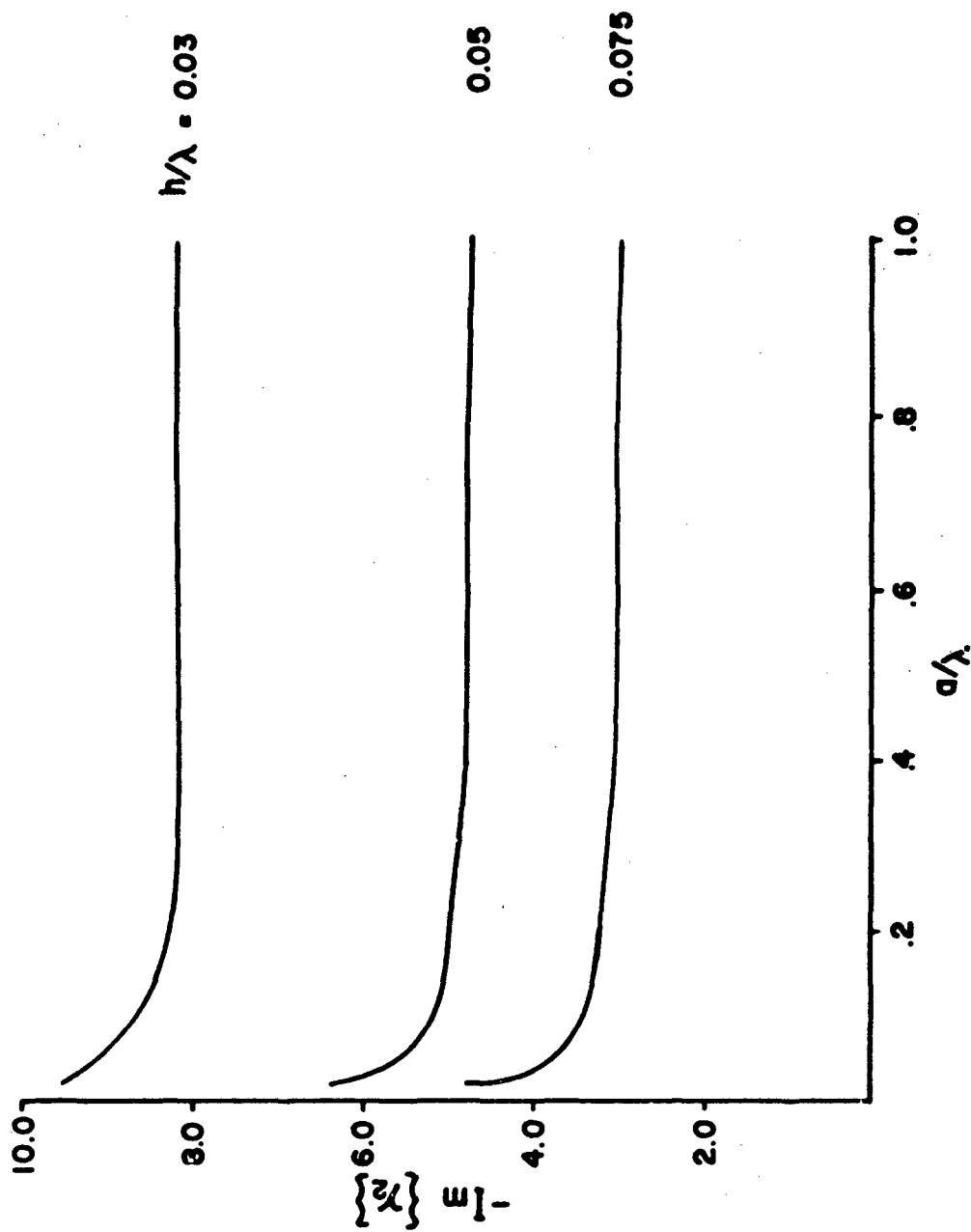


Figure 3-7 Imaginary Part of Higher Leaky Mode of Slitted Parallel Plate Region
-Parameter h/λ

4. PROPAGATION CHARACTERISTICS OF A PERIODIC ARRAY OF SLITTED PARALLEL PLATE GUIDES

The periodic array of slitted (constant width) parallel plate guides finds application as the canonic modal solutions for the tapered notch element array. The slitted parallel plate guide array is shown in Fig. 4-1. This array is assumed linearly polarized (in y) with modes H-type with respect to x ($E_x=0$). In addition the field is approximated with no y variation.*

The infinite array approximation allows the solutions for consideration be reduced to those of a unit cell.^[10] The unit cell wave guide for this infinite slitted parallel plate guide array is shown in Fig. 4-2. The distance between the short circuit walls is D_y (spacer plates for the array case) and the periodicity in z is d . The slit width is a and parallel plate spacing is h , as in the isolated slit guide case. The dielectric loading between plates is .

4.1 Modes

The dispersion relation is an equation, $D(\gamma, k) = 0$, for an arbitrary choice of parameters, D_y , a , h , ϵ , d and phase excitation $\hat{\kappa}$. The solutions γ_i are the longitudinal wavenumbers (in x) that characterize a mode propagating along the unit cell with a unique phase velocity. Symmetry of the structure may be exploited in deriving the dispersion relation which is given by,

$$\cos \hat{\kappa} d = \frac{Y_{sb} + Y_{ob}}{Y_{sb} - Y_{ob}} \quad (4-1)$$

where the subscripts ob and sb correspond to the admittance seen looking into the unit cell circuit at the accessible terminals (see Fig. 4-3) for open and short circuit bisections

* The approximation of no y variation of the field does not result from a fundamental limit of the method of solution but merely a simplification to expedite numerical results.

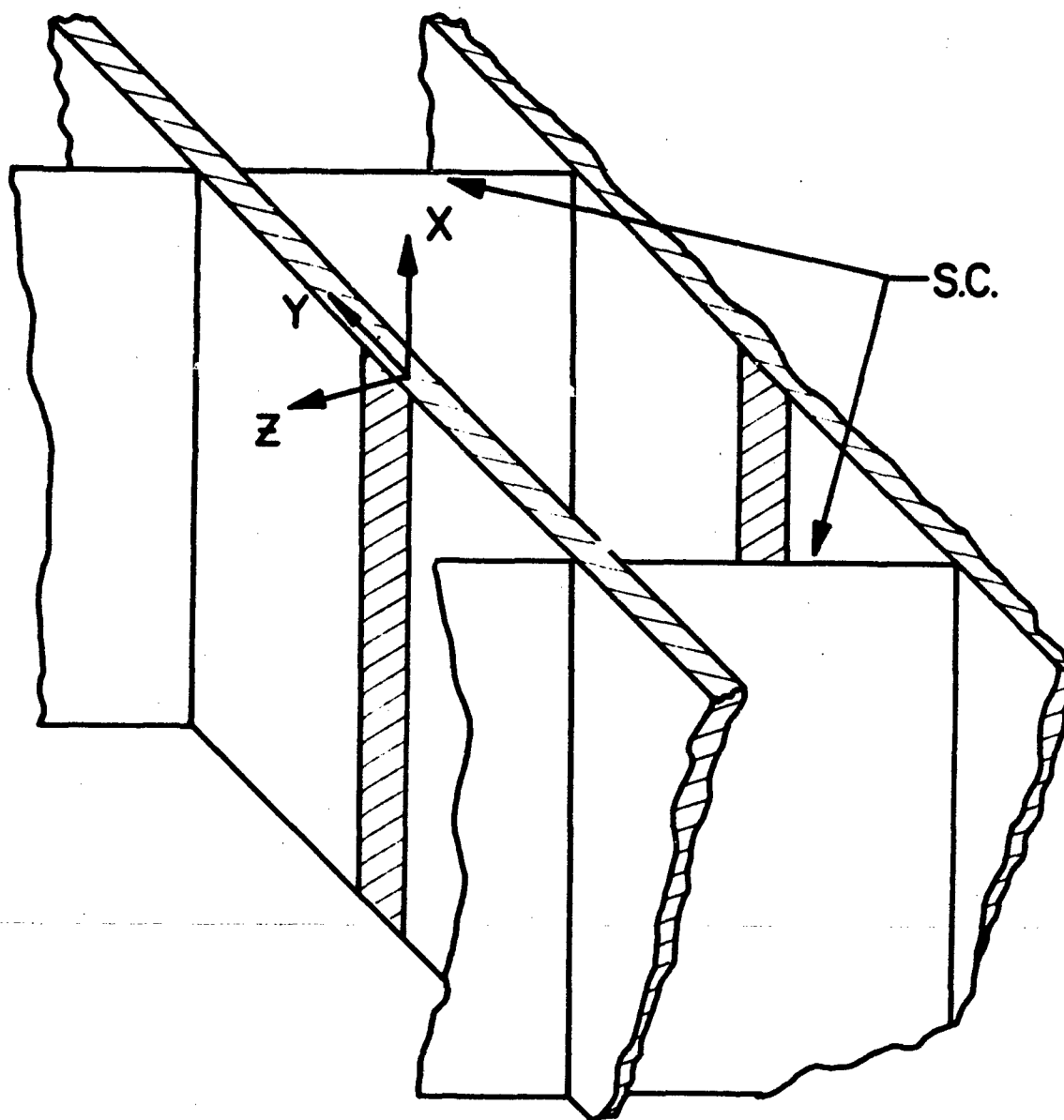


Figure 4-1 Infinite Array of Periodic Slits

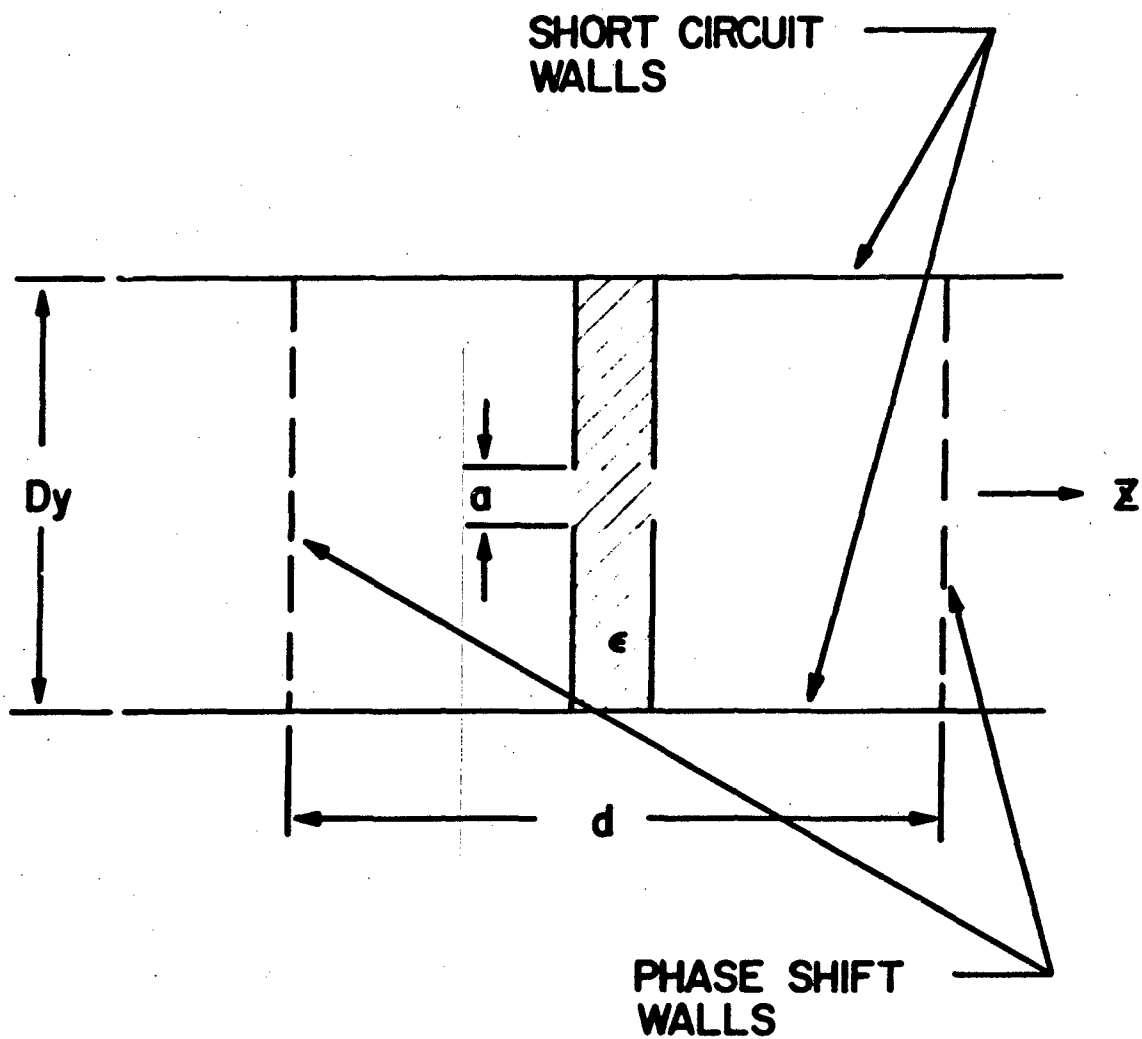


Figure 4-2 Unit Cell of Infinite Array of Slitted Parallel Plate Guides

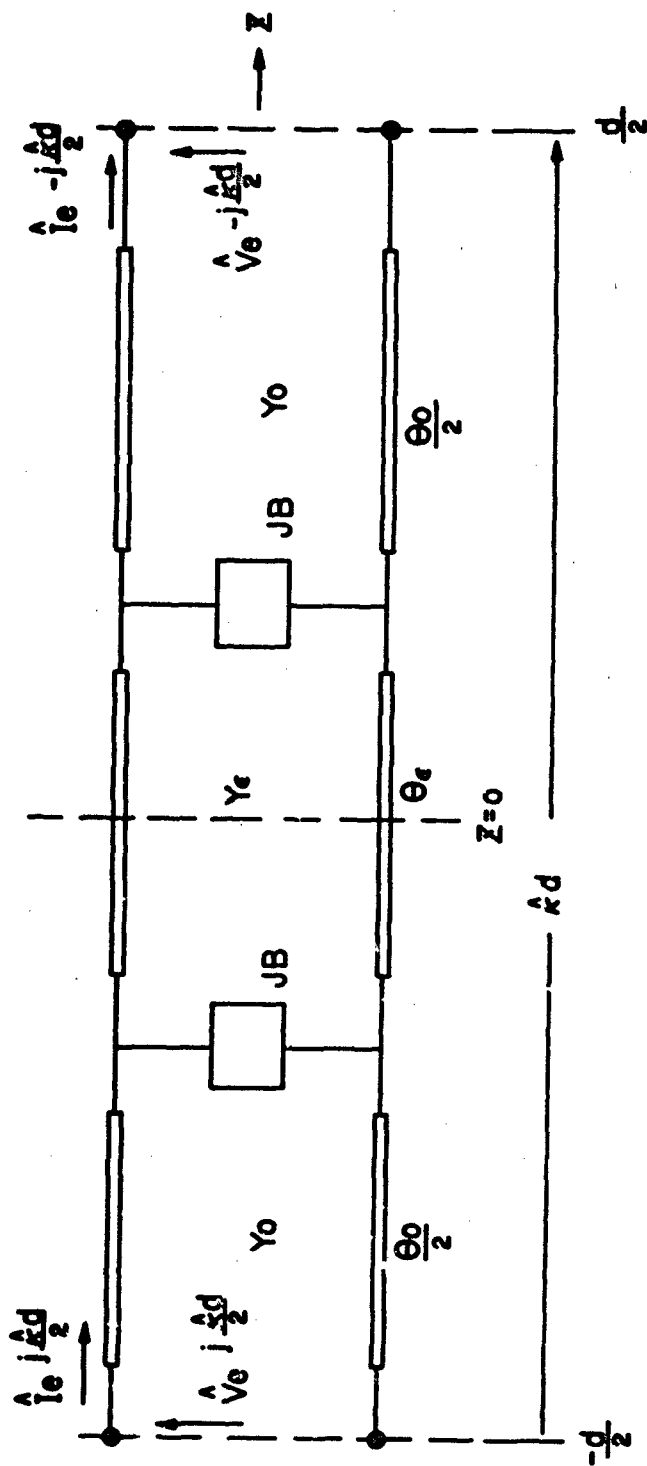


Figure 4-3 Equivalent Circuit of Unit Cell
 kd = Phase Delay Per Period in Z

at the mid-plane. The normalized (to Y_0) admittances are,

$$\bar{Y}_{sb} = \frac{Y_{sb}}{Y_0} = j \frac{B - \bar{Y}_e \cot \theta_s/2 + \tan \theta_e/2}{1 - \bar{B} \tan \theta_s/2 + \bar{Y}_e \tan \theta_s/2 \cot \theta_e/2} \quad (4-2)$$

and

$$Y_{ob} = j \frac{\bar{B} + \bar{Y}_e \tan \theta_s/2 + \tan \theta_e/2}{1 - \bar{B} \tan \theta_s/2 - \bar{Y}_e \tan \theta_s/2 \tan \theta_e/2} \quad (4-3)$$

where

$$\bar{Y}_e = Y_e / Y_0 \quad \text{(normalized modal admittance in dielectric region)}$$

$$\bar{B} = B / Y_0 \quad \text{(normalized susceptance of slit)}$$

$$\theta_s = \kappa_0 (d-h)$$

$$\theta_e = \kappa_e h$$

$$\left. \begin{aligned} \kappa_0 &= k \sqrt{1-\gamma^2} \\ \kappa_e &= k \sqrt{\epsilon_r - \gamma^2} \end{aligned} \right\}$$

no y
variation

and Y_0 and Y are either k/η_0 or $\pi/\eta_0 k$ with η_0 = free-space impedance 377Ω .

The dispersion relation of (4-1) with (4-2) and (4-3), reduces to known solutions for the limiting cases of $\theta_e \rightarrow 0$ and for $\bar{B} \rightarrow 0$. These dispersion relations are:

$$\theta_e \rightarrow 0; \quad \cos \hat{k}d = \cos \theta_e - \bar{B} \sin \theta_e \quad (4-4) \quad [11]$$

and

$$\bar{B} \rightarrow 0; \quad \cos \hat{k}d = \cos \theta_e \cos \theta_e - \frac{\bar{Y}_e + \bar{Z}_e}{2} \sin \theta_e \sin \theta_e \quad (4-5) \quad [12]$$

The susceptance of the slit with $k_x \neq 0$ is obtained by extending known results of susceptance for TEM slit excitation [11] to the H-type mode case via the transformation $k^2 \rightarrow k^2 - k_x^2$. Thus,

$$\bar{B} = \frac{2\bar{D}_y}{\pi} \sqrt{k^2 - k_x^2} \left[\ln \csc \frac{\pi a}{2\bar{D}_y} + \frac{(\frac{2\pi}{\bar{D}_y} \Gamma_1 - 1) \alpha_1^2}{1 + (\frac{2\pi}{\bar{D}_y} \Gamma_1 - 1) \alpha_2^2} \right] \quad (4-6)$$

$$\text{with } \Gamma_1^2 = \left(\frac{\pi}{\bar{D}_y}\right)^2 + k_x^2 - k^2$$

$$\text{and } \alpha_1 = \cos^2 \frac{\pi a}{2\bar{D}_y}; \quad \alpha_2 = \sin^2 \frac{\pi a}{2\bar{D}_y}$$

Figs. (4-4) - (4-6) are curves of γ_0 versus $\hat{k}d/\pi$ (phasing) for three notch configurations in a square array, with frequency as a parameter. Each figure is associated with a fixed geometry, specifying a/d and a/h , and presents the family of curves for a/λ . The selection of parameters is based on assuming the stripline plate spacing, h , remains constant, and the a/h ratios vary from curve to curve in a manner typical of the range of notch flare. In similar fashion the choices of a/d are made. The relative dielectric constant is assumed to be $\epsilon_r = 2.22$ for duroid.

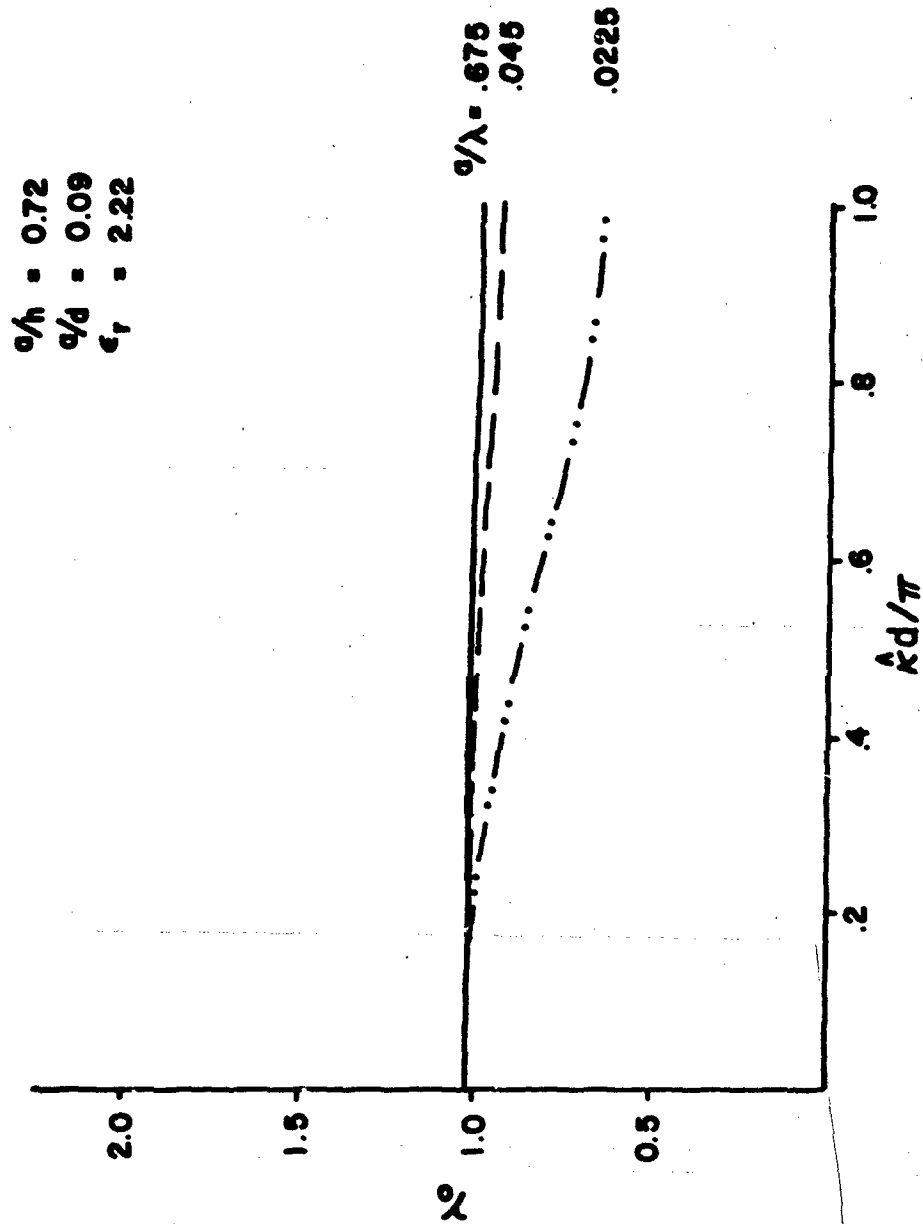


Figure 4-4 γ_0 vs kd/π -Parameter a/λ

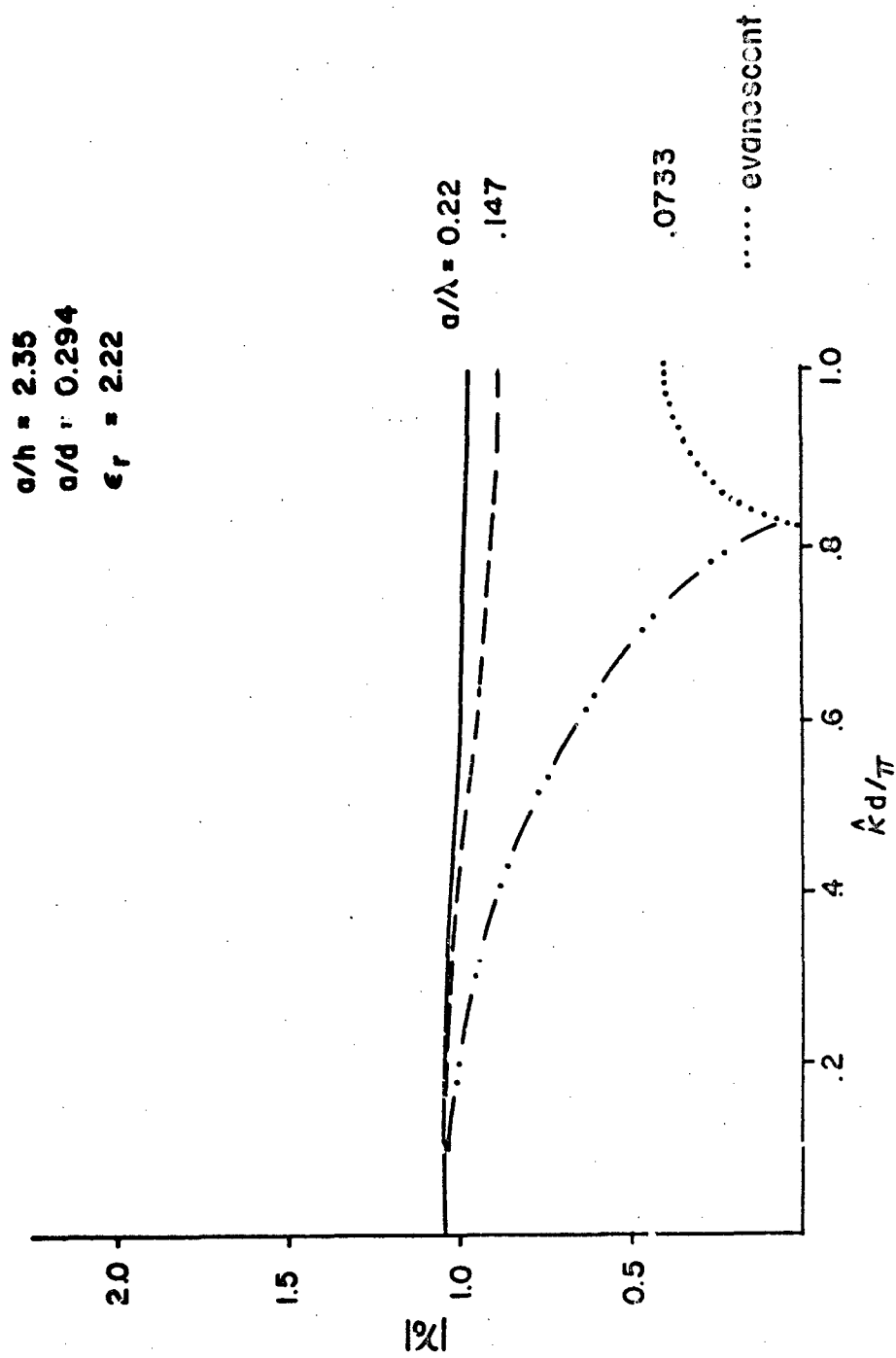


Figure 4-5 γ_0 vs $\underline{kd/\pi}$ -Parameter a/λ

$a/h = 5.09$
 $a/d = .638$
 $\epsilon_r = 2.22$

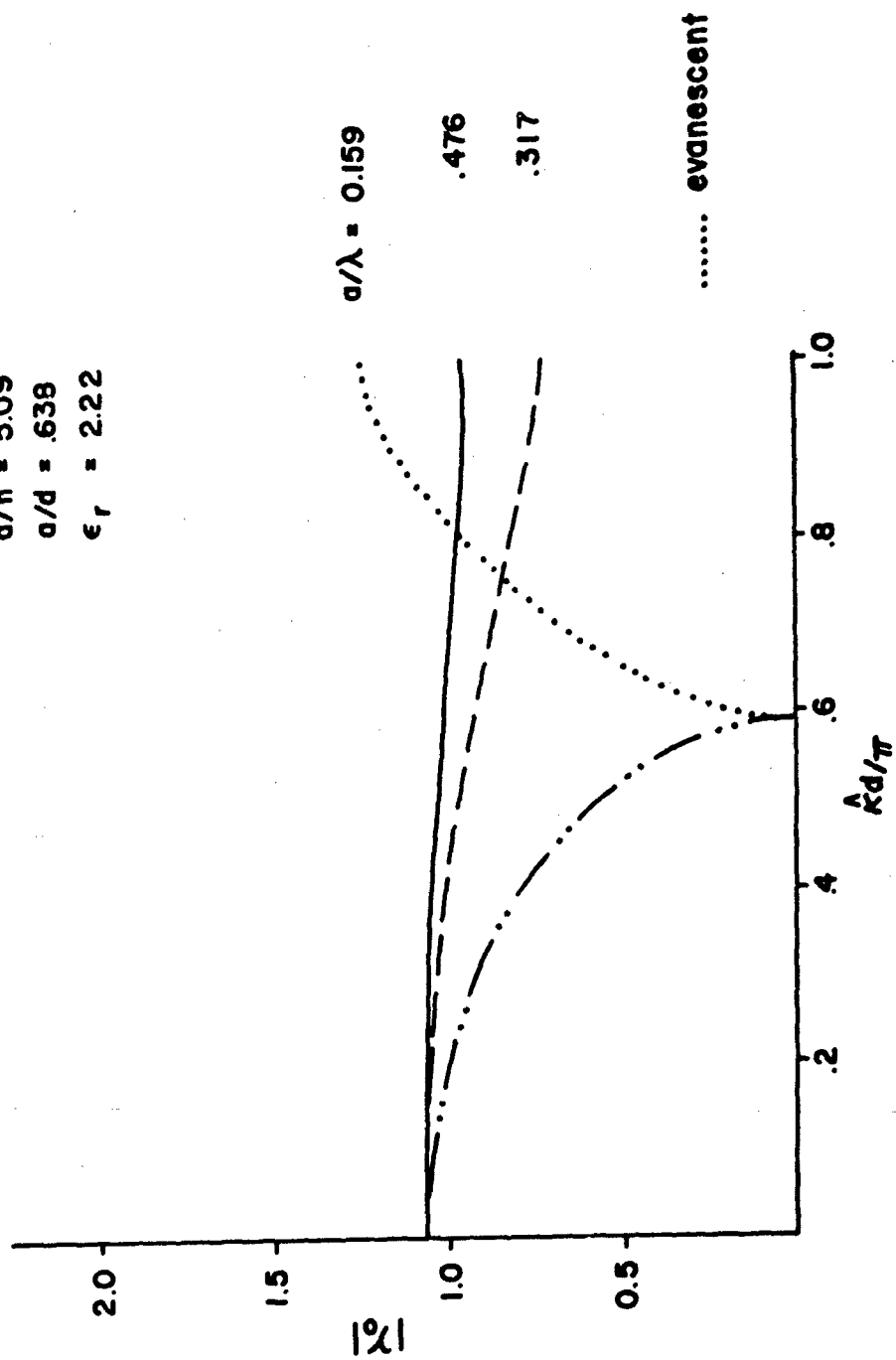


Figure 4-6 γ_0 vs $\hat{k}d/\pi$ -Parameter a/λ

In general, the γ_0 mode is a slow wave ($\gamma_0 > k$) for $\hat{k}d/\pi = 0$. As $\hat{k}d/\pi$ is increased, the mode eventually passes through $\gamma_0 = k$. Further increase in $\hat{k}d/\pi$ drives the mode toward cut-off. At the high frequency, γ_0 varies only slightly out to the band edge, with only nominal change in a/λ ratio. At the middle and low frequencies, γ_0 tends toward cut-off as the $\hat{k}d/\pi = 0$ band edge is approached. In particular, at the low frequency, γ_0 is cut off beyond $\hat{k}d/\pi \sim .82$, for $a/h = 2.35$, and beyond $\hat{k}d/\pi \sim .52$, for $a/h = 5.09$.

Some interesting trends of the dispersion relation may be seen from a consideration of Fig. (4-7). This curve fixes h/λ and spacing d/λ for a square grid array and vary a/λ . For scanning, $\hat{k}d/\pi > 0$, the γ_0 mode goes from a slow to a fast wave ($\gamma_0 < k$) eventually being cut-off and then increasingly evenescent. This cut-off behavior is typical for array scanning, and the slow-to-fast wave characteristic has been shown for the limiting case of a periodic array of dielectric slabs.^[12]

Fig. (4-7) shows that for increasing slit width the cut-off condition moves closer to broadside scan. A close look at the dispersion relation for periodically iris-loaded waveguide verifies this trend. The dispersion relation for the waveguide is given in equation (4-4) as $\cos \hat{\theta} = \cos \hat{\theta} - \bar{B} \sin \hat{\theta}$, with $\hat{\theta} = \hat{k}d$. A plot of (4-4) for \bar{B} versus θ is shown in Fig. (4-8) for the lowest order passband where θ is taken as a parameter. Band edges are at $\hat{\theta} = 0$ and π , with corresponding band edge curves given as $\bar{B}(\theta; 0) = -\tan \theta/2$ and $\bar{B}(\theta; \pi) = -\cot \theta/2$. The passband region is shown shaded in the figure.

The actual behavior of susceptance versus θ is given by equation (4-6) and may be plotted onto Fig. 4-8 to graphically display the cut-off trends of interest. The iris susceptance equation of (4-6) shows that \bar{B} is linear in θ , ($\theta \ll \sqrt{k^2 - k_x^2}$). In particular for the range $0 \ll a/D_y \ll 1$ the corresponding slope of $\bar{B}(\theta)$ varies between zero and infinity. Figure 4-9 is the

$\epsilon_r = 2.20$
 $d_x/\lambda = d_y/\lambda = 0.2545$
 $h/\lambda = 0.0424$

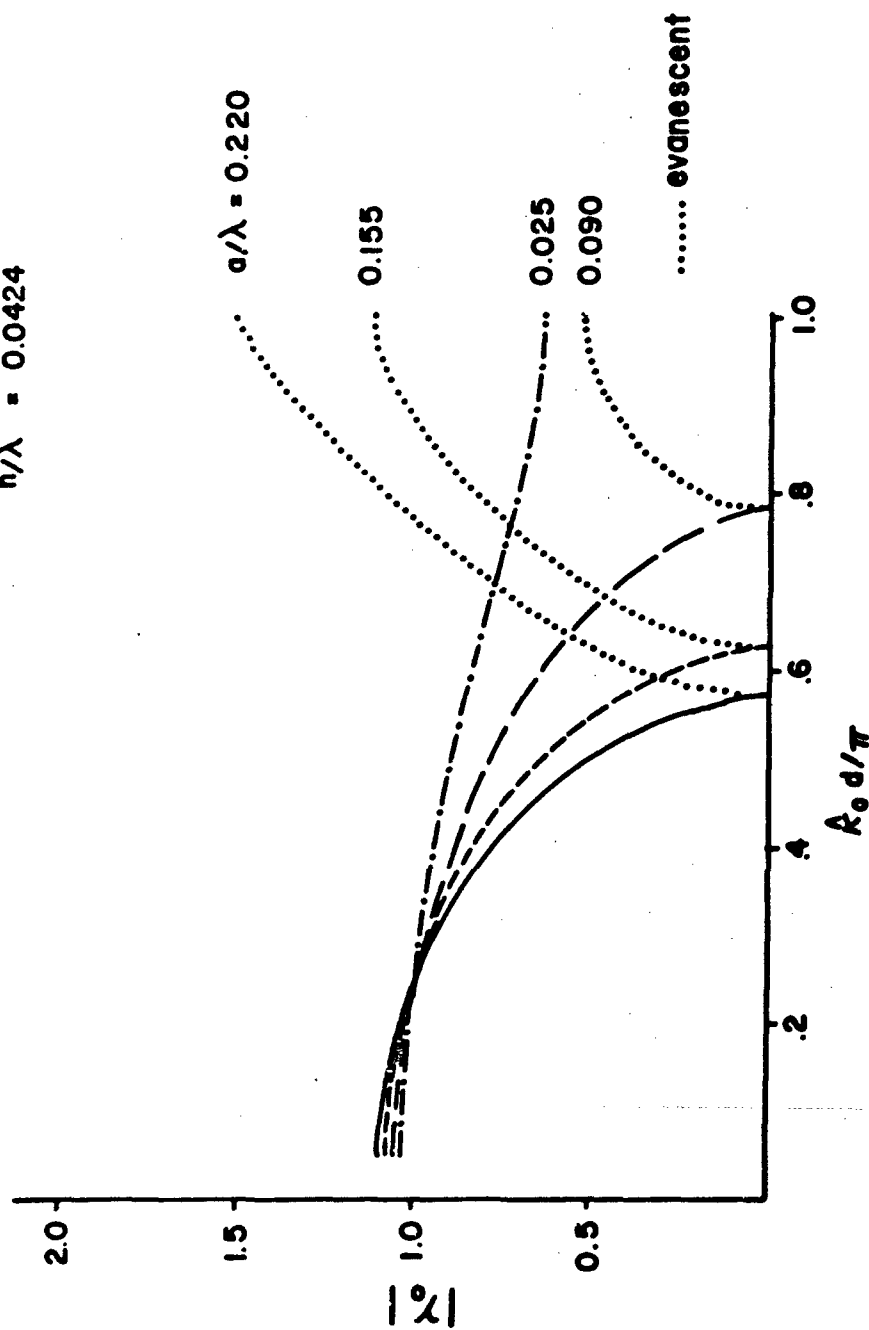


Figure 4-7 γ_0 vs $k_0 d/\pi$ -Parameter a/λ

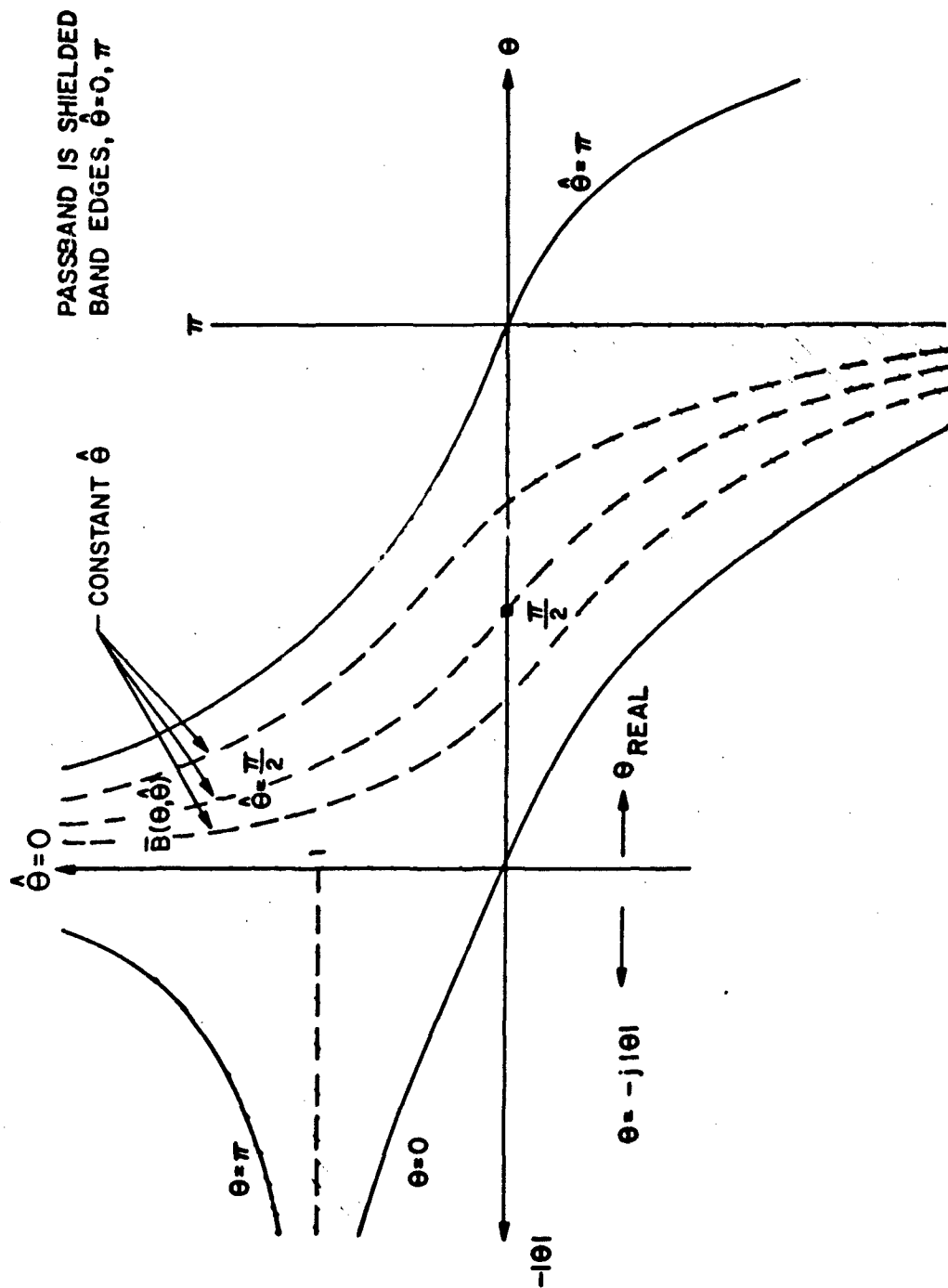


Figure 4-8 Lowest Order Passband of the
Dispersion Relation for Iris Loaded
Waveguides, $\bar{B}(\theta, \hat{\theta})$ Versus θ .

superposition of "load lines," onto the applicable region of the dispersion curve of Fig. 4-8, ($\bar{B} = C\theta$, with C a parameter proportional to a/D_y). A family of load lines is drawn with decreasing slopes as a/D_y increases.

The cut-off trends of Fig. 4-7 are seen by assuming a cut-off condition for the simplified dispersion curve of Fig. 4-9. A cut-off line ($\gamma = 0$) at $\theta \sim kd$ is drawn. Intersections of this cut-off line with three load lines are labelled 1, 2, and 3. In this same order (1, 2, and 3) the values of a/D_y are increasing. These intersections lie on constant $\hat{\theta}$ curves which are decreasing for this same ordering following the trends shown in Fig. 4-7.

4.2 Mode Functions of the Unit Cell Waveguide

Since the unit cell waveguide is uniform in the x , direction it supports modes with $e^{-jk_x x}$ variation. With no y variation the transverse to x field of a typical mode may be set,

$$\begin{aligned} \underline{E}_t(x, z) &= V e^{-jk_x x} \underline{e}(z) \\ \underline{H}_t(x, z) &= I e^{-jk_x x} \underline{h}(z) \end{aligned} \quad (4-7)$$

for $0 \leq z \leq d$.

The assumed polarization is H-type with respect to x , ($E_x = 0$) such that for no y variation,

$$\underline{e}(z) = e_y(z) \underline{y}_0$$

and

$$\underline{h}(z) = h_z(z) \underline{z}_0$$

The field is thus TEM at an angle to the x axis; modes are H with respect to x where it has been shown that [12]

$$e_y(z) = h_z(z) = - \frac{\hat{V}(z)}{N} \quad (4-8)$$

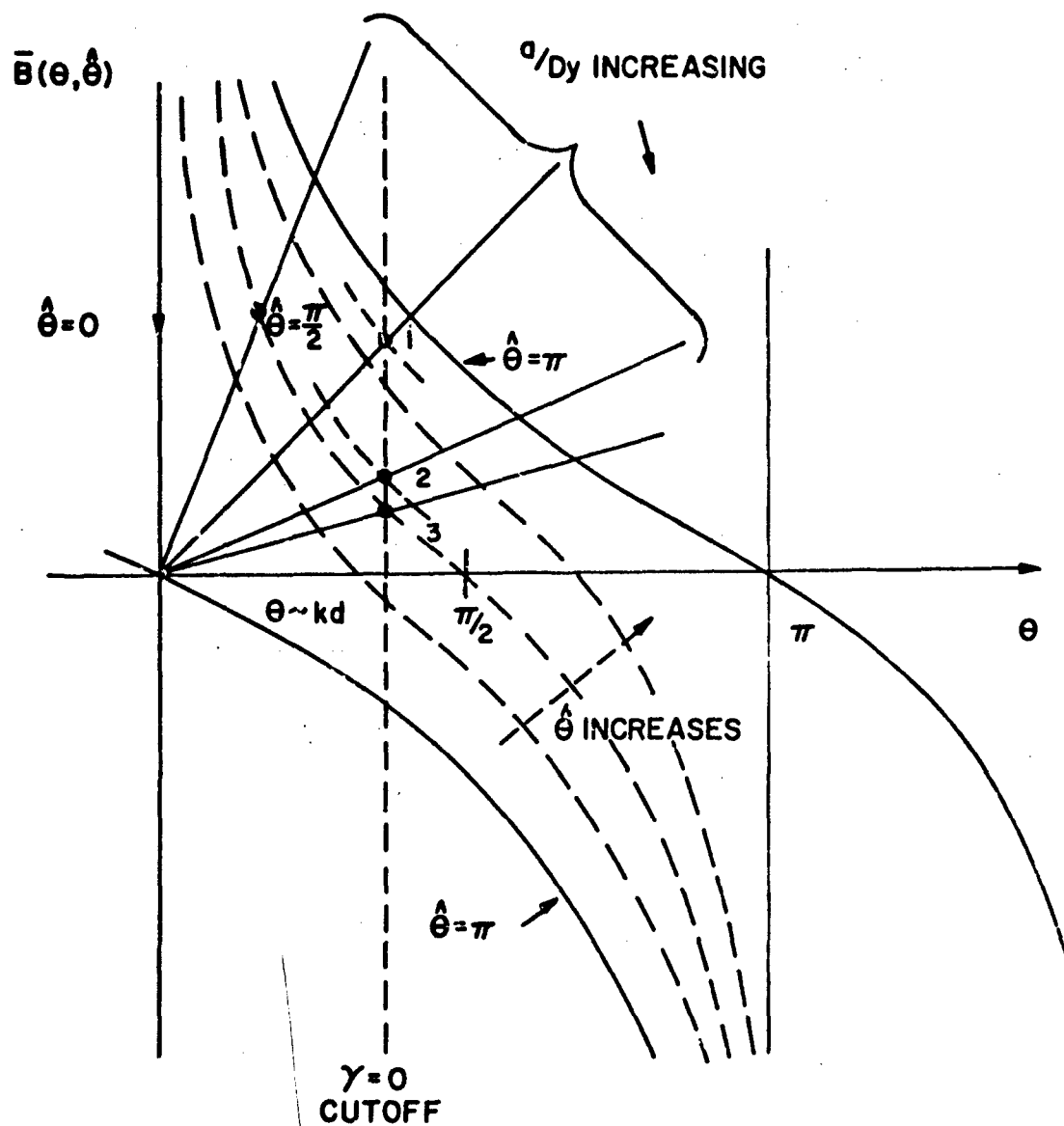


Figure 4-9 Susceptance Load Lines
on Dispersion Curve for
Iris Loaded Waveguides

$\hat{V}(z)$ is computed from the equivalent circuit of the unit cell, Fig. 4-3, with appropriate H-mode network parameters. The quantity N is a normalization given by,

$$N^2 = \int_{-d/2}^{d/2} |\hat{V}(z)|^2 dz \quad (4-9)$$

This normalization was selected such that complex power carried by the N^{th} mode in the x direction is given by $V_n I_n^*$. The H-mode impedance of the x directed transmission line is $\omega\mu/v$.

The voltage variation $\hat{V}(z)$, can be easily found from the open and short circuit bisections of the unit cell circuit. The open circuit bisection results from the real part of the terminal voltages and the short circuit bisection is obtained from the imaginary parts. For symmetric excitation (open circuit),

$$\hat{V}(-z) = \hat{V}(z) \quad (4-10)$$

where

$$\hat{V}(z) = \begin{cases} \hat{V} \cos \frac{\kappa_0 d}{2} [\cos \kappa_0 (z + d/2) - j Z_0 Y_2 \sin \kappa_0 (z + d/2)], & -d/2 \leq z \leq d/2 \\ \hat{V}(-d/2) [\cos \kappa_0 (z + d/2) - j Z_0 Y_1 \sin \kappa_0 (z + d/2)], & -d/2 \leq z \leq 0 \end{cases} \quad (4-11)$$

with

$$Y_1 = Y_0 \frac{j Y_0 + Y_2 \cot \kappa_0 (d-h)/2}{Y_0 \cot \kappa_0 (d-h)/2 + j Y_2}$$

$$Y_2 = j (Y_0 \tan \kappa_0 h/2 + B)$$

$$Y_1 = Y_0 \tan \kappa_0 h/2$$

For antisymmetric excitation (short circuit),

$$\hat{V}(-z) = -\hat{V}(z) \quad (4-12)$$

where

$$\hat{V}(z) = \begin{cases} \hat{V} \sin \frac{\pi d}{2} [\cos \kappa_0(z + \frac{1}{2}) - j \frac{Z_0}{Y_1} \sin \kappa_0(z + \frac{1}{2})], & -\frac{d}{2} \leq z \leq \frac{1}{2} \\ \hat{V}(-\frac{1}{2}) [\cos \kappa_0(z + \frac{1}{2}) - j Z_0 Y_1 \sin \kappa_0(z + \frac{1}{2})], & -\frac{1}{2} \leq z \leq 0 \end{cases}$$

Curves of the $n = 0$ mode functions are shown in Figs. (4-10) and (4-11) with $\frac{\kappa d}{\pi}$ as a parameter. In Fig. 4-10 the slit width is made equal to element spacing and these results limit to those of the periodic array of dielectric slabs. The physical configuration that corresponds to mode function curve of Fig. 4-11 is that of a thin slab with a fairly wide slit and a small periodicity. The field is essentially constant in z for $\frac{\kappa d}{\pi} < 0.8$, and then shows the development of the short circuit at $z = -d/2$ end open circuit at $z = 0$ associated with the $\frac{\kappa d}{\pi} = 1$ band edge.

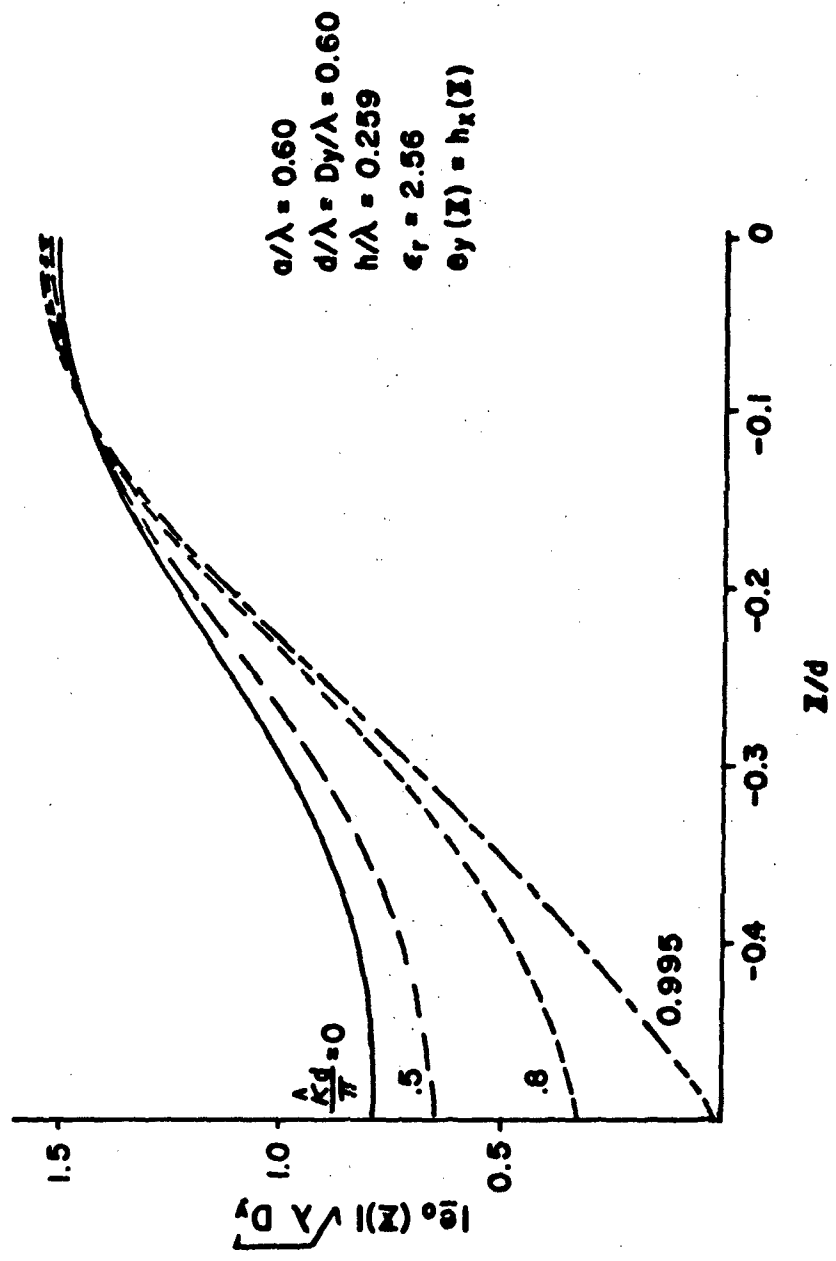


Figure 4-10 n=0 Mode Function (H-Mode)

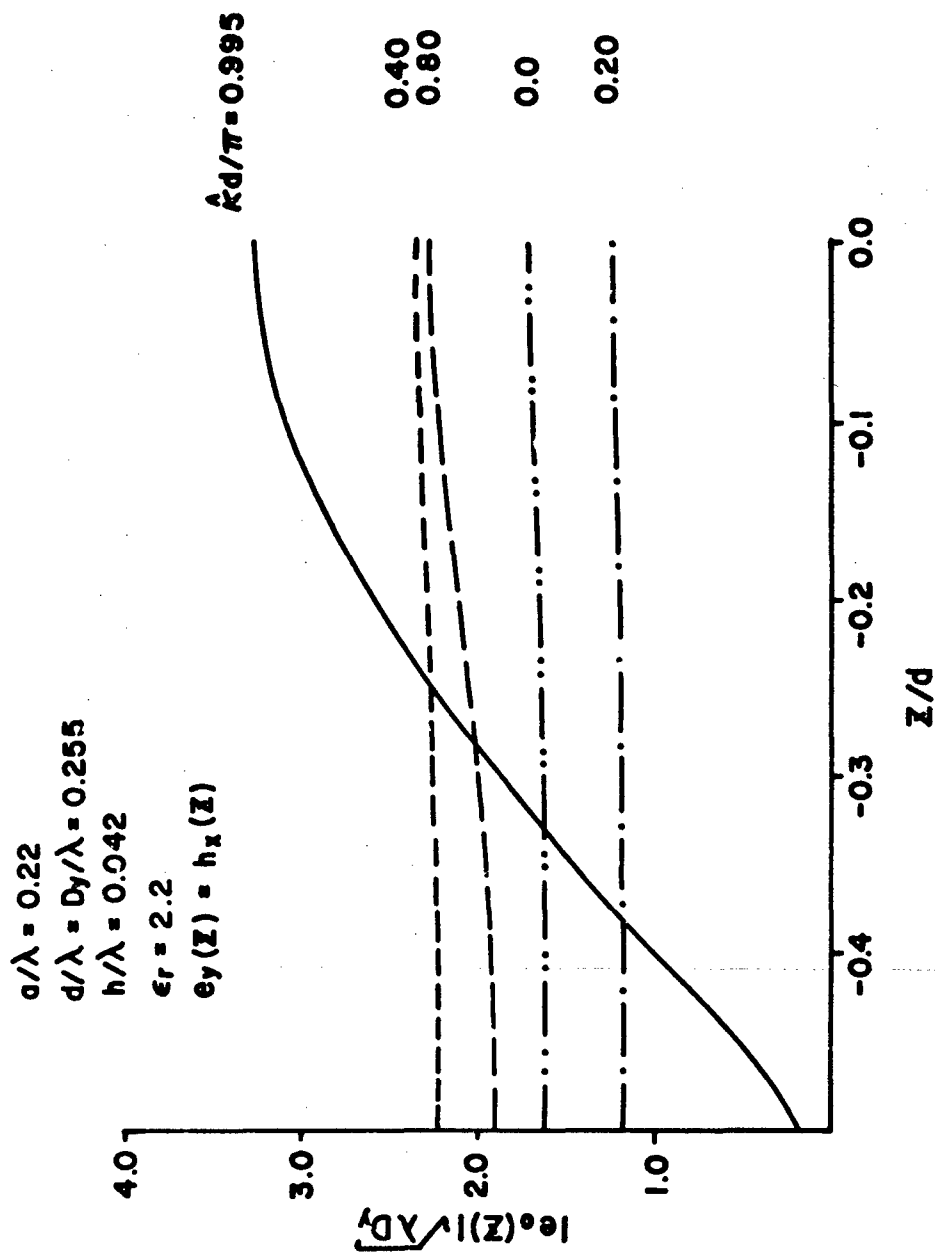


Figure 4-11 $n=0$ Mode Function
(H-Mode)

5. THE INFINITE PHASED ARRAY OF NOTCH ELEMENTS

The notch antenna used as an array element is a lightweight low cost approach for broadbanding. The notch element in a practical array configuration is shown in Fig. 5-1. The E-plane is formed by the plane of the elements, with metallic spacers in the H-plane. A practical feed can fit broadband phase shifters behind each element connected through the rear ground plane: a right angle stripline bend from the notch coupling region toward the ground plane and then a stripline-coax or stripline-waveguide adapter to the phase shifter.

The analysis of a large phase array of this type is facilitated by using the infinite array approximation which permits a consideration of only the unit cell. The array may be characterized by three distinct propagation regions whose modes remain decoupled except at the discontinuities separating these regions. These regions are the stripline feed, the notch parallel plate guide and free space. A scattering matrix for each discontinuity is determined in terms of the modal transmission lines connecting the regions. Calculations of reflection and transmission coefficient result from evaluation of the network of these scattering matrices.

Basic to the analytic solutions for reflection and transmission of the array is the determinations of modes in the notch region. For the tapered notch this region is non-uniform along the propagation direction (in x), but modal solutions for the array of constant width slitted parallel plate guides (Chapter IV) may be extended for the taper by a stepwise approximation.

The array reflection coefficient is determined from a formulation involving the scattering matrices of the interfaces between a) the aperture plane ($x = l$) and free-space, \underline{S}^a b) the stripline feed to notch transition, \underline{S}^o , and c) the transformers representing the stepwise approximation of the flared notch. An equivalent network involving the scattering matrices for junctions a) and b), and the variable impedance

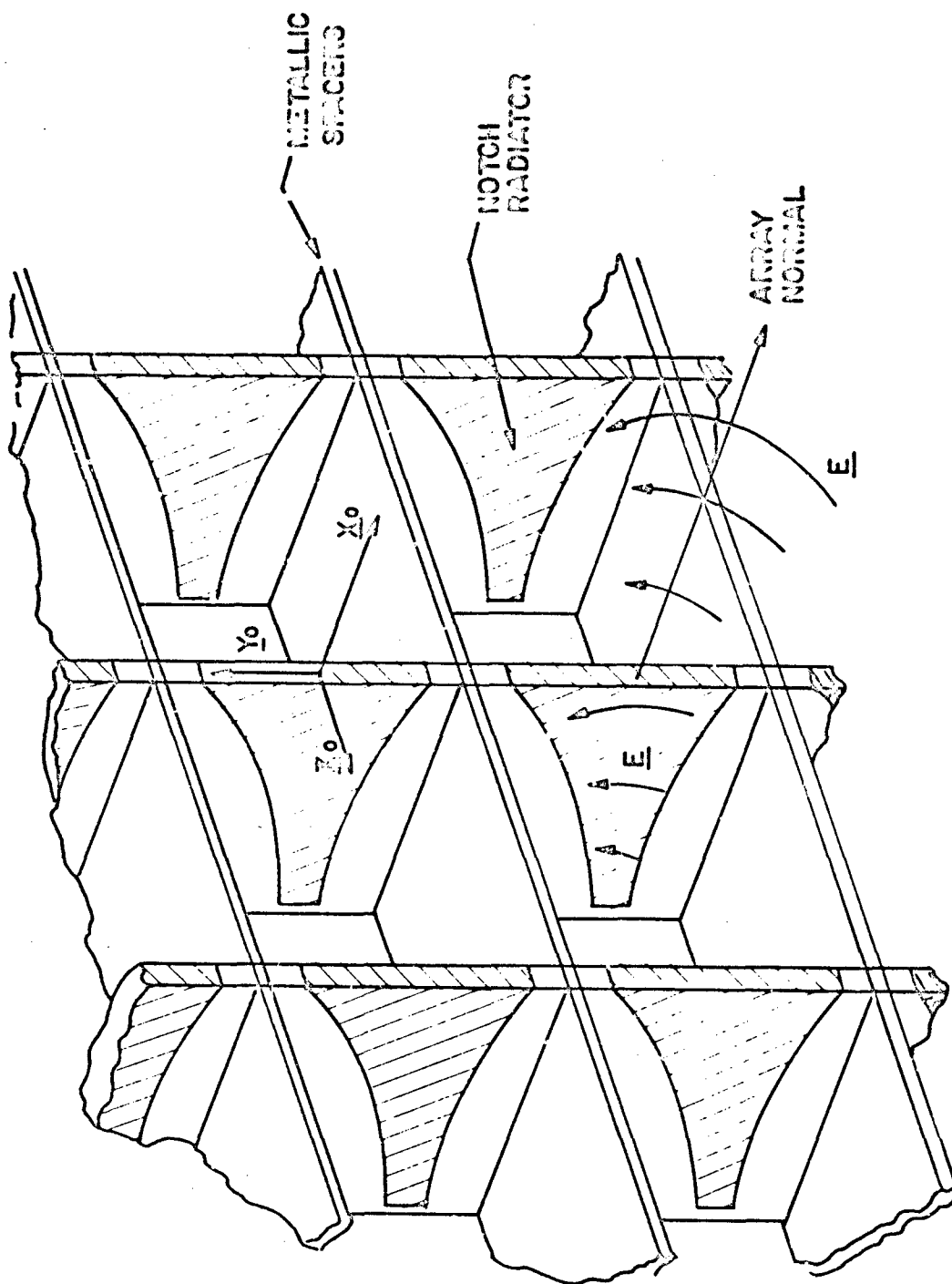


Figure 5-1 Notch Element Array "Egg Crate"

transmission line for the flare region is shown in Fig. 5-2. The network N connecting the junctions a) and b) is composed of equal lengths of non-uniform, uncoupled transmission lines. The particular choice of N is that of small steps of uniform regions to approximate the flare.

The scattering matrix $\underline{\underline{S}}^a$ is obtained by matching transverse fields at the aperture interface, via Galerkin's method. This type of evaluation is standard [13], [14], and has been carried out specifically for a scattering matrix approach to phased array analysis. The scattering matrix $\underline{\underline{S}}^n$ is obtained in a manner similar to the isolated notch, in Chapter II, requiring conservation of energy. A transmission matrix is conveniently used for the cascaded transmission lines of the flare. For each step of this cascaded line the appropriate wavenumbers (modal impedances) are obtained via the dispersion relation of equation (4-1). Both the scattering matrix $\underline{\underline{S}}^o$ and transmission matrix $\underline{\underline{T}}$ are found for single mode representation of stripline and notch regions, the scattering matrix $\underline{\underline{S}}^a$ is multimode.

With the discontinuities characterized by the scattering matrices and knowledge of the network N (Chapter 4) for the connecting flare region, the input reflection coefficient, element patterns, as well as unknown modal voltages, are readily obtained from the network of Fig. 5-2.

5.1 The Scattering Matrix $\underline{\underline{S}}^a$

The determination of the scattering matrix at the free-space interface, $x = l$, is based on approximate field matching via Galerkin's method. The notch region is assumed to extend from $x = l$ to $x = -\infty$ and is of uniform width. With the notation of Fig. 5-2 and with

$$\underline{\underline{V}}_r = \left(\frac{\underline{\underline{V}}_r^{-l}}{\underline{\underline{V}}_a^+} \right) ; \quad \underline{\underline{V}}_i = \left(\frac{\underline{\underline{V}}_i^{-l}}{\underline{\underline{V}}_a^-} \right) \quad (5-1)$$

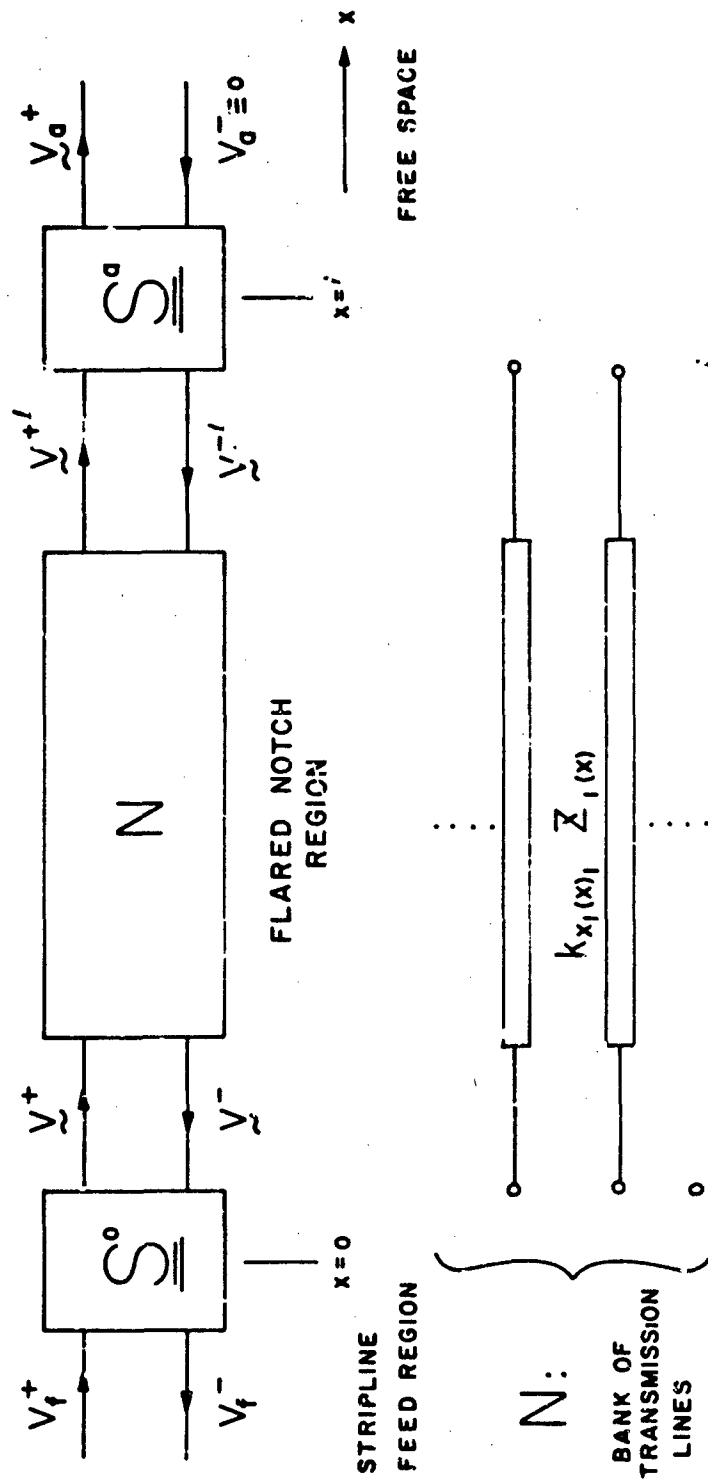


Figure 5-2 Equivalent Circuit of Unit Cell

the matrix $\underline{\underline{S}}^a$ is defined by

$$\underline{\underline{V}}_r = \underline{\underline{S}}^a \underline{\underline{V}}_i \quad (5-2)$$

and may be partitioned as follows:

$$\underline{\underline{S}}^a = \left(\begin{array}{c|c} \underline{\underline{S}}_{11}^a & \underline{\underline{S}}_{12}^a \\ \hline \underline{\underline{S}}_{21}^a & \underline{\underline{S}}_{22}^a \end{array} \right)$$

For the excitation conditions of interest, where $V_a^- = 0$, only $\underline{\underline{S}}_{11}^a$ and $\underline{\underline{S}}_{12}^a$ are of concern. The order of these partitioned blocks is determined by the number of modes used to approximate the fields in the notch and free-space regions. The orthonormal mode functions, \underline{e} , \underline{h} of the notch region have been derived in Chapter 4. The transverse fields in the unit cell at the plane $x = l^-$ (at the discontinuity) are given in terms of the mode functions with corresponding modal voltage and current amplitudes as,

$$\begin{aligned} \underline{E}_t(x=l^-) &= \sum_n V_n^l \underline{e}_n \\ \underline{H}_t(x=l^-) &= \sum_n I_n^l \underline{h}_n \end{aligned} \quad (5-3)$$

where the mode index includes arbitrary intergers for both a y and \bar{y} dependence and the division of E and H modes. The free-space modal representation for the infinite doubly periodic array embedding is given in the Waveguide Handbook.^[17] The orthonormal mode functions are \underline{e}_a and \underline{h}_a .

A simple set of equations relating total modal voltages and currents in the free-space and slitted regions results from application of Galerkin's method for matching the fields at the boundry. These are:

$$\underline{V}_A = \underline{\mathcal{E}}^* \underline{V}^f$$

and *

$$\underline{I}^f = \underline{\tilde{\mathcal{E}}} \underline{I}_A$$

(5-4)

where $\underline{\mathcal{E}}$ is a coupling coefficient matrix or Fourier transforms of the slitted parallel plate guide array fields. The elements of $\underline{\mathcal{E}}$ are

$$\mathcal{E}_{mn} = (\underline{e}_n, \underline{h}_{am} \times \underline{x}_0) \quad (5-5)$$

where the parentheses is an inner product integral over the unit cell. The explicit expressions for \mathcal{E}_{mn} are given in Appendix D.

The scattering block \underline{S}_{11}^a is defined via,

$$\underline{V}^{-f} = \underline{S}_{11}^a \underline{V}^{+f} \Big|_{\underline{V}_A=0} \quad (5-6)$$

This matrix has been shown [14] to be,

$$\underline{S}_{11}^a = 2 [\underline{Y} + \underline{\tilde{\mathcal{E}}} \underline{Y}_a \underline{\mathcal{E}}^*]^{-1} \underline{Y} \quad (5-7)$$

where \underline{Y} and \underline{Y}_a are diagonal matrices of the modal admittance Y_n and Y_{am} for the slit and free-space regions, respectively. From the voltage relations in the two media and the definition of \underline{S}_{11}^a one finds,

$$\underline{S}_{11}^a = \underline{\mathcal{E}}^* (\underline{1} + \underline{S}_{11}^a) \quad (5-8)$$

with $\underline{1}$ being the unity matrix.

* The tilde is the transpose operator, and the asterisk denotes conjugation.

5.2 The Scattering Matrix \underline{S}^0

The determination of the scattering matrix, \underline{S}^0 , at the stripline-to-slitted parallel plate coupling region is developed in an analogous fashion to that for the isolated element scattering matrix (see Chapter 2). An assumed form of electric field is prescribed in the uniform infinite slit. In the infinite stripline region, the equivalence theorem is invoked to replace the slit field by an equivalent magnetic surface current which sustains the internal field distribution in the absence of the slit discontinuity. This equivalent magnetic current is put in a representation of stripline mode functions. From the representation of the magnetic currents, equivalent series voltage source distributions are deduced for each of the modal transmission lines. From a knowledge of the functional relationship of the induced sources to the aperture field amplitude, the modal transmission line voltages and currents are obtained as functions of the aperture field, giving a complete formal description of internal traveling wave scattering due to the transverse slit. In the region external to the stripline, the aperture field is matched to the dominant array mode. Specializing to single mode in the stripline feed and slit, conservation of energy is enforced to obtain the aperture field amplitude. A second relation is obtained for aperture field phase, and a complete traveling wave description of the coupling region is obtained.

For reference, various views of the cell geometry are shown in Figure 5-3.

The aperture electric field is uniform in y and is given by

$$E_{ap} = y_0 \sum_i E_i e^{jk_x |x|} P(y) \quad (5-9)$$

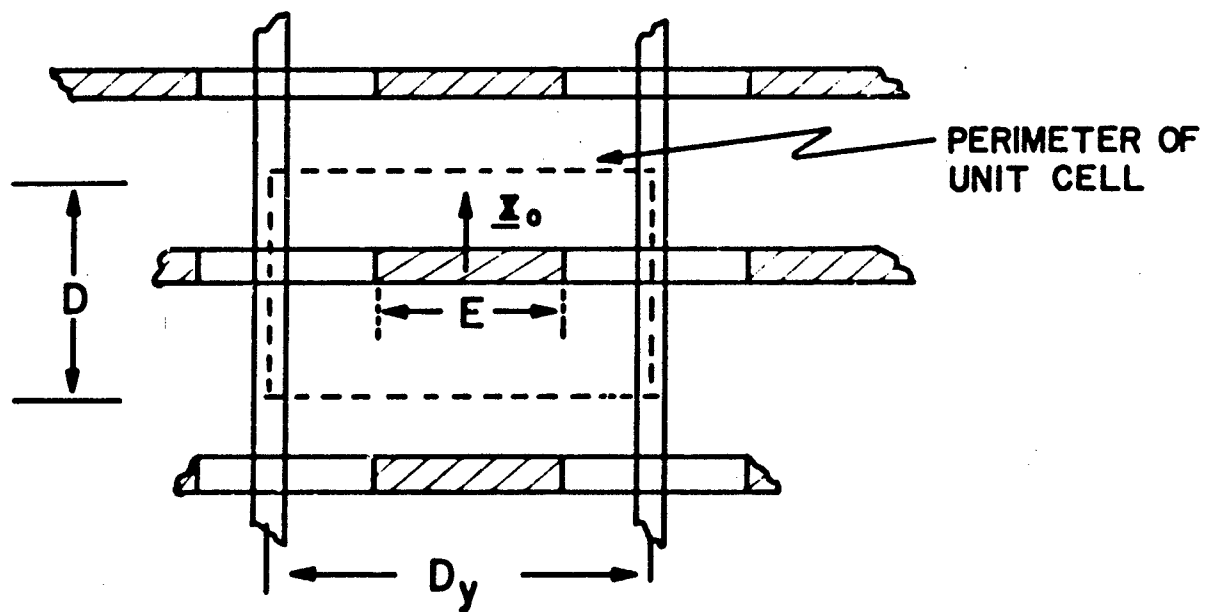
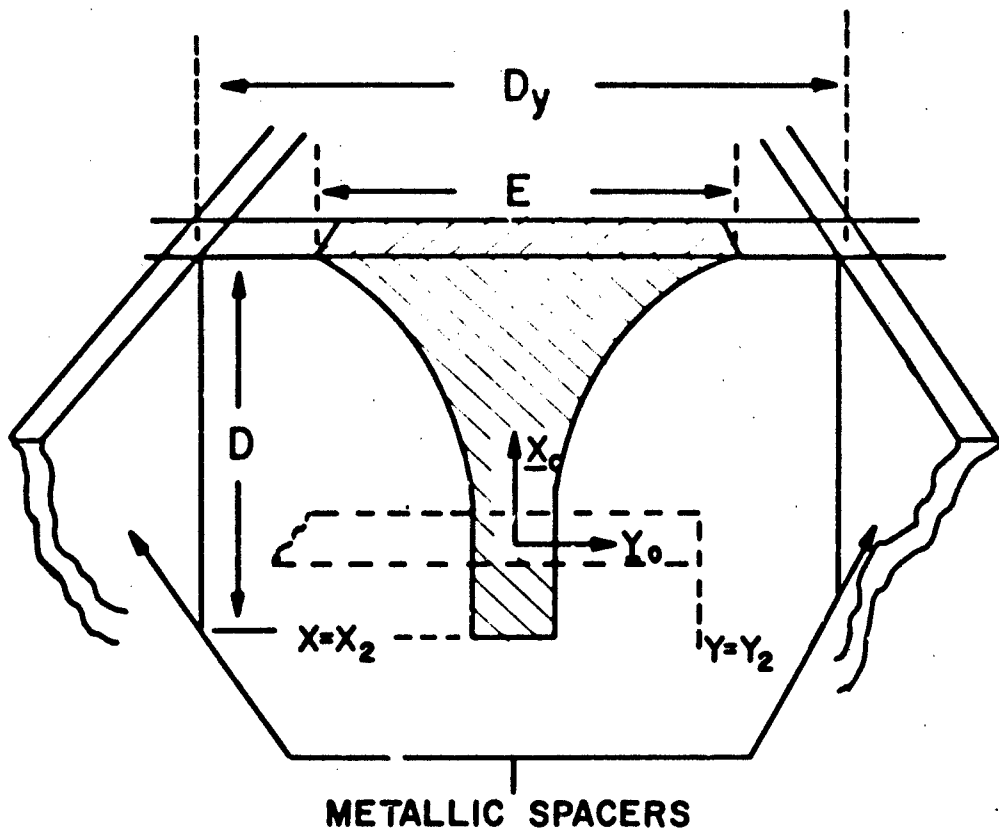


Figure 5-3 Unit Cell Geometry

where

$$P(y) = \begin{cases} 1, & |y| \leq a/2 \\ 0, & |y| > a/2 \end{cases}$$

and k_{x_i} are the modal wavenumbers of the array of slitted parallel plate guides. By the equivalence theorem, the aperture and its assumed electric field distribution are replaced by the equivalent magnetic current density

$$\underline{M}(x) = \underline{z}_0 \times \underline{E}_{ap} [\delta(z - a/2) - \delta(z + a/2)] \quad (5-10)$$

Putting $\underline{M}(x)$ in a representation of stripline mode functions, as

$$\underline{M}(x) = \sum_n \underline{v}_n(y) \underline{h}_n(x, z) \quad (5-11)$$

and enforcing the equality of equations (5-10) and (5-11) over the space spanned by \underline{h}_n results in an expression for the modal voltage coefficients, $\underline{v}_n(x)$, given as

$$\underline{v}_n(y) = \iint_{C_s} \underline{M}(x) \cdot \underline{h}_n(x, z) dC_s \quad (5-12)$$

where C_s is the transverse stripline cross-section. For the slit geometry, $\underline{v}_1(x)$ may be identified as a controlled series voltage source excitation of the i^{th} modal transmission line. In analogy to the development for the isolated element, $\underline{v}_n(x)$ may be expressed as

$$\underline{v}_n(y) = \sum_i \underline{E}_i \underline{e}_{i_n} \quad (5-13)$$

where the coupling coefficients, ϵ_{in} , are given by equation 2-6. Since the coupling coefficients, ϵ_{in} , are identical (save for the k_{xi}) to those appearing in the isolated element results, the single mode results for the isolated element may be applied directly to obtain the total feedguide transmission line voltages at the reference planes, $y = \pm a/2$ for feed excitation V_a^+ . These voltages are given by

$$V(-a/2) = V_f^+ + \frac{a\epsilon_0\epsilon_r}{2} e^{-ju} \frac{\sin u}{u} \quad (5-14)^*$$

$$V(a/2) = V_f^+ e^{-2ju} - \frac{a\epsilon_0\epsilon_r}{2} e^{-ju} \frac{\sin u}{u} \quad (5-15)$$

where $u = k \sqrt{\epsilon_r} a/2$. The second term of equation 5-14 is recognized as the total reflected voltage due to the aperture discontinuity, V_g^- .

Since the modal fields of the array of slitted parallel plates are uniform in y , matching of electric field in the slit plane must be accomplished via a functional best fit. The total array transverse to x electric field is given by

$$\underline{E}_t = \sum \hat{V}_n \hat{e}_n \quad (5-16)$$

where \hat{V}_n is the modal voltage amplitude of the n^{th} array mode, \hat{e}_n (the modes of periodic arrays of slitted parallel plate guide are developed and discussed in Chapter 4). At the slit plane, $z = \pm h/2$,

$$\underline{E}_t(x) = \underline{E}_{ap}(x) \quad (5-17)$$

* The plane $y = -a/2$ has been arbitrarily chosen as the phase reference plane for the stripline region.

or

$$\sum_i \hat{V}_i \hat{E}_i \Big|_{z=\pm h/2} = y_0 \sum_p E_p e^{-j k_{z,p} |x|} P(y) \quad (5-18)$$

where it is recognized that the right hand side (RHS) exists only in the aperture plane, $z = h/2$.

Extending the domain of definition of the aperture field such that the tangential electric field is zero on the ground planes yields,

$$E_{ap} = \begin{cases} y_0 \sum_i E_i e^{-j k_{z,i} |x|} P(y), & z = \pm h/2 \\ 0 & , \text{elsewhere} \end{cases} \quad (5-19)$$

Substituting equation (5-19) for the RHS of equation (5-18) and forming appropriate inner products with \hat{E}_n over the extended domain results in

$$\hat{V}_n(x) = 2 E_n^*(h/2) a \sum_i E_i e^{-j k_{z,i} |x|} \quad (5-20)$$

A unique phase velocity for each mode in x requires for the single mode approximation that,

$$\hat{V}_0(x) = 2 a E_0 e^*(h/2) e^{-j k_{z,0} |x|} \quad (5-21)$$

For stripline excitation V_g^+ conservation of energy requires

$$|V_g|^2 / \eta_c = |V_g|^2 / \eta_c + |V(h/2)|^2 / \eta_c + 2 \frac{k_{z,0}}{\omega \mu} |\hat{V}(0)|^2 \quad (5-22)$$

where V_g^- is the second term on the RHS of equation (5-14). Making appropriate substitutions in equation 5-22 for V_g^- , $V(a/2)$, and $\hat{V}(o)$ from equations (5-14), (5-15), and (5-21), respectively, and rearranging results in an expression for the unknown aperture field coefficient, E_o given as

$$|E_o| = \cos(\pi + \phi_o + \phi_e + u) \frac{|V_g^+| |E_o| \sin u}{2k_o a |\hat{e}(h/2)|^2 + 2a |E_o|^2 \frac{\sin^2 u}{u}} \quad (5-23)$$

where ϕ_o is the phase of E_o and ϕ_e is the phase of E_{oo} . As was found for the single notch element, the requirement of conservation of energy results in an expression for the magnitude of the aperture field in terms of its phase. Thus, a second independent relation for either $|E_o|$ or ϕ_o (or between both) is required to uniquely specify E_o , and hence, V_g^- , $V(a/2)$, and $V(o)$. This second relation (for ϕ_o) is obtained from equation 2-24, where

$$G_{ap} = 2 \frac{k_o}{\omega \mu} \frac{|\hat{e}(h/2)|^2}{|E_o|^2} \quad (5-24)$$

and B_{ap} is derived from the uniformly excited slit approximation presented in Appendix B.

From the above results the definition of \underline{S}^o is straight forward. Figure 5-4 defines the terminal pairs for the stripline-to-slitted parallel plate region. The particular choices of notation for parts 1 and 4 are made to coincide with the notation of Figure 5-2. Thus, for voltage excitation vector $\{V_1^+, V_2^+, V_3^+, V^- \}$ we have

$$\begin{pmatrix} V_f^- \\ V_2^- \\ V_3^- \\ V^+ \end{pmatrix} = \underline{S}^o \begin{pmatrix} V_f^+ \\ V_2^+ \\ V_3^+ \\ V^- \end{pmatrix} \quad (5-25)$$

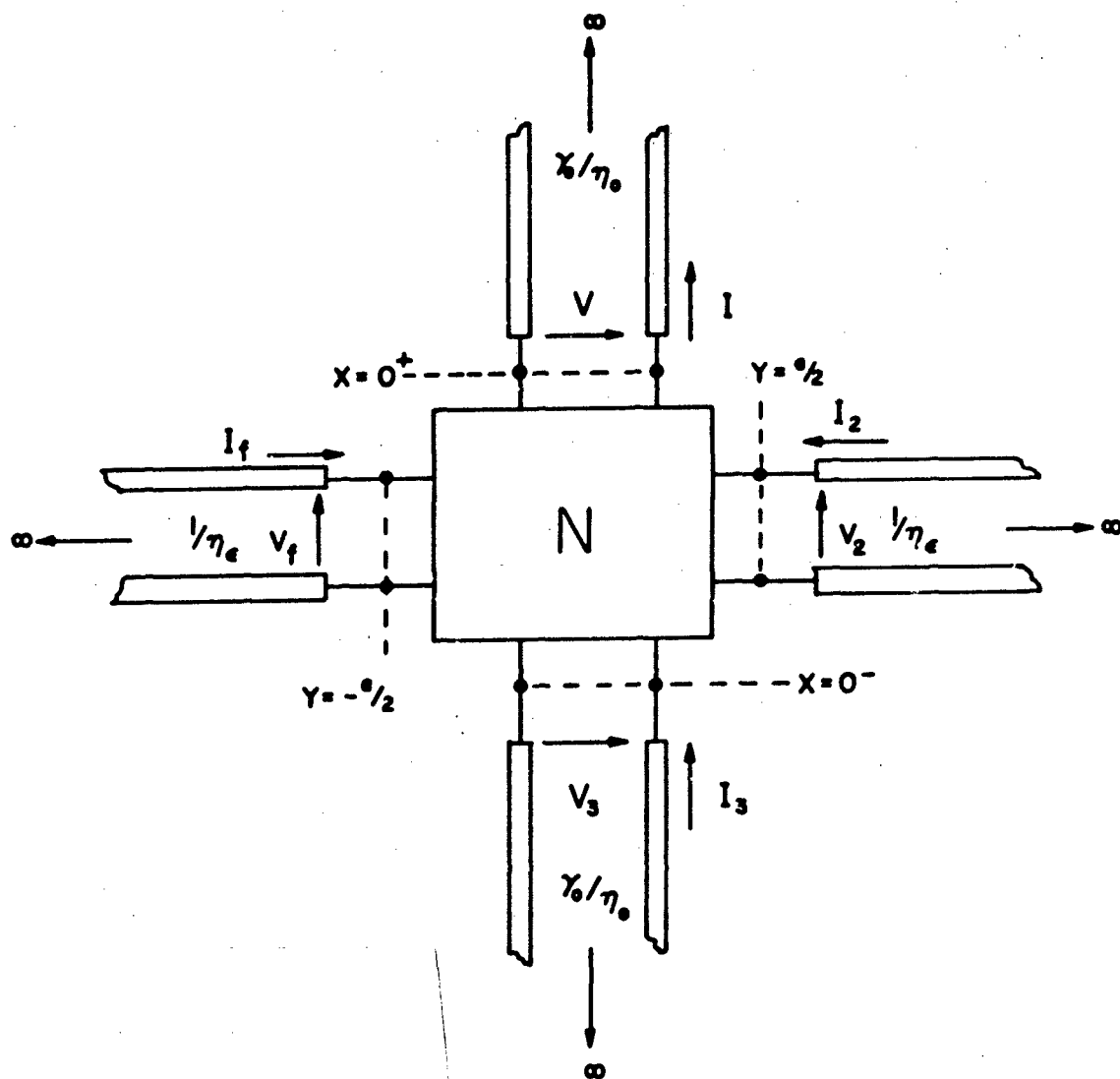


Figure 5-4 Network Definitions for Stripline-to-Slitted Parallel Guide Coupling Region

Applying reciprocity and symmetry arguments one finds,

$$S^0 = \begin{pmatrix} S_{11}^0 & S_{21}^0 & \bar{\eta} S_{31}^0 & -\bar{\eta} S_{41}^0 \\ S_{21}^0 & S_{11}^0 & -\bar{\eta} S_{31}^0 & -\bar{\eta} S_{41}^0 \\ S_{31}^0 & -S_{31}^0 & S_{33}^0 & S_{43}^0 \\ S_{31}^0 & -S_{31}^0 & S_{43}^0 & S_{33}^0 \end{pmatrix} \quad (5-26)$$

where $\bar{\eta} = k_{x_0}/k_0 \sqrt{\epsilon_r}$. Making appropriate identifications with V_g^+ , V_g^- , $V(a/2)$, and $V(0)$, we can write,

$$\begin{aligned} S_{11}^0 &= \left. \frac{V_1^-}{V_1^+} \right|_{V_2^+ = V_3^+ = V^- = 0} = \frac{V_g^-}{V_g^+} \\ &= \frac{u \epsilon_0 \epsilon_r}{2V_g^+} e^{-j\mu} \frac{\sin u}{u} \end{aligned} \quad (5-27)$$

$$S_{21}^0 = \left. \frac{V_2^-}{V_1^+} \right|_{V_2^+ = V_3^+ = V^- = 0} = \frac{V(a/2)}{V_g^+} = e^{-j\mu} - S_{11}^0 \quad (5-28)$$

$$\begin{aligned} S_{31}^0 &= \left. \frac{V_3^-}{V_1^+} \right|_{V_2^+ = V_3^+ = V^- = 0} = \frac{V(0)}{V_g^+} \\ &= 2u \frac{\epsilon_0}{V_g^+} e_0 (h/2) \end{aligned} \quad (5-29)$$

By requiring losslessness,

$$S_{33}^0 = \frac{1}{2} \frac{S_{31}^0 (S_{21}^{0*} - S_{11}^{0*})}{S_{31}^{0*}} - 1 \quad (5-30)$$

and

$$S_{43}^0 = 1 + S_{33}^0 \quad (5-31)$$

The scattering matrix \underline{S}^0 exhibits the broadband characteristic. Figure 5-5 shows the variation of $|S_{11}^0|$ and $|S_{31}^0|$ with frequency for a fixed array geometry and for $k_d/\pi = 0$ (no scan). As seen from the figure, there is only a small change in either scattering matrix element over a 3:1 frequency band.

5.3 The Transmission Matrix \underline{T} of the Flared Notch Region

The transmission matrix \underline{T} , connecting the scattering matrix at the upper interface, \underline{S}^a , to the scattering matrix of the coupling region, \underline{S}^0 , is developed for single mode. The flared region is assumed to consist of piecewise uniform equal length segments. Provided that the granularity of this approximation is sufficiently fine, (slow variation in wavenumbers known in results of Chapter 4) the piecewise approximation is an appropriate representation of the non-uniform region. Numerical results indicate that for the small notch elements considered, a ten-segment approximation is sufficient.

For single mode, the transmission matrix \underline{T} representing the network N in Figure 5-2, is obtained by multiplication of the junction transmission matrices (evaluated at the junctions of the uniform segments) and the uniform line transmission matrices, where \underline{T} is defined in terms of the network terminal voltages via

$$\begin{pmatrix} v^+ \\ v_o^- \end{pmatrix} = \underline{T} \begin{pmatrix} v^{+l} \\ v_o^{-l} \end{pmatrix} \quad (5-32)$$

\underline{T} is then given by

$$\underline{T} = \prod_{i=1}^I \underline{A}_{i-1}^j \underline{A}_i^d \quad (5-33)$$

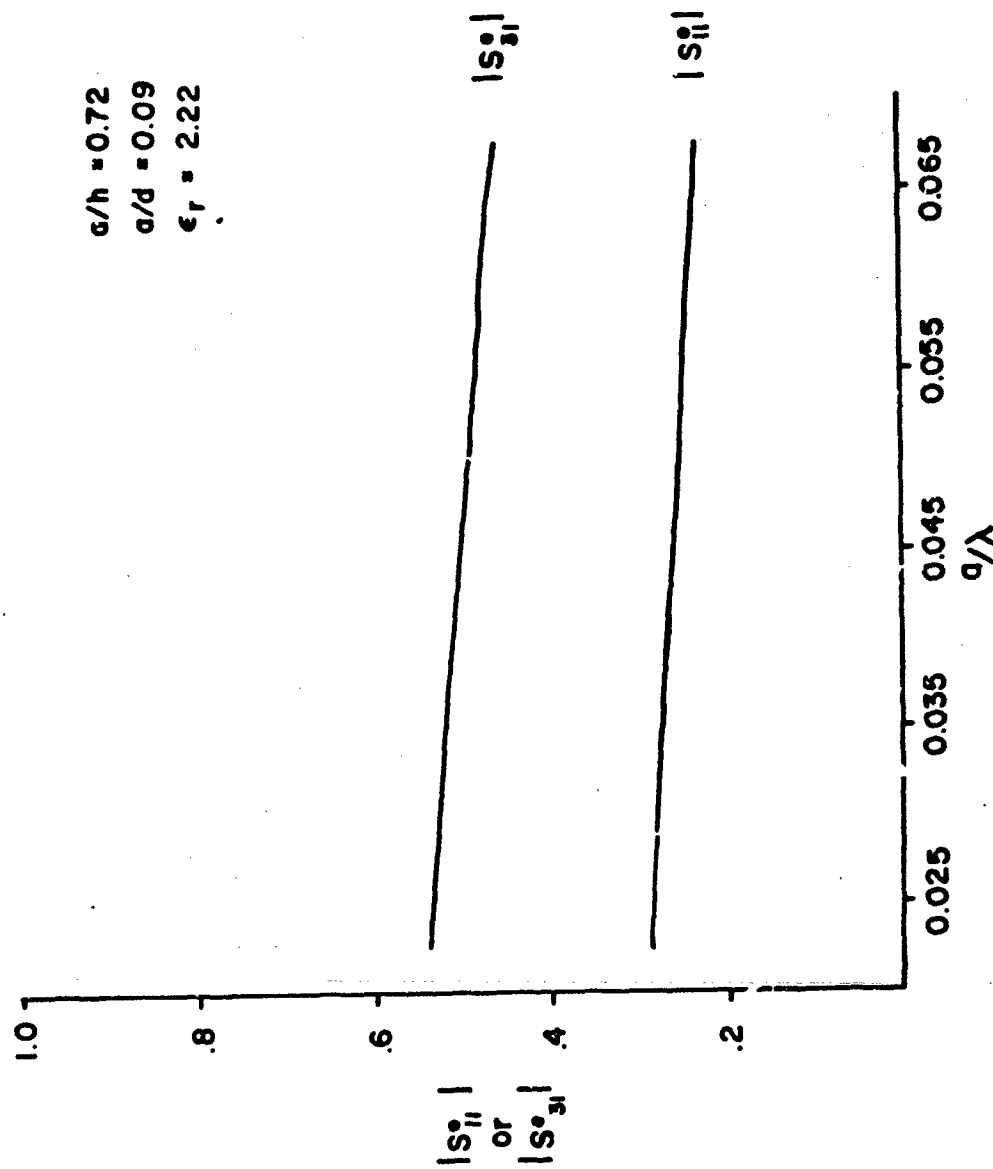


Figure 5-5 Modulus of Scattering Parameters S_{11}^o and S_{31}^o vs a/λ
 $k_d/\pi = 0$

where \underline{A}_{i-1}^j is the transmission matrix representing the junction of the $(i-1)^{th}$ segment and the i^{th} segment: \underline{A}_i^d is the transmission matrix representing the i^{th} uniform line segment; and the segments are ordered from right to left with respect to the network representation in Figure 5-2.

For the p^{th} junction, the junction transmission matrix \underline{A}_{p-1}^j is given by

$$\underline{A}_{p-1}^j = \begin{pmatrix} a_{11}^j & a_{12}^j \\ a_{21}^j & a_{22}^j \end{pmatrix}, p = 0, 1, \dots, z-1 \quad (5-34)$$

where

$$a_{11}^j = a_{22}^j = \frac{Y_{p-1} + Y_p}{2Y_{p-1}} \quad (5-35)$$

$$a_{12}^j = \frac{Y_{p-1} - Y_p}{2Y_{p-1}} \quad (5-36)$$

$$a_{21}^j = a_{12}^j \quad (5-37)$$

where $Y_n = k_n / \omega \mu$ is the characteristic admittance of segment n .

The elements of the g^{th} uniform line transmission matrix

$$\underline{A}_g^d = \begin{pmatrix} a_{11}^d & a_{12}^d \\ a_{21}^d & a_{22}^d \end{pmatrix} \quad (5-38)$$

are given by

$$a_{11}^d = e^{jk_{zy}\Delta} \quad (5-39)$$

$$a_{22}^d = a_{11}^{d*} \quad (5-40)$$

$$a_{12}^d = a_{21}^d = 0 \quad (5-41)$$

where Δ is the length of the uniform line segment.

5.4 The Active Array Reflection Coefficient

From the definitions of \underline{S}^o and \underline{S}^a , one has for arbitrary stripline mode excitation,

$$\underline{V}_f^- = \underline{S}_{11}^o \underline{V}_f^+ + \underline{S}_{12}^o \underline{V}^- \quad (5-42)$$

$$\underline{V}^+ = \underline{S}_{21}^o \underline{V}_f^+ + \underline{S}_{22}^o \underline{V}^- \quad (5-43)$$

$$\underline{V}^{-l} = \underline{S}_{11}^a \underline{V}^{+l} \quad (5-44)$$

$$\underline{V}^{+a} = \underline{S}_{21}^a \underline{V}^{+l} \quad (5-45)$$

A set of auxiliary relations for the network have also been found where,

$$\underline{V}^+ = \underline{T}_{11} \underline{V}^{+l} + \underline{T}_{12} \underline{V}^{-l} \quad (5-46)$$

$$\underline{V}^- = \underline{T}_{21} \underline{V}^{+l} + \underline{T}_{22} \underline{V}^{-l} \quad (5-47)$$

Using (5-44) in (5-46) and (5-47) and solving V in terms of \underline{V}^+ one finds

$$\underline{V}^+ = \underline{M} \underline{V}^- \quad (5-48)$$

where $\underline{M} = (\underline{T}_{11} + \underline{T}_{12} \underline{S}_{11}^a) (\underline{T}_{21} + \underline{T}_{22} \underline{S}_{11}^a)^{-1}$

Solving for \underline{V}^- in (5-b) and using the result in (5-43) yields active array reflection

$$\underline{V}_f^- = (\underline{S}_{11}^o + \underline{S}_{12}^o (\underline{M} - \underline{S}_{22}^o)^{-1} \underline{S}_{21}^o) \underline{V}_f^+ \quad (5-49)$$

Array transmission coefficient is found using (5-43), (5-44) (5-45) and (5-47):

$$\underline{V}_a^+ = \underline{S}_{21}^o \underline{B}^{-1} (\underline{M} - \underline{S}_{22}^o)^{-1} \underline{S}_{21}^o \underline{V}_f^+ \quad (5-50)$$

where

$$\underline{B} = (\underline{T}_{21} + \underline{T}_{22} \underline{S}_{11}^a)$$

For the one mode approximations, the active reflection coefficient reduces to

$$\frac{V_f^-}{V_f^+} = \Gamma = S_{11}^o + S_{21}^o \frac{V_2^+}{V_f^+} + \bar{\gamma} S_{31}^o \frac{V_3^+}{V_f^+} + \bar{\gamma} S_{31}^o \frac{V_f^-}{V_f^+} \quad (5-51)$$

where the port conventions of Figure 5-4 have been used and

$$V_2^+ = \vec{\Gamma}_2 e^{-jk_0(2y_2-a)} V_2^- \quad (5-52)$$

$$V_3^+ = -e^{2jk_0x_0} V_3^- \quad (5-53)$$

$$V^- = \vec{\Gamma}_4 e^{-2jk_0x_0} V^+ \quad (5-54)$$

In equations 5-52 and 5-54, $\vec{\Gamma}_2$ is the reflection coefficient due to the open circuit stripline termination as seen at $y = y$ (see equation 2-36), x_0 is the distance from $x = 0$ to the beginning of the flare, and $\vec{\Gamma}_4$ is given by

$$\begin{aligned} \vec{\Gamma}_4 &= \frac{V^-}{V^+} \Big|_{x=x_0} \\ &= \frac{T_{21}V^{+l} + T_{22}V^{-l}}{T_{11}V^{+l} + T_{12}V^{-l}} \end{aligned} \quad (5-55)$$

5.5 Numerical Results

The calculation of active array reflection coefficient follows from equation 5-51, which is a single mode specialization of equation 5-49. In the calculations, it is assumed that only the $n = 0$ array mode is coupled to the stripline excitation. The higher order array modes are assumed terminated in their own characteristic impedances at $x = -\infty$, and are coupled only at the aperture plane, $x = l$. These approximations are justified by the well matched interface at $x = l$, and by the higher mode attenuation in the notch region. Moreover, higher mode effects are partially included at the feed discontinuity by the assumed circuit for determination of \underline{S}^0 .

Two array configurations have been selected for modeling. Both configurations are square lattice. An array typical of this lattice is shown in Figure 5-6. The dimensions of the two arrays

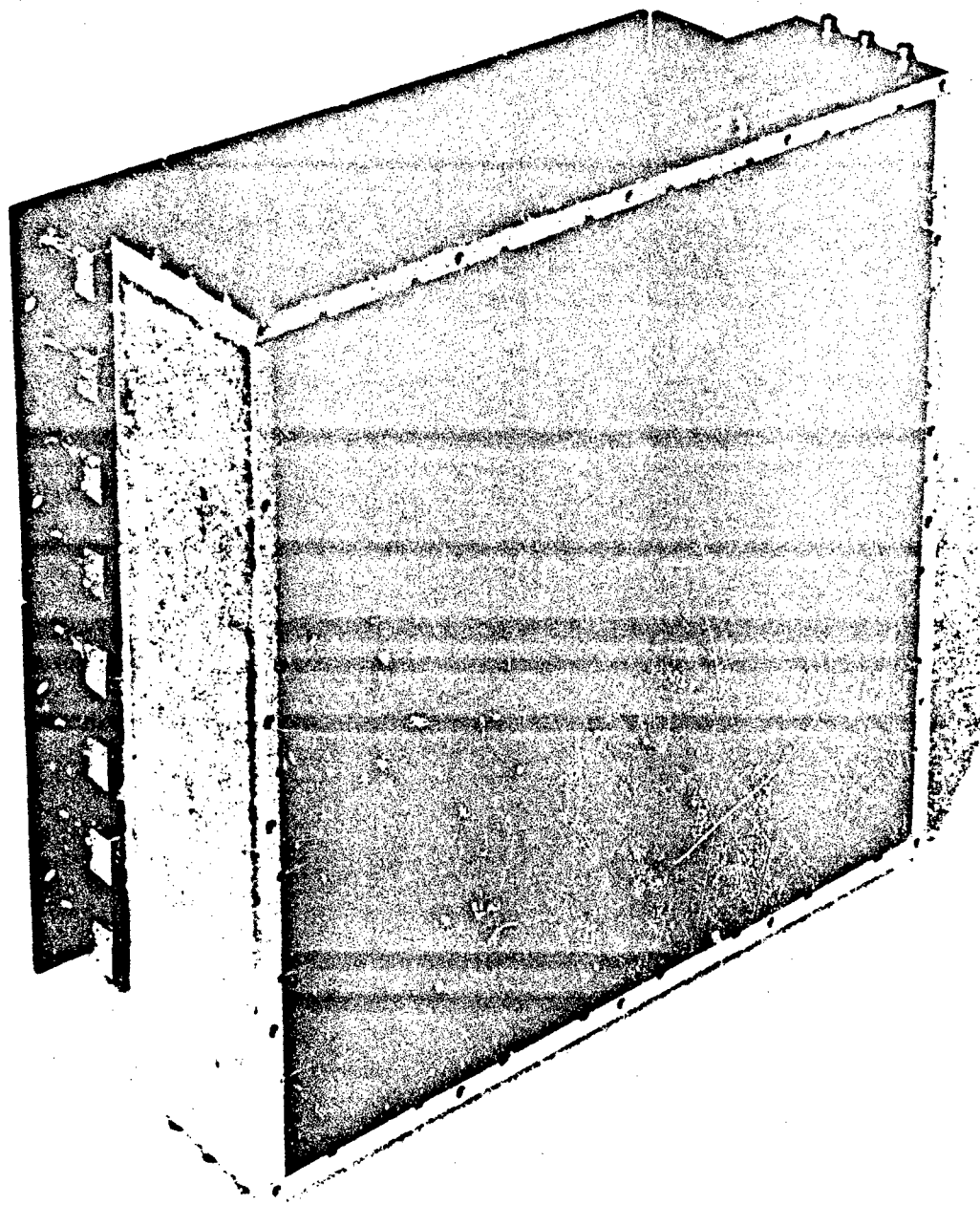


Figure 5-6 - 64 Element "Egg Crate" Array

73-67162

are given in Table 5-1 with respect to free-space wave length at low frequency for the pertinent operating bands. The elements of array 1 are element #5 of Table 5-1. These elements have been shown both theoretically and experimentally (see Chapter 2), to be well matched over a 3:1 frequency band (isolated). Array 2 has been built and tested, and exhibits nearly full array gain over an octave band.

Computed active array reflection coefficient, is shown with parameter d/λ versus H-plane scan angle, θ , in Figure 5-7 and 5-8 for arrays 1 and 2, respectively. The element spacing for array 1 is such that an end fire grating enters at midband. For array 2, no grating lobes appear.

As seen in Figure 5-7, array 1 is well matched out to approximately 70° scan at low frequency. The reflection coefficient remains below .333 (VSWR of 2:1) out to approximately 25° , and below .5 (VSWR of 3:1) out to approximately 70° . As end fire is approached, $|r|$ increases rapidly to 1. For $d/\lambda = .55$ (just above midband) a grating lobe enters for $\theta = 54.9^\circ$. The array remains well matched out to approximately 25° . The resonance at $\theta = 40.5^\circ$ corresponds to entry of the $n = -1$ array^[14,15] mode at $\theta = 39.1^\circ$. At high frequency the grating lobe enters at $\theta = 19.5^\circ$, with a resonance at $\theta = 14^\circ$. For $d/\lambda = .75$, the reflection coefficient is above .4 out to the appearance of the grating lobe.

For array 2, the element spacing is such that neither the -1. space harmonic nor the -1 array mode comes in. Thus, as seen in Figure 5-8, resonances do not occur. At low frequency $d/\lambda = .245$, $|r|$ remains below .333 out to approximately 47° , and below .5 out to approximately 60° , being better matched off-broadside. For $d/\lambda = .367$, $|r|$ remains above .38 throughout, and below .5 out to 30° . For $d/\lambda = .465$, the match is poor at broadside, but improves as the array is scanned out to 33° . Beyond 40° , $|r|$ rises rapidly.

Array	d/λ_0	E/λ_0	D/λ_0	Frequency Range
1	.25	.1875	.1875	$f_0 - 3f_0$
2	.245	.204	.635	$f_0 - 2f_0$

TABLE 5-1

Pertinent Array Data with Respect to λ_0 at Low Frequency.

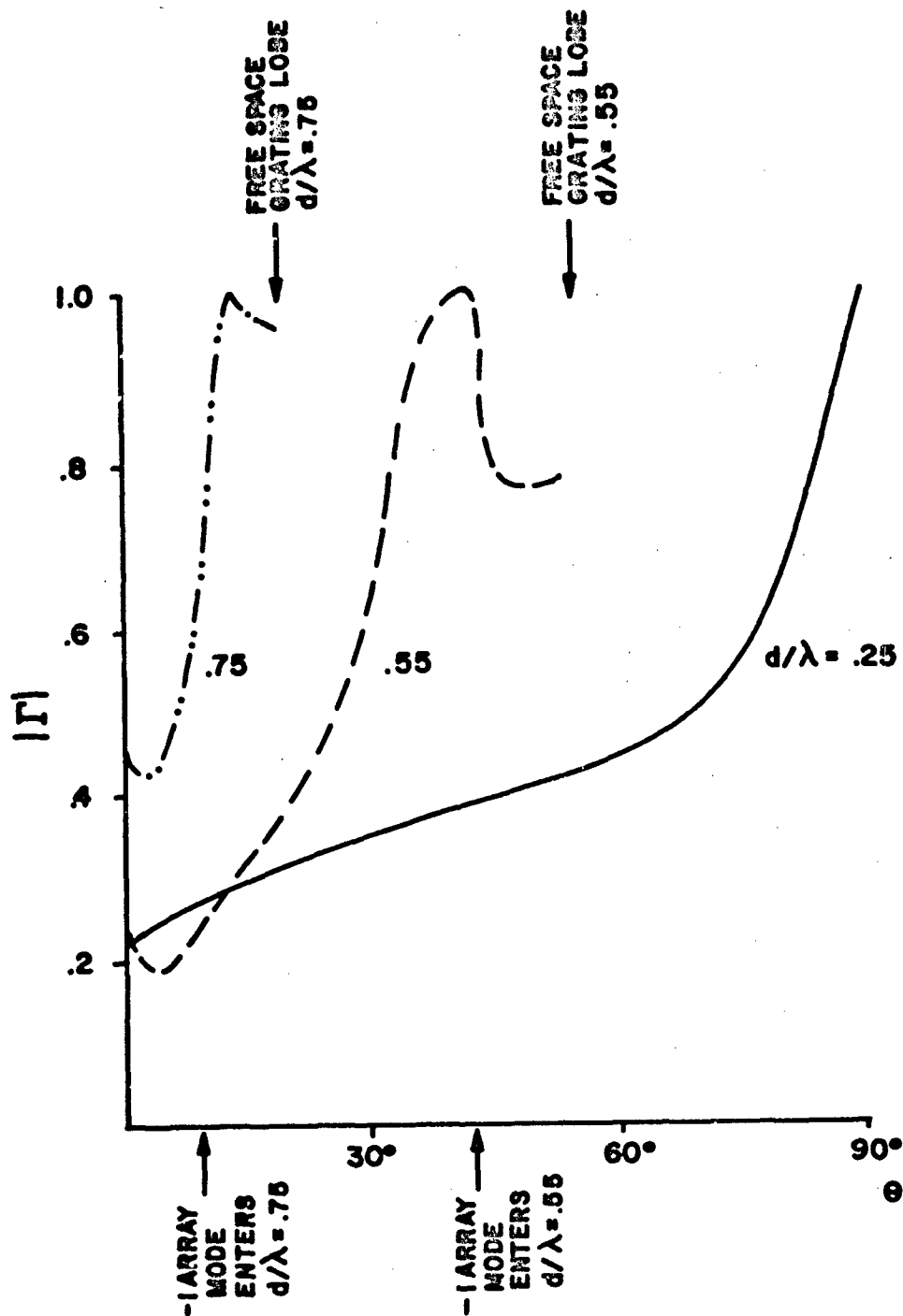


Figure 5-7 Array 1 Active Reflection Coefficient
vs H-Plane Scan Angle θ
105

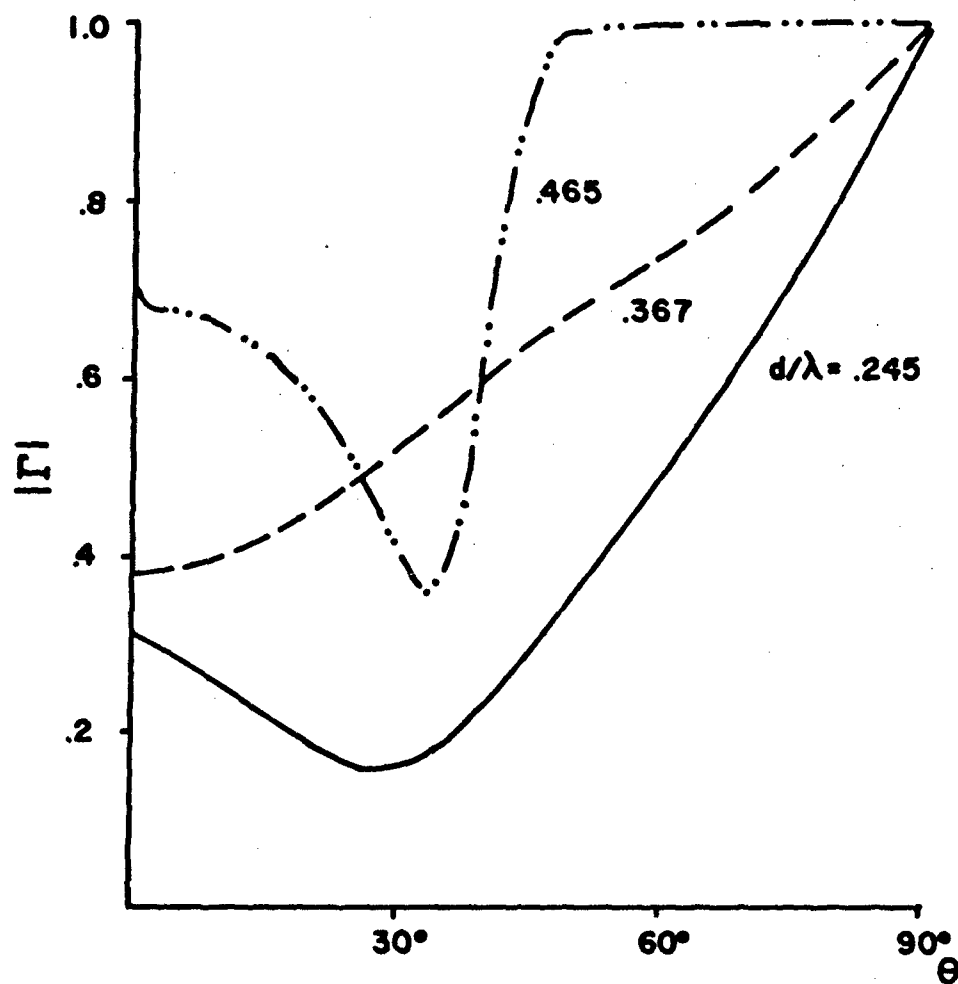


Figure 5-8 Array 2: Active Array Reflection Coefficient
vs H-Plane Scan Angle, θ

Figure 5-9 shows the active array reflection coefficient for array 2 when scanned in the E-plane. For $d/\lambda = 0.245$ and $d/\lambda = 0.367$, $|r| < .5$ beyond $\theta = 60^\circ$, then rapidly goes to 1 as end fire is approached. For $d/\lambda = 0.465$, $|r| > .67$ for all scan angles.

H-plane array element patterns, $(1 - |r|^2) \cos\theta$, are shown in Figures 5-10 through 5-12 for the two array configurations, with parameter d/λ . In Figures 5-10 and 5-11 the resonances exhibited occur just after the $n = -1$ array mode begins propagating. Only nominal gain loss (approximately 1dB) is observed over the 3:1 band. For array 2, the element patterns in Figure 5-12, shows increasing gain loss at broadside as frequency is increased. At the high frequency, $d/\lambda = .465$, the broadside gain loss is approximately 3dB.

Typical E-plane element patterns are shown in Figure 5-13 for array 2. For $d/\lambda = .465$, the array is better matched off-broadside. At the lower frequencies, the patterns are broad and, essentially differ only in level, consistent with broadside gain loss.

Calculated element patterns have been compared to measured gain for E-plane scanning of array 2 over a 2:1 band. The overall agreement is found to be excellent. Figures 5-14 through 5-16 show these comparisons for scan angles of 0° , 30° , and 45° versus frequency. The measured array gain is presented with respect to theoretical full array gain. At broadside, the calculated results are within 1dB of measured gain over most of the band. The notch appearing near $1.5f_0$ in the measured results has been associated with a connector problem, and a more representative curve would follow theoretical results more closely. This notch also appears in the measured results shown in Figures 5-15 and 5-16. In general, the calculated results are seen to form an envelope for the measured data. At 45° scan, this

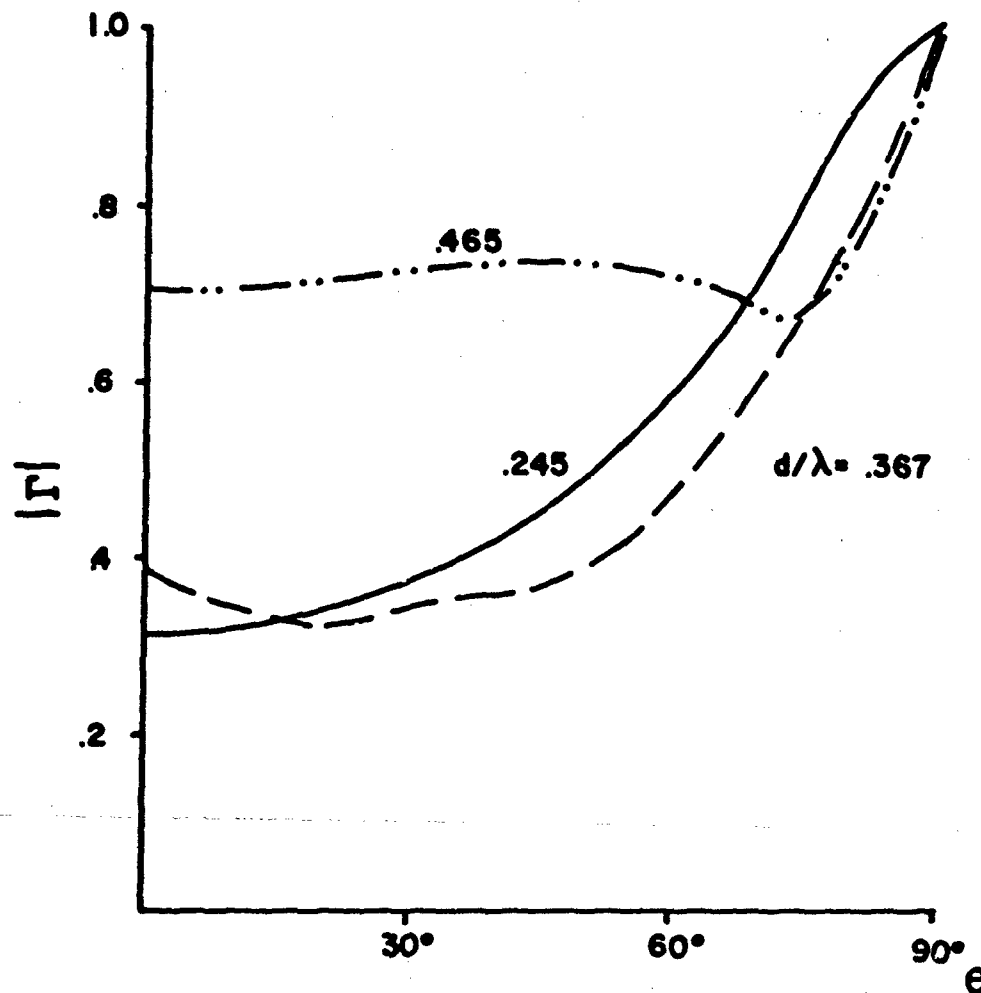


Figure 5-9 Array 2: Active Array Reflection
Coefficient vs E-Plane Scan Angle, θ
108

envelope is approximately 1dB above measured gain over the entire band. However, as is found for broadside, the shape of the envelope is in excellent agreement with measured data.

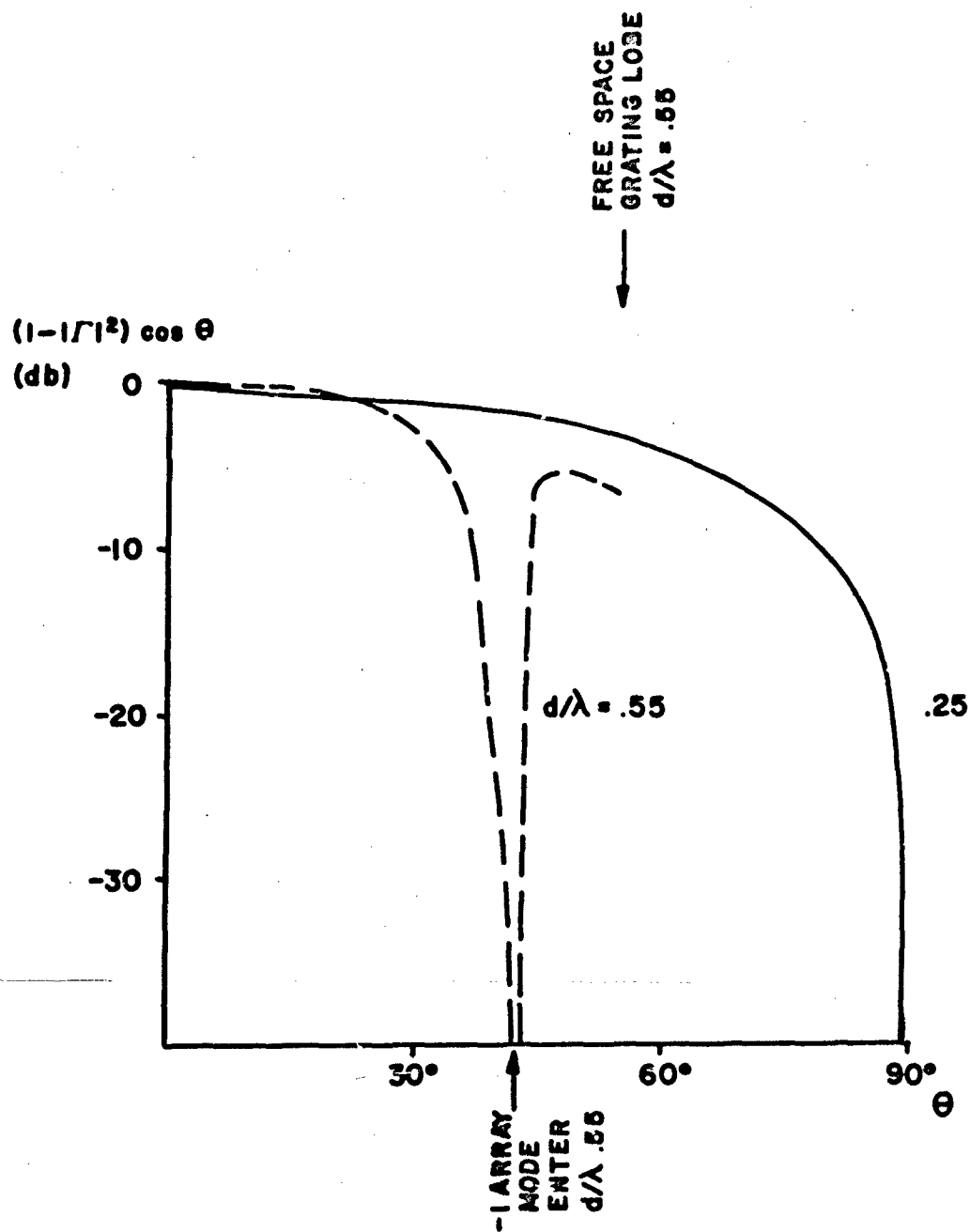


Figure 5-10 Array 1: Active Array Element Pattern,
H-Plane

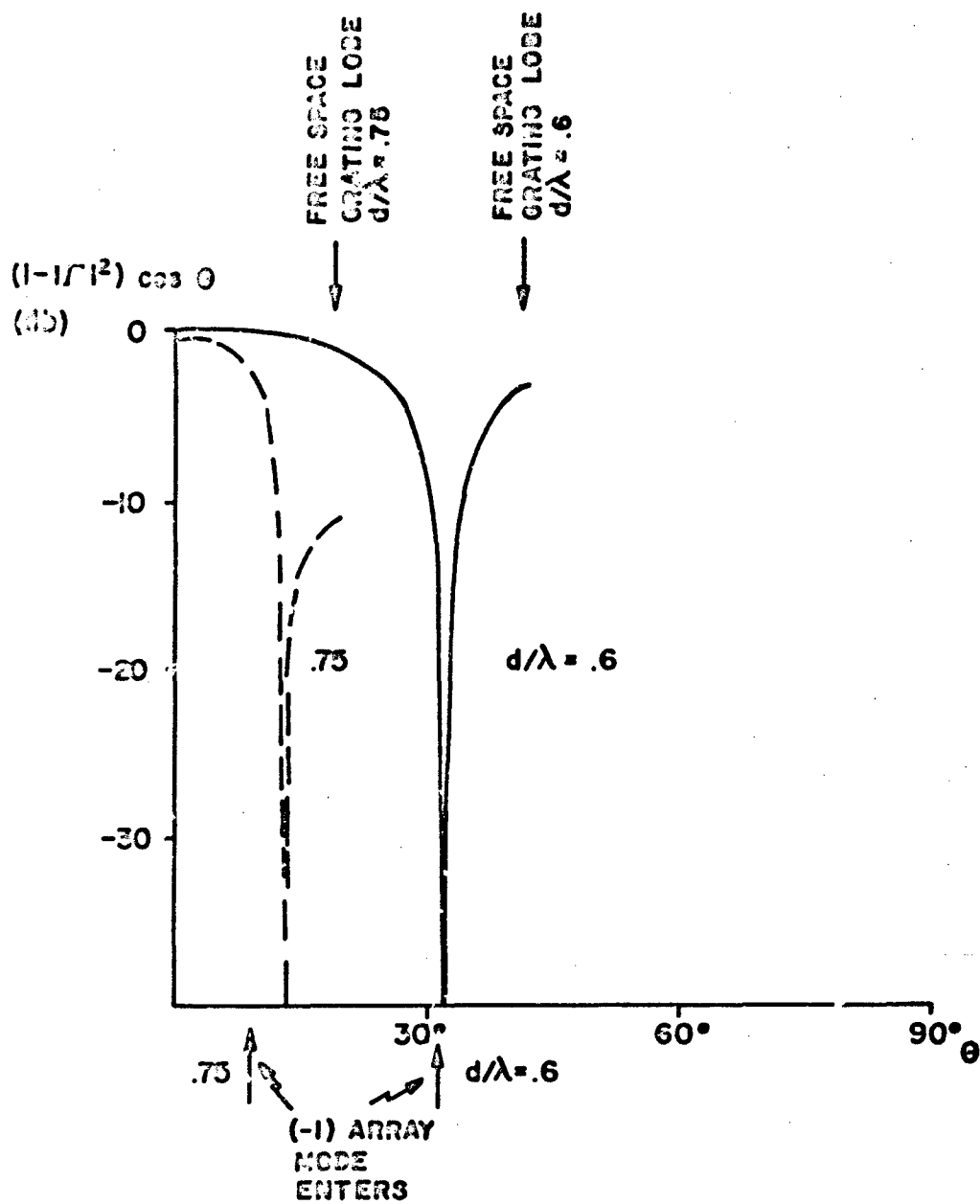


Figure 5-11 Array 1: Active Array Element Pattern,
H-Plane

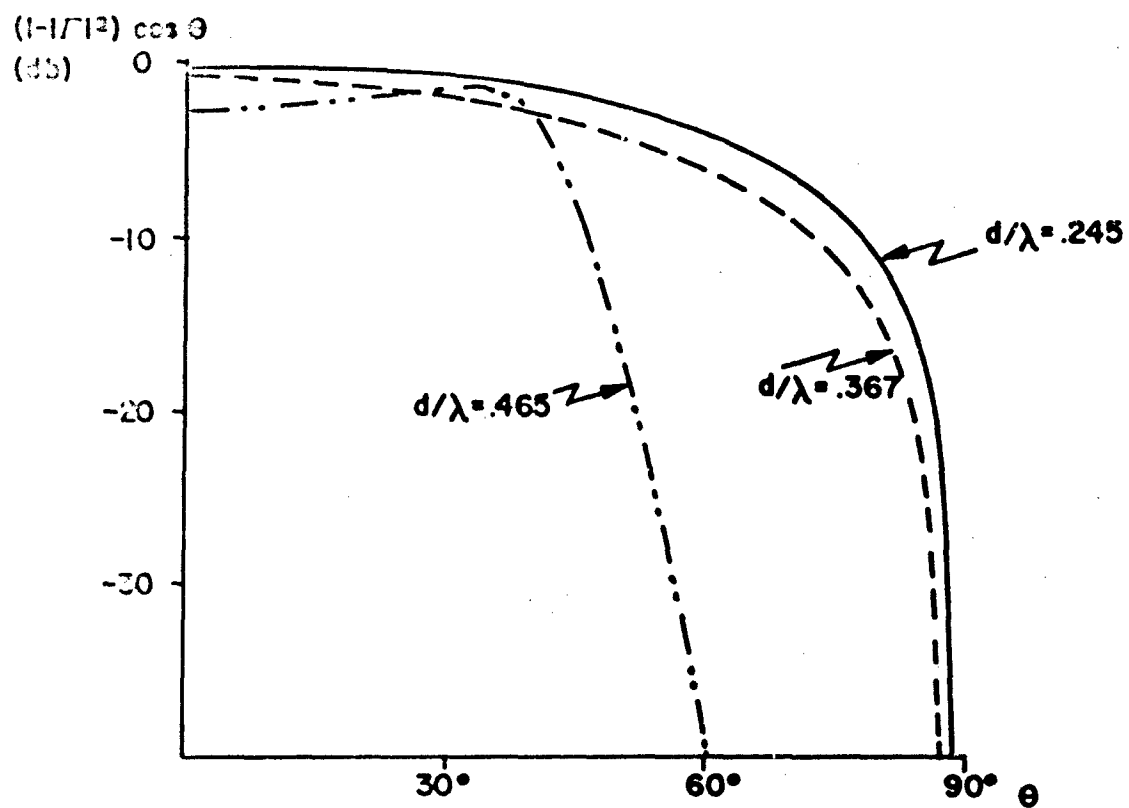


Figure 5-12 Array 2: Active Array Element Pattern,
H-Plane

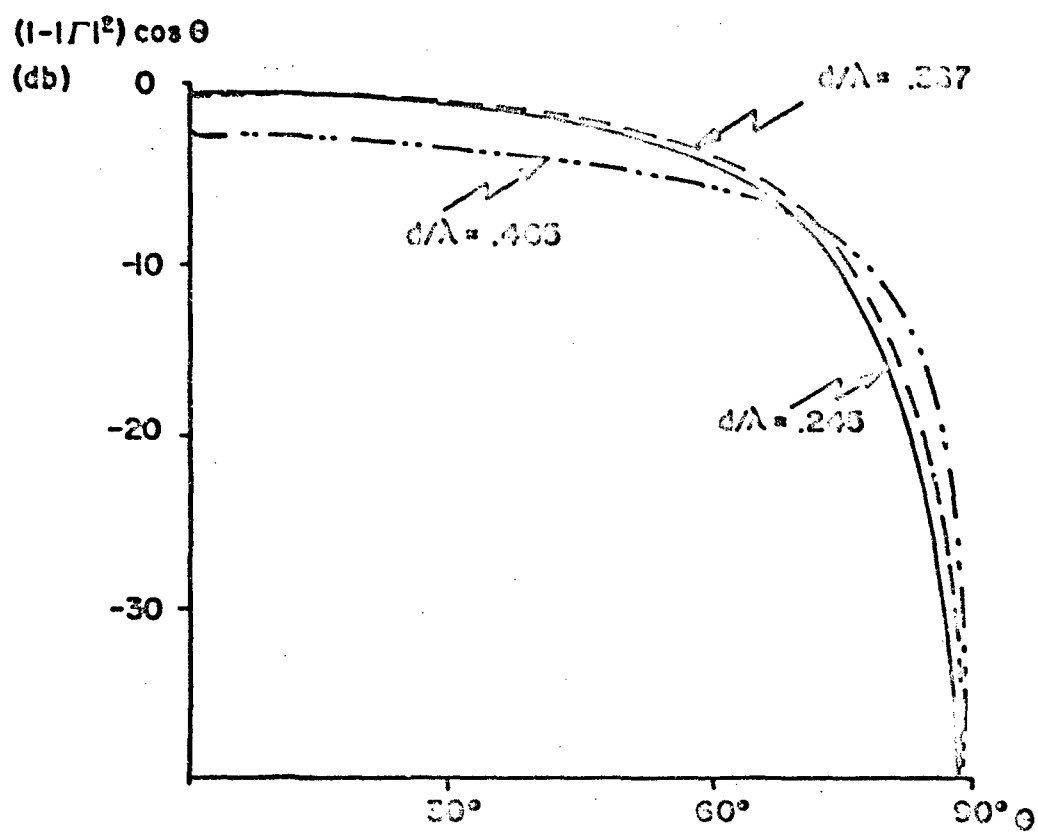


Figure 5-13 Array 2: Active Array Element Pattern,
E-Plane

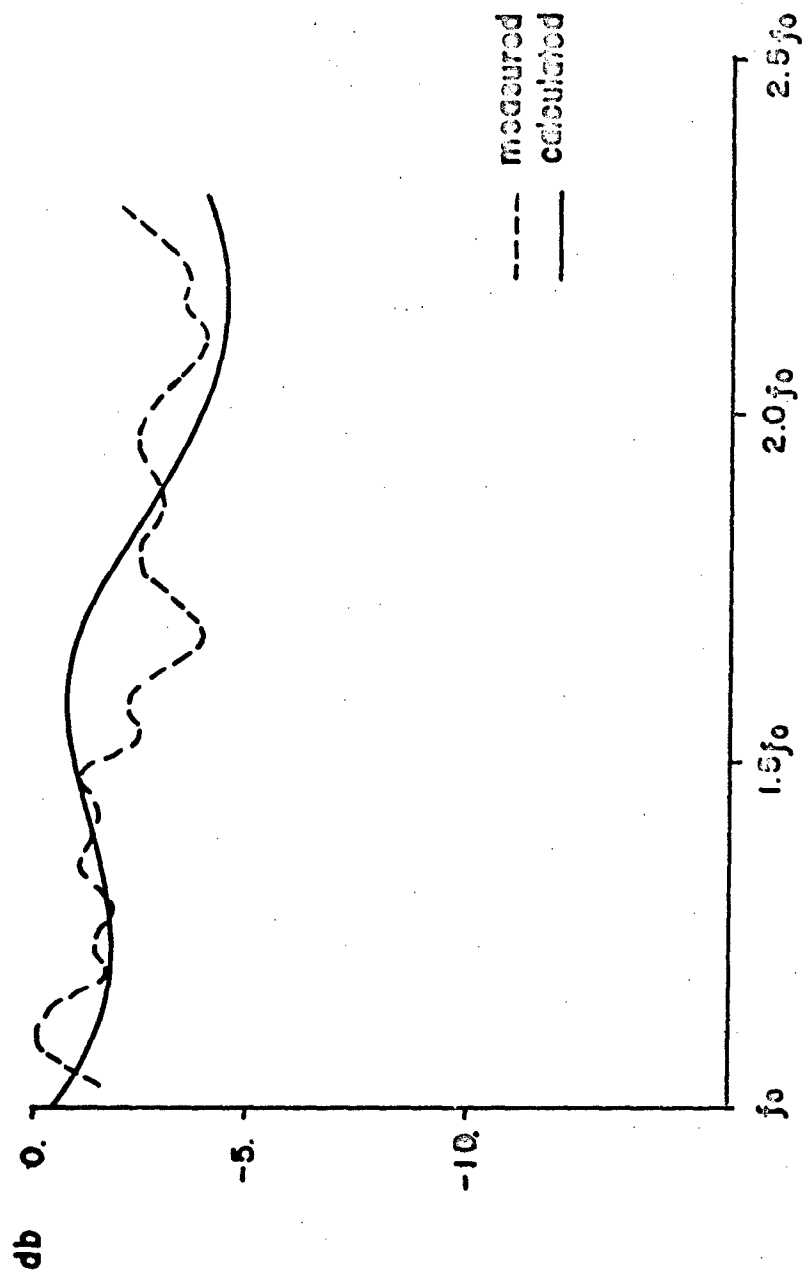


Figure 5-14 Array 2: Measured Array Directive Gain Relative to Theoretical Full Array Gain and Calculated Active Array Element Gain Relative to Cell Gain VS Frequency, Broadside Scan

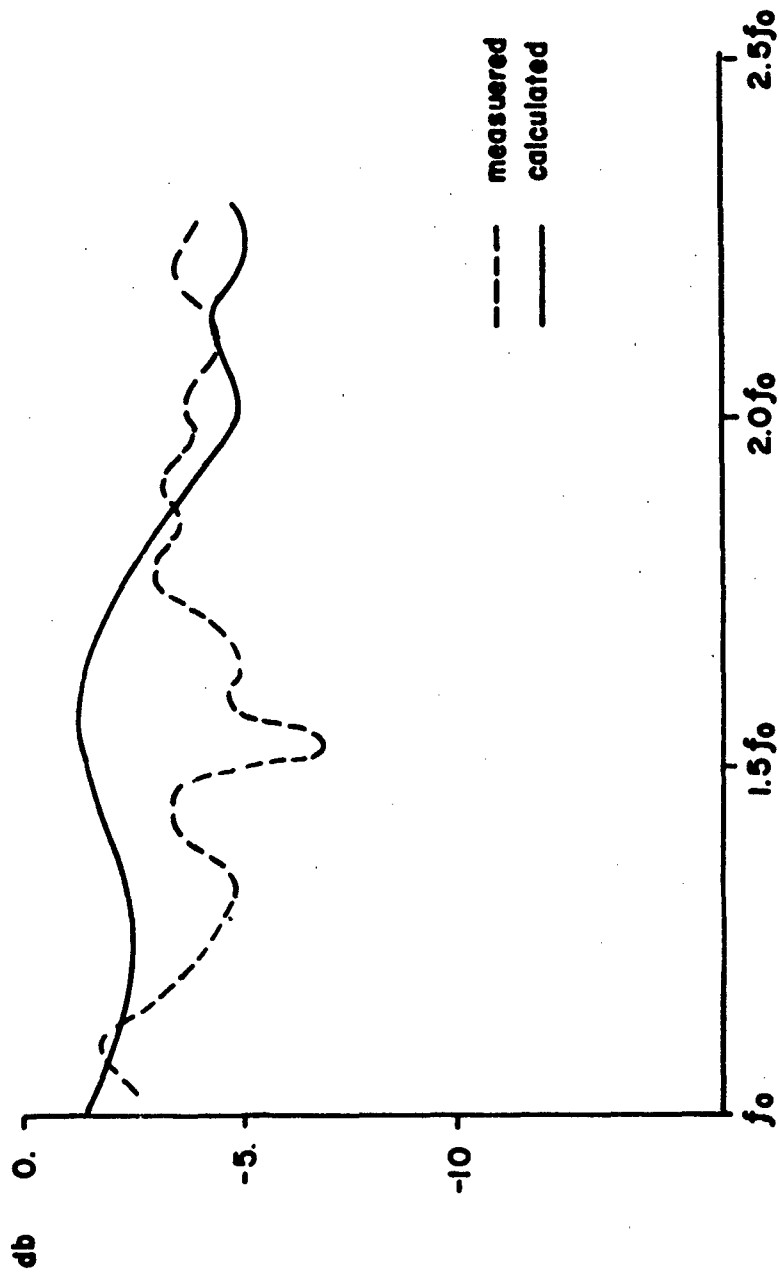


Figure 5-15 Array 2: Measured Array Directive Gain Relative to Theoretical Full Array Gain and Calculated Active Array Element Gain Relative to Cell Gain VS Frequency, E-Plane Scan Angle = 30°

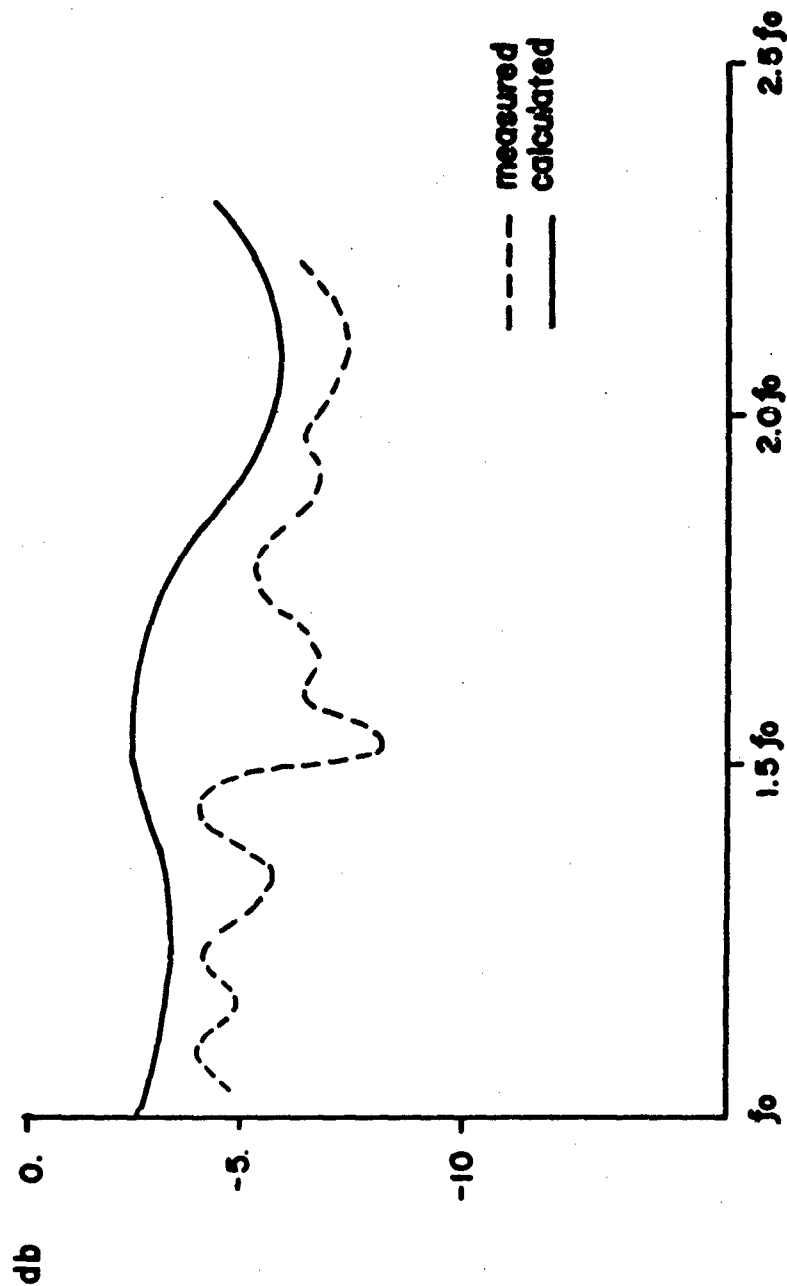


Figure 5-16 Array 2: Measured Array Directive Gain Relative to Theoretical Full Array Gain and Calculated Active Array Element Gain Relative to Cell Gain \sqrt{S} Frequency, E-Plane
Scan Angle = 45°

6. CONCLUSIONS

The stripline fed flared notch antenna has been shown to be a broadband radiator, capable of octave or greater bandwidths, in both isolated element and infinite array configurations. As shown by theoretical considerations, the broadband nature of the element is associated primarily with the stripline-to-notch coupling region and the proper selection of planes for the notch and center conductor terminations.

Analysis of the coupling regions for both isolated element and infinite array configurations has been restricted to the dominant modes of the stripline and notch regions. Higher order modes have been partially included via the expressions for slit susceptance. The numerical results obtained from dominant mode analysis have shown excellent agreement with measured data for two broadband notch elements in the isolated configuration, and with a 256 element scanning array. The computed results for the E-plane scanning array are in agreement with measured array gain loss to within 1dB over an octave band and 45° scan range. For the isolated configurations, the theory predicts the occurrence of the low frequency cut-off at slightly higher frequencies. However, calculations of isolated element reflection coefficient are within .1 of measured results over 2:1 and 3:1 frequency bands, respectively, for the elements considered.

Wave slowing has been observed for H-plane active array element patterns for one of the arrays considered. The slowing produces dips in the H-plane active element patterns at high frequencies, and consequently poses a restriction on the high frequency scan volume. The scan volume may be increased by appropriate change in element spacing.

Appendix A

Stripline TEM Mode Functions

The stripline TEM mode functions, \underline{e} and \underline{h} , are developed by determining the static electric and magnetic fields in the stripline region, and then normalizing them such that

$$\iint_{C_s} \underline{E}_t \cdot \underline{E}_t^* dC_s = 1 \quad (\text{A-1})$$

where C_s is the stripline cross-section as shown in Figure A-1. In the following, subscripts 1, 2, 3, and 4 will refer to the regions of Figure 1 in which the particular expressions are valid. Subscript "t" refers to transverse fields.

To within two unknown constants, A_m and C_p , the potential distributions for symmetric stripline in regions 1 through 3 are given as [16]

$$V_1(x, z) = \sum_{m=1}^{\infty} A_m \cosh \frac{2m\pi x}{h} (-1)^m \sin \frac{2m\pi z}{h} - \frac{2V_0}{h} z \quad (\text{A-2})$$

$$V_2(x, z) = \sum_{m=1}^{\infty} A_m \cosh \frac{2m\pi x}{h} \sin \frac{2m\pi z}{h} + \frac{2V_0}{h} z \quad (\text{A-3})$$

$$V_3(x, z) = \sum_{p=1}^{\infty} C_p e^{-p\pi x/h} (-1)^p \sin \frac{2p\pi z}{h} \quad (\text{A-4})$$

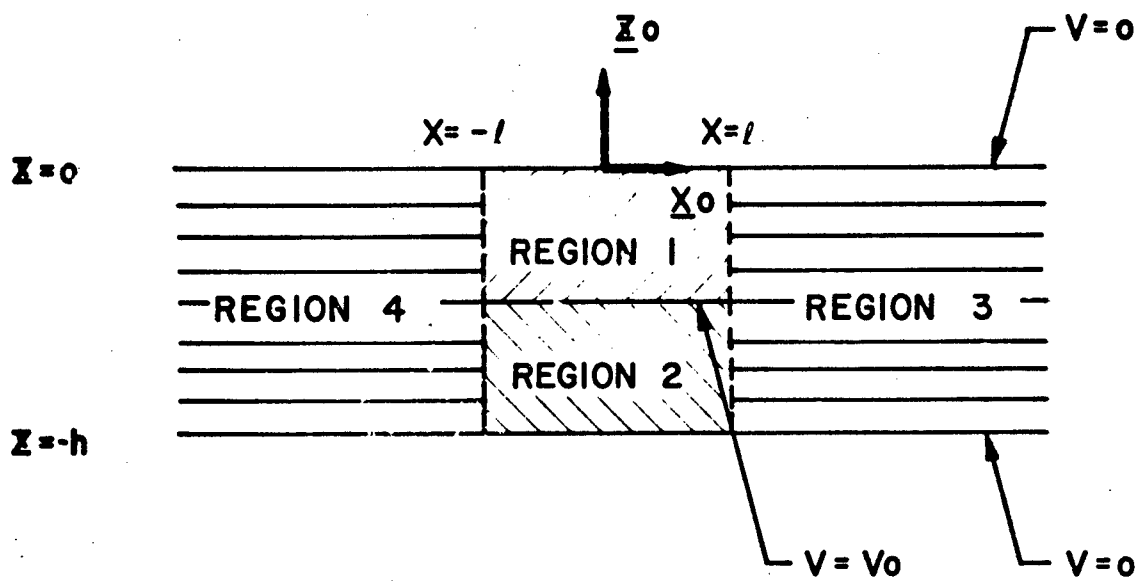


Figure A-1 Stripline Cross-Section

It has been assumed that the center conductor is infinitesimally thin. From symmetry it must follow that

$$\begin{aligned} \text{i. } V_1(x, z) &= V_2(x, -h-z) \\ \text{ii. } V_3(x, z) &= V_3(x, -h-z) \end{aligned}$$

where $0 \geq z \geq -h/2$.

$$\begin{aligned} \text{a. } V_1(x, z) &= \sum_m A_m \cosh \frac{2m\pi x}{h} (-1)^m \sin \frac{2m\pi z}{h} - \frac{2V_0}{h} z \\ V_2(x, -h-z) &= -\sum_m A_m \cosh \frac{2m\pi x}{h} \sin \frac{2m\pi z}{h} - \frac{2V_0}{h} z \end{aligned}$$

Therefore condition i is satisfied if m is odd.

b. Similarly, condition ii is satisfied if p is odd.

Let the potential distribution at $x = \pm l$ be given as

$$\Phi(z) = \begin{cases} -\frac{2V_0}{h} z + \phi(z), & 0 \geq z \geq -h/2 \\ \frac{2V_0}{h}(h+z) + \phi(z+h), & -h/2 \geq z \geq -h \end{cases} \quad (\text{A-5})$$

where

$$\phi(z) = \sum_{n=1}^{\infty} q_n \sin \frac{2n\pi z}{h} \quad (\text{A-6})$$

It is reasonable to assume that the potential distributions at $x = \pm l$ are approximately linear, i.e. $\phi(z) = 0$. With this approximation

$$A_n = 0 \quad (\text{A-7})$$

and

$$C_p e^{-p\pi l/h} = \frac{8V_0}{(p\pi)^2} \sin p\pi/2 \quad (\text{A-8})$$

The approximate potential distributions are then,

$$V_1(x, z) \approx -\frac{2V_0}{h} \quad (A-9)$$

$$V_2(x, z) \approx \frac{2V_0}{h} (h+z) \quad (A-10)$$

$$V_3(x, z) \approx -8V_0 \sum_{\substack{p=1 \\ \text{odd}}}^{\infty} e^{p\pi(1-x)/h} \frac{\sin \frac{p\pi}{2} \sin \frac{p\pi z}{h}}{(p\pi)^2} \quad (A-11)$$

The total electric field is given as

$$\underline{E} = -e^{jk_y y} \nabla V \quad (A-12)$$

and the magnetic field is

$$\underline{H} = j \frac{1}{k_y \eta_0} \nabla \times \underline{E} \quad (A-13)$$

where $\eta_0 = 120$ ohms. For TEM waves, the magnetic field equation must reduce to

$$\underline{H} = j \frac{k_z}{k_y \eta_0} \underline{y}_0 \times \underline{E} \quad (A-14)$$

or

$$\frac{\partial}{\partial z} E_x - \frac{\partial}{\partial x} E_z = 0 \quad (\text{A-15})$$

which results in

$$\frac{\partial}{\partial z} \frac{\partial}{\partial x} V - \frac{\partial}{\partial x} \frac{\partial}{\partial z} V = 0 \quad (\text{A-16})$$

Equation A-16 is clearly satisfied by the potentials given above.

The approximate electric and magnetic fields are then given as:

$$E_1 = \frac{2V_0}{h} e^{jk_y y} \underline{z}_0 \quad (\text{A-17})$$

$$E_2 = -\frac{2V_0}{h} e^{jk_y y} \underline{z}_0 \quad (\text{A-18})$$

$$E_3 = -\frac{8V_0}{h} e^{jk_y y} \left\{ x \sum_{n=1}^{\infty} e^{\frac{n\pi}{h}(l-x)} \frac{\sin \frac{n\pi}{2} \sin \frac{n\pi}{h} z}{n\pi} \right. \\ \left. - z_0 \sum_{\substack{n=1 \\ \text{odd}}}^{\infty} e^{\frac{n\pi}{h}(l-x)} \frac{\sin \frac{n\pi}{2} \cos \frac{n\pi}{h} z}{n\pi} \right\} \quad \text{A-19}$$

$$\underline{H}_1 = \frac{k_z}{k_0 \gamma_0} \underline{y}_0 \times \underline{E}_1 \quad (\text{A-20})$$

$$\underline{H}_2 = \frac{k_z}{k_0 \gamma_0} \underline{y}_0 \times \underline{E}_2 \quad (\text{A-21})$$

$$\underline{H}_3 = \frac{k_z}{k_0 \gamma_0} \underline{y}_0 \times \underline{E}_3 \quad (\text{A-22})$$

These expressions possess all the necessary symmetries and are continuous at $x = \underline{L}$, $z = 0-h$. As might be expected, the nature of the approximation for the potential distribution at $x = \underline{L}$, i.e. $\underline{\Phi}(x)$ results in $E_{3x}(l, z) \neq 0$ and $H_{3x}(l, z) \neq 0$ for $z \neq 0, -h/2, -h$.

The mode functions are defined as

$$\underline{\hat{e}} = -\nabla \underline{V} \quad (\text{A-23})$$

$$\underline{\hat{h}} = \underline{y}_0 \times \underline{\hat{e}} \quad (\text{A-24})$$

such that $Q_e\{\hat{V}\hat{I}\}$ is power and the characteristic impedance is the TEM wave impedance thus,

$$\underline{e}_1 = \frac{2W}{h} \underline{z}_0 \quad (\text{A-25})$$

$$\underline{e}_2 = -\frac{2N}{h} \underline{z}_0 \quad (A-26)$$

$$\underline{e}_3 = -\frac{2N}{h} \left\{ \underline{z}_0 \sum_{p=1}^{\infty} e^{\frac{2p\pi}{h}(1-x)} \frac{\sin \frac{2p\pi}{h} \sin \frac{2p\pi}{h} y}{p\pi} \right. \quad (A-27)$$

$$\left. - \underline{z}_0 \sum_{p=1}^{\infty} e^{\frac{2p\pi}{h}(1-x)} \frac{\sin \frac{2p\pi}{h} \cos \frac{2p\pi}{h} y}{p\pi} \right\} \quad (A-28)$$

$$\underline{h}_1 = y_0 \times \underline{e}_1$$

$$\underline{h}_2 = y_0 \times \underline{e}_2 \quad (A-29)$$

$$\underline{h}_3 = y_0 \times \underline{e}_3 \quad (A-30)$$

The normalization constant, N , is then determined from

$$\iint_{C_s} \underline{e} \cdot \underline{e} \, dC_s = 1 \quad (A-31)$$

here C_s is the stripline cross-section. The normalization constant N is given as

$$N = \left(\frac{2}{h} + 1.005509020014 \right)^{-1/2} \quad (A-32)$$

The numerical constant is $4 \left(\frac{2}{\pi} \right)^3 \lambda(3)$ where

$$\lambda(3) = \sum_{k=0}^{\infty} (1k+1)^{-3} = (1-2^{-3}) \sum_{k=1}^{\infty} k^{-3}$$

and the last summation is recognized as the Riemann Zeta function.

Appendix B

Slit Susceptance for Slitted Parallel Plate Guide

An infinite slit excited with a uniform electric field is capacitive. Values of this capacitance have been computed by both Marcuvitz [17] and Harrington [9]. In these cases the aperture voltage is taken as aE (a is the slit width), while for the problem under consideration here the aperture voltage is given as $aE_0\epsilon_0$ (see equation (2-23)). This difference of normalization is adjusted by using a transformer at the aperture discontinuity. In this fashion the susceptance as viewed at the terminal pair with voltage aE_0 can be transformed properly to the reference plane with voltage $aE_0\epsilon_0$.

The ratio of aperture voltages is $1/\epsilon_0$ which reflects a $1/\epsilon_0^2$ multiplier to those results of capacitance at the aE_0 reference plane. The capacitance C'_{ap} at the reference plane $V'_{ap} = aE_0$ is $C_{ap} = C'_{ap}/\epsilon_0^2$ at the terminal pair $V_{ap} = aE_0\epsilon_0$.

For the isolated slit, C'_{ap} is given as [17,9]

$$C'_{ap} = \frac{\epsilon}{2\pi} (3.135 - 2 \ln ka) \quad (B-1)$$

For the array of slitted parallel plate guides, the capacitance C'_{ap} is taken as that of a symmetric septum in parallel plate guide, and is given as [10]

$$C'_{ap} = \frac{2\epsilon d_y}{\pi} \left[\ln \csc \frac{\pi a}{2d_y} + \frac{(\frac{\pi}{2d_y r_1} - 1) \alpha_1^2}{1 + (\frac{\pi}{2d_y r_1} - 1) \alpha_2^2} \right] \quad (B-2)$$

where

$$\Gamma_1^2 = \left(\frac{\pi}{2y} \right)^2 - k^2 \quad (\text{B-3})$$

$$\alpha_1 = \cos^2 \frac{\pi a}{2y} \quad (\text{B-4})$$

$$\alpha_2 = 1 - \alpha_1^2 \quad (\text{B-5})$$

Appendix C

Orthonormal Mode Functions of Parallel Plate Regions with Open and Short Circuit Boundaries

Figure C-1 shows a parallel plate region for which the planes $z=0, -h$ are perfect electric conductors (PEC or short circuit boundary) and the plane $z = -h/2$ is a perfect magnetic conductor (PMC or open circuit boundary). The region extends to infinity in x and y . Longitudinal (in y) scalar wave functions satisfying the boundary conditions at the open and short circuit planes and the radiation condition at $x = +\infty$ are:

- (i) longitudinal (in y) electric field E-modes.

$$\phi_n' = A_n \sin k_{zn} z e^{-jk_n x} \quad (C-1)$$

- (ii) longitudinal (in y) magnetic field (H-mode)

$$\phi_m'' = B_m \cos k_{zm} z e^{-jk_m x} \quad (C-2)$$

where

$$k_{zn} = \frac{(2n+1)\pi}{h} \quad (C-3)$$

and A_n and B_m are unknown normalizations.

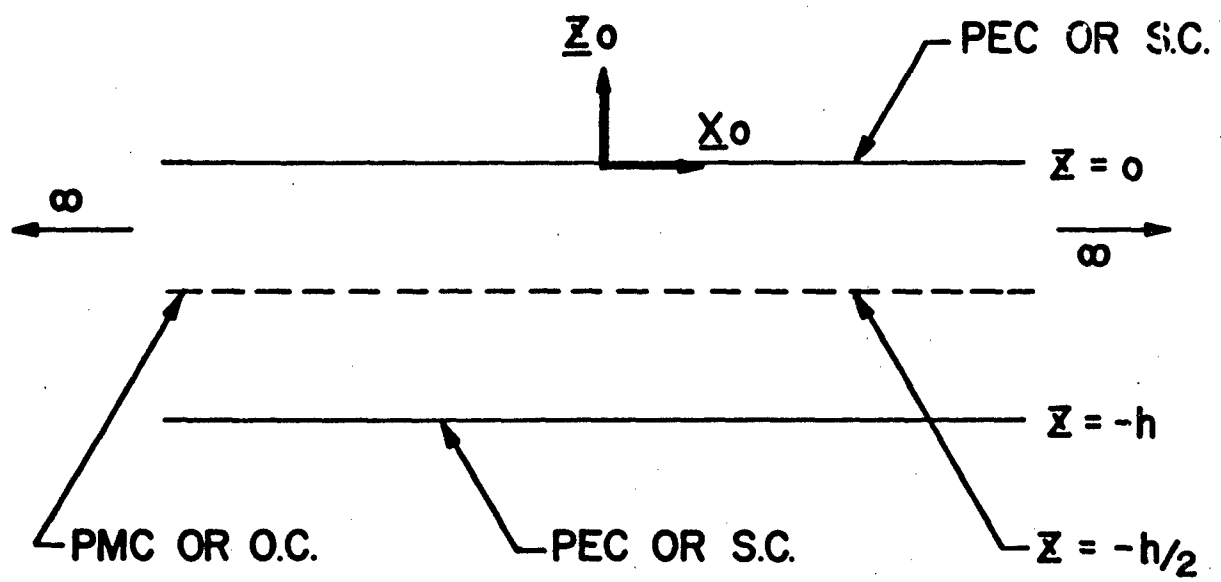


Figure C-1 Parallel Plate Region
with Open and Short Circuit

Boundaries

It then follows that for E-modes, the transverse to y mode functions are given as

$$\underline{e}'_n = -\frac{\nabla_t \phi'_n}{k_{tn}} = \frac{A_n e^{jk_n x}}{k_{tn}} \{x_0 j k_n \sin k_{yn} z - z_0 k_{yn} \cos k_{yn} z\} \quad (C-4)$$

$$\underline{h}'_n = y_0 \times \underline{e}'_n \quad (C-5)$$

where $k_{tn}^2 = k_n^2 + k_{yn}^2$.

For H-modes

$$\underline{h}''_m = -\frac{\nabla_t \phi''_m}{k_{tm}} = \frac{B_m e^{jk_m x}}{k_{tm}} \{x_0 j k_m \cos k_{ym} z + z_0 k_{ym} \sin k_{ym} z\} \quad (C-6)$$

$$\underline{e}''_m = \underline{h}''_m \times y_0 \quad (C-7)$$

The normalization constants A_n and B_m are taken such that

$$\operatorname{Re}\{V_p I_p^*\} = \operatorname{Re}\left\{\frac{k_y}{\omega \mu} |V_p|^2\right\} \quad (C-8)$$

represents real power flow per unit length in x and k_y is the longitudinal wavenumber. Thus

$$\int_{-h}^0 dz \underline{e}'_p \cdot \underline{e}'_g = \delta_{pg} \quad (C-9)$$

$$\int_{-h}^0 dz \, \underline{h}_r'' \cdot \underline{h}_s'' = \delta_{rs} \quad (C-10)$$

where δ_{ij} is the Kronecker delta function

Thus

$$A_n = B_n = \frac{2}{\sqrt{h}} \quad (C-11)$$

With equation C-11, the mode functions are readily extended to the complex k_x domain.

Appendix D

Coupling Coefficients for Slitted Parallel Plate Array to Free Space Transition

The elements of the coupling coefficient matrix, $\underline{\epsilon}$, for the slitted parallel plate array to free space transition are given, for array normal $\hat{n} \parallel \underline{z}_0$ as

$$\epsilon_{grs,n} = \iint_{\text{Cell}} ds \underline{e}_n(\underline{r}) \cdot \hat{\underline{e}}_{grs}(\underline{r}) \quad (\text{D-1})$$

where \underline{r} the generalized position vector

$$\underline{r} = y \underline{y}_0 + z \underline{z}_0 \quad (\text{D-2})$$

$\underline{e}_n(\underline{r})$ is the nth slitted parallel plate array mode function (see Chapter 3), and $\hat{\underline{e}}_{grs}(\underline{r})$ is the space of Floquet mode functions for the mode spectrum (rectangular grid)

$$k_{zg} = \hat{k}_z + g \frac{2\pi}{d} \quad (\text{D-3})$$

$$k_{yr} = \hat{k}_y + r \frac{2\pi}{d} \quad (\text{D-4})$$

The $\hat{\underline{e}}_{grs}(\underline{r})$ are given by [17]

$$\hat{E}_{grs}(\underline{z}) = \frac{1}{\sqrt{d D_y}} \frac{1}{k_{tgr}} e^{-j(k_{yg} z_0 + k_{yr} y_0)} \begin{cases} (2-s)(k_{yg} z_0 + k_{yr} y_0) \\ (s-1)(k_{yg} y_0 - k_{yr} z_0) \end{cases} \quad (D-5)$$

where $s = 1(2)$ for E-(H-) mode with respect to the array normal, \underline{z}_0 , and $k_{tgr}^2 = k_{yg}^2 + k_{yr}^2$. Performing the operations in equation D-1 results in

$$E_{grs,n} = [(2-s)k_{yr} + (1-s)k_{yg}] F_{grs,n} \quad (D-6)$$

and

$$F_{grs,n} = \frac{D_y}{k_{tgr} \sqrt{d D_y}} \frac{\sin k_{yr} D_y/2}{k_{yr} D_y/2} \frac{e^{j k_{yg} \frac{d}{2}}}{N_n} \cdot$$

$$\left\{ \frac{2}{\kappa_n^2 - k_{yg}^2} \left[\kappa_n \sin \theta_n \cos \left(\frac{\kappa_n d}{2} - \frac{k_{yg} h}{2} \right) - k_{yg} \cos \theta_n \sin \left(\frac{\kappa_n d}{2} - \frac{k_{yg} h}{2} \right) \right] \right.$$

$$- j \frac{2}{\kappa_n^2 - k_{yg}^2} \left[\kappa_n (B_1 A_1 + B_2 A_2) + k_{yg} \sin \theta_n (B_1 A_3 - B_1 A_4) \right.$$

$$\left. - \kappa_n \cos \theta_n (B_1 A_4 + B_2 A_3) \right]$$

$$+ \frac{2}{\kappa_n^2 - k_{yg}^2} \left[k_{yg} (C_2 A_4 - C_2 \cos \theta_n - C_1 A_3) + \kappa_n C_1 \sin \theta_n \right]$$

$$- j \frac{2}{\kappa_n^2 - k_{yg}^2} \left[\kappa_n (D_1 A_4 - D_1 \cos \theta_n + D_2 A_3) - k_{yg} D_2 \sin \theta_n \right] \quad (D-7)$$

where

$$\kappa_n = k \sqrt{1 - \gamma_n^2}$$

$$\kappa_{en} = k \sqrt{\epsilon_r - \gamma_n^2}$$

$$\gamma_n = k_{xn}/k$$

$$\theta_n = \kappa_n(d-h)/h, \quad \theta_{en} = \kappa_{en} h/2$$

$$A_1 = \cos k_{y\beta} \frac{d}{2}, \quad A_2 = \sin k_{y\beta} \frac{d}{2}$$

$$A_3 = \sin k_{y\beta} \frac{h}{2}, \quad A_4 = \cos k_{y\beta} \frac{h}{2}$$

$$B_1 = Z Y_d^s \cos \frac{\kappa_d d}{2}, \quad B_2 = Z Y_d^a \sin \frac{\kappa_d d}{2}$$

$$C_1 = \cos \frac{\kappa_d d}{2} (\cos \theta_n - j Z Y_d^s \sin \theta_n)$$

$$C_2 = \sin \frac{\kappa_d d}{2} (\cos \theta_n - j Z Y_d^a \sin \theta_n)$$

$$D_1 = C_1 Z_e Y_1^s, \quad D_2 = C_2 Z_e Y_1^a$$

$$Z Y_d^s = j \frac{\bar{Y}_{en} \tan \theta_n + \bar{B} + \tan \theta_n}{1 - \bar{Y}_{en} \tan \theta_n \tan \theta_n - \bar{B} \tan \theta_n}$$

$$Z Y_d^a = j \frac{\bar{B} - \bar{Y}_{en} \cot \theta_n + \tan \theta_n}{1 + \bar{Y}_{en} \cot \theta_n \tan \theta_n - \bar{B} \tan \theta_n}$$

$$Z_e Y_1^s = j \tan \theta_n, \quad Z_e Y_1^a = (Z_e Y_1^s)^{-1}$$

$$\bar{Y}_{en} = \kappa_{en}/\kappa_n, \quad \bar{B} = B/(\kappa_n/w\mu)$$

B is given in Appendix B by equation B-2, and N_n is the slitted parallel plate array mode normalization given by

$$N_n^2 = \frac{1}{\iint_{\text{cell}} \underline{e}_n(\underline{z}) \cdot \underline{e}_n(\underline{z}) dA} \quad (\text{D-8})$$

REFERENCES

1. L.B. Felsen, "General Formulation of Diffraction Problems" - class notes, 1969.
2. L.B. Felsen and N. Marcuvitz, Radiation and Scattering of Waves, Chap 2, Prentice Hall, New Jersey, 1973.
3. M. Abramowitz and J. Stegun, Handbook of Mathematical Functions, pg. 807, Dover, 1965.
4. H.L. Bertoni and A. Hessel, "Group Velocity and Power Flow Relations for Surface Wave in Plane Stratified Anisotropic Media," IEEE Trans. Ant. and Prop., Vol. AP-14, No. 3, pp. 344-352, May, 1966.
5. Private Communication for A. Hessel.
6. H.M. Altschuler and A.A. Oliner, "Discontinuities in the Center Conductor of Symmetric Strip Transmission Line", IRE Trans of Microwave Theory and Tech., Vol. MTT-8, No. 3, May 1960, pp. 328-339.
7. Q. Balzano, L.R. Lewis, K. Siwiak, "Analysis of Dielectric Covered Arrays on Large Cylinders" AFCRL-7C-73-0587 Scientific Report, Aug. 1973.
8. P.M. Morse and H. Feshbach, Methods of Theoretical Physics, Part 1, McGraw-Hill, New York, 1953, p. 823.
9. R.F. Harrington, Time-Harmonic Electromagnetic Fields, McGraw-Hill, New York, 1961, pp. 180-184.
10. S. Edelberg and A. Oliner, "Mutual Coupling Effects in Large Antenna Arrays: Part I - Slot Arrays", IRE Trans. AP, May 1960.
11. R.E. Collin, Foundations for Microwave Engineering, McGraw-Hill, New York, 1966, p. 371.
12. L.R. Lewis and A. Hessel, "Propagation Characteristics of Periodic Arrays of Dielectric Slabs", IEEE Trans. on MTT, Mar., 1971.
13. G.V. Borgiotti, "Modal Analysis of Periodic Planar Phased Arrays of Apertures", IEEE Proc., Nov. 1968.

14. G.H. Knittel, A. Hessel and A.A. Oliner, "Element Pattern Nulls in Phased Arrays and Their Relation to Guided Wave", IEEE-Proc. Nov. 1968.
15. L.R. Lewis, A. Hessel and G.H. Knittel, "Performance of a Protruding Dielectric Waveguide Element in a Phased Array", IEEE - Trans AP Nov. 1972.
16. N.A. Begovich, "Capacity and Characteristic Impedance of Strip Transmission Lines with Rectangular Inner Conductors, IRE Trans. on MTT, MTT-3, #2, 1952, pp. 127-133.
17. N. Marcuwitz, Waveguide Handbook, Dover, 1965.
18. R.E. Collin, Field Theory of Guided Waves, McGraw-Hill, 1960.